Rheology and tribology at the nanoscale

Jean Comtet

THÈSE DE DOCTORAT

de l'Université de recherche Paris Sciences et Lettres
PSL Research University

Préparée à l'Ecole Normale Supérieure de Paris

Rhéologie et Tribologie aux Nanoéchelles

École doctorale n°564

PHYSIQUE EN ÎLE DE FRANCE

Spécialité PHYSIQUE DE LA MATIÈRE MOLLE ET NANOSCIENCES

COMPOSITION DU JURY :

M Lydéric Bocquet
ENS Paris, Directeur de thèse

M Joël Chevrier
Univ. Grenoble-Alpes, Président du Jury

Mme Annie Colin
ESPCI, Invitée

M Carlos Drummond
Univ. de Bordeaux, Examinateur

M Yoël Forterre
Univ. Aix-Marseille, Rapporteur

M Thierry Ondarçuhu
Univ. de Toulouse, Rapporteur

Mme Susan Perkin
Oxford University, Examinatrice

M Alessandro Siria
ENS Paris, Directeur de thèse

M Michael Urbakh
Tel Aviv University, Examinateur

Soutenue par **Jean Comtet**
le 3 Juillet 2018

Dirigée par **Lydéric Bocquet**
et par **Alessandro Siria**

ENS ÉCOLE NORMALE SUPÉRIEURE | PSL RESEARCH UNIVERSITY PARIS

Remerciements

Je voudrais commencer par remercier les membres du jury pour l'intérêt qu'ils ont porté à mon travail. J'ai apprécié leur lecture attentive du manuscrit, ainsi que leurs questions, commentaires et la discussion stimulante qui a suivi mon exposé. Merci à Thierry Ondarçuhu et Yoël Forterre d'avoir accepté d'être les rapporteurs de ma thèse. Je remercie Joël Chevrier de m'avoir fait l'honneur de présider le jury. Enfin, je souhaite remercier Susan Perkin, Michael Urbakh et Carlos Drummond pour leurs commentaires pertinents durant la soutenance.

Mes deux directeurs de thèse, Alessandro Siria et Lydéric Bocquet, ainsi qu'Antoine Niguès sont à la source de l'environnement exceptionnel dont j'ai bénéficié au cours de ces trois années. Alessandro, merci pour ta confiance et la liberté que tu m'as accordée. Je retiens ton inventivité et ta volonté de toujours vouloir aborder et viser des questions nouvelles et parfois difficiles. J'espère emporter un peu de ces qualités avec moi. Merci de m'avoir aidé à prendre du recul par rapport aux manips et à garder la tête froide dans les moments de doutes. Lydéric, merci pour ta générosité, ton énergie et ton optimisme à toute épreuve. Tu es une vraie source d'inspiration pour moi et j'espère pouvoir faire fructifier un peu de la vision que tu m'as transmise. Merci à tous les deux pour votre bienveillance au quotidien et pour vos conseils avisés sur la recherche et la vie après la thèse. Antoine, tu m'as formé sur le montage diapason et tu m'as appris à faire de vraies manips. Ton soutien et ton entrain ont été vraiment équilibrants au cours de ces trois années.

Je voudrais aussi remercier Annie Colin, qui a pris une part intégrante à cette thèse. Annie, merci pour la confiance que tu m'as accordée, et pour notre collaboration. J'ai vraiment apprécié travailler avec toi. Merci pour ton dynamisme et ton engagement.

Je souhaite maintenant remercier mes collaborateurs. Vojtech Kaiser et Benoit Coasne pour votre aide précieuse sur les liquides ioniques. Guillaumé Chatté pour notre travail sur le rhéoépaississement et Guillaume Ovarlez pour ton sens critique. Antoine Lainé pour ton aide sur le projet nano-jonction, puis pour ton travail durant toute cette année de passation. J'espère que cela débouchera sur de jolis travaux. Luca Canale, merci pour ta persévérance et ton endurance sur le projet ski. Merci enfin à Christophe Clanet et Caroline Cohen d'apporter un regard toujours rafraichissant sur ce projet.

Je voulais aussi remercier toute la communauté Liquides aux Interfaces et les diverses personnes avec qui j'ai eu plaisir à échanger scientifiquement aux cours de ces trois années. Merci notamment à Elisabeth Charlaix, Benjamin Cross, Benjamin Rotenberg, Thomas Salez, Cécile Cottin-Bizonne, Abdelhamid Maali et Leo Garcia.

Place maintenant aux membres de l'équipe Micromégas.

Les postdocs dont je partage maintenant la dure condition. Merci Adrien pour ton amitié, ton partage et les mails absurdes que tu continues à envoyer. Timothée pour l'exemple de sincérité et de solidité que tu renvoies. Merci Eleonora et Elisa pour votre bonne ambiance et votre implication pour le bon fonctionnement de l'équipe. Benoit pour ton flegme et ta tranquillité. Merci Hiroaki pour le prêt du mac et les gâteaux au thé.

Mes co-thésard.e.s : Laetitia pour ton énergie débordante et ton enthousiasme, Sophie pour être un exemple d'efficacité et d'engagement et pour avoir éclairci toutes les embûches administratives de la thèse avec quelques mois d'avance. Anthony pour ton honnêteté et ton humour. Antoine et Luca à nouveau, pour le temps passé ensemble sur les manips et pour votre franchise et votre équilibre. Merci aux stagiaires: Axel, Agastia et Evelyne. Et merci aux nouveaux arrivants pour les moments passés ensemble: Nikita et Alice ainsi qu'Amin et Christie.

Cette thèse a été réalisée au Laboratoire de Physique Statistique de l'ENS. Je remercie Jorge Kurchan de m'avoir accueilli au laboratoire. Merci à Nora Sadaoui, Annie Ribaudeau, Benoit Paulet et Fabienne Renia pour leur bienveillance et leur efficacité dans la gestion des commandes, missions et autres questions administratives. Un grand merci à José Palomo et Michaël Rosticher de la salle blanche. Merci à tout le personnel de l'atelier central (notamment Jean-Michel Isac, Arnaud Leclercq, Mathieu Sardin et Nabil Garroum) pour les pièces réalisées à temps. José Da Silva Quintas et à Carlos Goncalves Domingues de l'atelier du LPS. Cyrille LeGallo pour le matériel. Didier Courtiade, Catherine Gripe et Célia Ruschinzik pour leur implication dans la gestion et le bon fonctionnement des bâtiments. Zaire Dissi et Yann Colin pour l'informatique. Merci à Laura Baron-Ledez de l'Ecole Doctorale. Merci enfin à Jean-Francois Allemand et Marie-Caroline Julien pour avoir accepté de faire partie de mon comité de thèse et pour leurs conseils avisés.

Au cours de ces annés à l'ENS, j'ai eu la chance de croiser divers thésards et post-doc, avec qui j'ai pris plaisir à discuter. Merci notamment à Josh McGraw, Steve Donaldson, Eugene Choi, Nariaki Sakai, Hugo Perrin, Lauriane Contamin, Tino Cubaynes, Clémence Gruget, Jean Goder, Paul Heo et Samuel Poincloux. Merci aussi aux permanents avec qui j'ai eu la chance d'échanger : Takis Kontos, Kristina Davitt, Francois Petrelis et Eric Perez.

Merci à tous mes amis de Paris, notamment Jérome, Julien, Pauline, Addo et Agnès. Ma famille, notamment mes parents à qui je dois beaucoup sur le choix de ce chemin ainsi que mes grand-frères Manu et Fred.

Enfin, merci à Emmanuelle, l'amour de ma vie, pour son soutien constant, et sans qui rien n'aurait été pareil.

Contents

Introduction

Fundamentally new paradigms are expected to emerge for the fields of soft matter and mechanics at the nanometer scale. Those new behaviors stems principally from two distinct effects: (i) a breakdown of the continuum concepts of mechanics when reaching molecular sizes for which the granularity of matter has to be accounted for and (ii) the increasingly predominant role played by interfaces and surfaces in nanoscale systems, leading to the appearance of new force scales (Van der Waals, electrostatic forces...).

Importantly, this relation between nanosciences and traditional soft-matter and mechanics is dual. On the one side, the traditional fields of soft matter and mechanics provide well grounded concepts, approaches and questions to study, characterize and rationalize the behavior of materials at the nanoscale. On the other side, many macroscale phenomena in soft matter take their origin at the nanoscale, and can thus be illuminated by experiments at those scales. This domain at the frontier between soft matter and nano science has been allowed by the development of experimental techniques to measure and quantify interactions at the nanoscale, such as Surface Force Apparatus and Atomic Force Microscopy, as well as the development of techniques to routinely manipulate and fabricate objects at the nanoscale.

In this Manuscript, we use a tuning fork based Atomic Force Microscope to measure the properties of various soft matter systems at the nanoscale. The use of frequency-modulation Atomic Force Microscopy techniques allow us to disentangle the conservative and dissipative dynamic mechanical responses of nanoscale materials, extending traditional soft-matter rheological approaches to the nanoscale. Doing so, we evidence several dramatic transitions in the mechanical response of materials. Those transitions can be thermodynamic and driven by surface effects, as in the case of the *confinement-induced freezing of ionic liquids*, or driven by external forcings such as shear or normal pressure, as in the case of *shear-induced melting of nanometric gold junctions* and *stress-induced friction between particles in shear thickening suspensions*. Finally, we discuss some perspectives associated with this work, and show that such changes in the mechanical response of nanoscale systems can be particularly interesting in the context of reactive lubrication and friction.

Chapter 1: Mechanics at the Nanoscale with the Tuning Fork based Atomic Force Microscope.

Force measurements at the nanoscale can be challenging, and a robust instrumentation is necessary for this daunting task. We show in this Chapter that we can take advantage of quartz-tuning fork based Atomic Force Microscopy techniques to measure quantitatively the dynamic response of fluid and solid materials at the nanoscale. Traditionally used in hard condensed matter for exquisite imaging and force sensing at the atomic scale, this instrument can be extended to the study of soft condensed matter systems. We introduce in this Chapter the various framework and experimental techniques associated with the tuning fork. In particular, we show that the quartz-tuning fork based Atomic Force Microscope can be fruitfully used as a nano-rheometer, allowing quantitative measurements of conservative and dissipative mechanical impedance of nanoscale soft matter systems, and unprecedented characterization of friction and dissipation at those scales.

Chapter 2: Nanoscale Capillary Freezing in Ionic Liquids

In this second Chapter, we show how confinement drastically affects the properties and flow of certain liquids. We focus on a particular type of electrolytes, known as Ionic Liquids, which are composed purely of ions and are thus governed by strong electrostatic interactions, challenging the conception of the liquid state. We show that ionic liquids can undergo a sudden change in their mechanical response under nanoconfinement, which is interpreted as a freezing transition. This response is found to be strongly dependent on the electronic properties of the confining materials, with more conductive materials facilitating this transition. We rationalize these observations by considering the relative wetting properties of ionic liquid and solid phases at metallic interfaces.

Chapter 3: Molecular Rheology of Gold Nanojunctions

Similarly to the liquid state, the solid state can be challenged at the molecular scale. In this third Chapter, we probe plasticity at the individual atomic level by measuring the viscoelastic rheological response of gold necks of few atoms radius, submitted to picometric oscillations. Shearing the bridge with increasing amplitude, we uncover a dramatic transition from a purely elastic regime to a plastic flow regime, up to the complete shear-induced melting of the bridge. Varying the lateral junction size, we study the dependence of those distinct rheological regimes on junction geometry. In those molecular objects, plastic flow seems to be limited by the slip of atomic planes under shear, as predicted for dislocation free systems.

Chapter 4: Pairwise Frictional Profile between Particles and the Non-Newtonian Rheology of Suspensions

Suspensions are hybrid objects, composed of solid particles in a suspending fluid. They can show non-newtonian behaviors, with for example dramatic increase in their viscosity with shear rates as in the case of shear-thickening. In this fourth Chapter, we probe the local frictional profile between pairs of particles from macroscopic suspensions, and evidence a stress-induced transition between a lubricated and frictional regime between particles at the nanoscale. Tuning the physicochemical properties of the suspending fluid, we demonstrate unambiguously that the shear thickening transition at the scale of the suspension takes its origin in this nanoscale frictional profile, and corresponds to a stress-induced transition between a low viscosity and high viscosity branch. We further rationalize the

Chapter 1

Mechanics at the Nanoscale with the Tuning Fork based Atomic Force Microscope

Contents

Mechanical measurements at the nanoscale are a daunting task and require robust and sensitive tools. In this first Chapter, we introduce the principles of the quartz-tuning fork based Atomic Force Microscope, which we used throughout this thesis. We present the principles of frequency modulation techniques, the experimental set-up and introduce the basic formalism for the quantitative measurement of dissipative and conservative force response. We show that the quartz-tuning fork based Atomic Force Microscope is a valuable tool for studying the dynamic response of confined soft matter systems.

1.1 Force measurements at the nanoscale

In condensed matter, surface forces can be measured with two main classes of instruments: Atomic Force Microscopy (AFM) and Surface Force Apparatus (SFA). We present briefly here those two instruments, and their use as static and dynamic force sensors.

1.1.1 Static force measurements

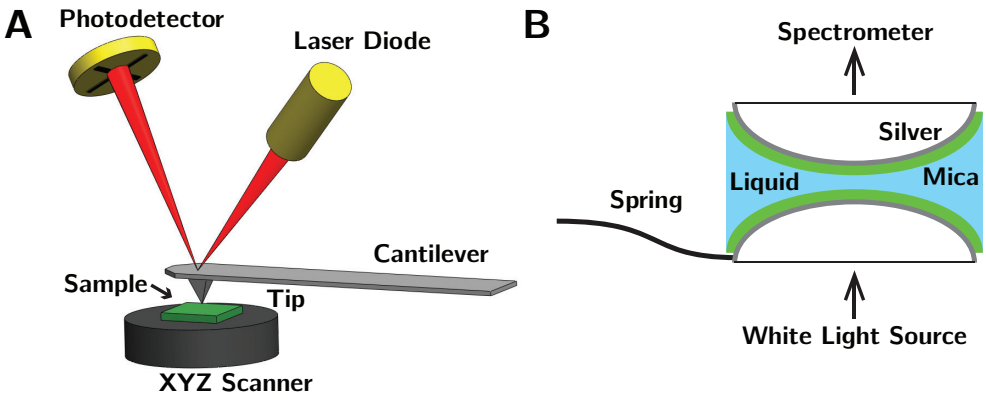

Figure 1.1: Schematic set-up for **(A)** Cantilever based Atomic Force Microscope (adapted from [20]) and **(B)** Surface Force Apparatus.

Static force measurement

In their static mode of operation, traditional AFM and SFA techniques measure the deflection δl [m] of cantilevers of known spring constant K [N.m^{-1}] to measure static forces F_s between surfaces, via:

$$F_s = K\delta l \tag{1.1}$$

In standard AFM, the cantilever deflection is measured through the reflection of a focused laser beam on a photodiode (Fig. 1.1A). AFM cantilevers have a typical size of hundreds of microns, with a sharp tip at the end ($<$ 100 nm radius of curvature). Standard spring constants range from 0.01 to 10 N.m^{-1}.

In classical SFA, the confining surfaces are typically back-silvered atomically smooth mica surfaces of centimetric radius of curvature (Fig. 1.1B). The deflection of the spring and the position between the two surfaces is obtained via white light interferometry, with angstrom resolution. Typical spring constants are of the order of 10^3 N.m^{-1} [8, 12, 13, 26].

Limitation

For a given displacement sensitivity δl, the force sensitivity of the instrument in static mode is inversely proportional to the spring constant K. High force sensitivity thus requires the use of small spring constant K.

However, small value of the spring constant K are also detrimental as they lead to instabilities when measuring strong attractive forces. If the attractive force gradient $|\partial F/\partial x|$ of the measured force field becomes larger than the stiffness K of the cantilever (e.g. due to capillary forces or electrostatic forces...), mechanical instabilities can occur, leading to "jump to contact" or "snap to contact" of the cantilever. Those instabilities preclude the use of cantilevers with small spring constants in presence of strong attractive force gradients.

Another intrinsic limitation associated with static force measurements relates to the $1/f$ noise in cantilever fluctuations. This flicker noise can be also a strong limiting factor for static force resolution [5].

1.1.2 Dynamic force measurements

One way to overcome those limitations is to operate the cantilever or spring in dynamic mode. In dynamic mode, the cantilever or spring is deliberately vibrated by an external force. When the vibrating probe interacts with the external force field, the oscillation amplitude and phase shift between the forcing and the cantilever oscillation is modified, allowing the detection of the interaction.

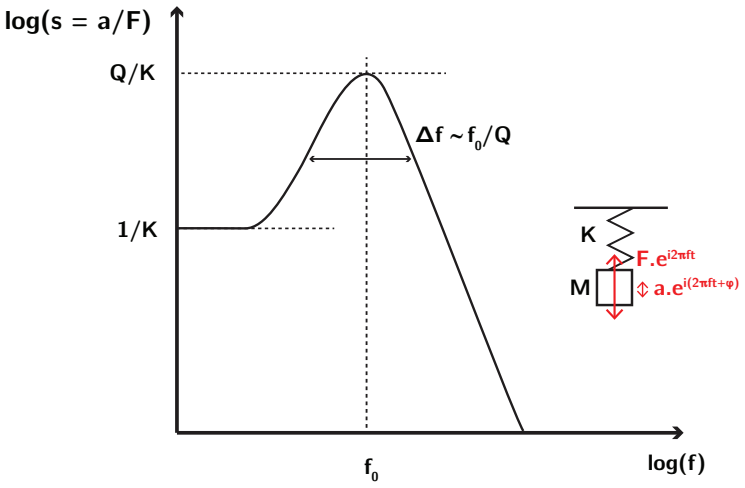

Figure 1.2: Log-log plot for the sensitivity or transfer function $s = a/F$ for a mass-spring resonator (inset) as a function of excitation frequency f. F is the driving force, a the oscillation amplitude, K [N.m^{-1}] the spring constant, M the equivalent mass, f_0 [Hz] the resonance frequency, Δf [Hz] the half width of the resonance, and $Q = f_0/\Delta f$ [-] the quality factor at resonance.

Dynamic sensitivity

A crucial parameter in dynamic mode is the sensitivity s, which quantifies the effect of an additional force δF on the amplitude change δa or phase change of the oscillator, via $\delta a = s \cdot \delta F$. The sensitivity can be simply taken as the transfer function of the resonator $s = a/F$. For a simple 2nd order mass spring resonator, the sensitivity has the typical shape shown in Fig. 1.2, with a resonance at a frequency $f_0 \sim \sqrt{K/M}$. The resonance is characterized by the quality factor Q, which can be estimated from the resonance half-width as $Q = f_0/\Delta f$.

Far before the resonance, for small oscillation frequencies, we have $s = 1/K$, as in the static case. Interestingly, at resonance, the sensibility is given by $s = Q/K$, and can thus increase by orders of magnitudes compared to the low frequency or static case, depending on the value of Q. The quality factor Q is thus a crucial parameter, as it sets the maximal sensitivity in the dynamic case. The quantity $1/s = K/Q$ is referred to as the dynamic stiffness, characterizing force sensitivity at the resonance in dynamic mode.

Amplitude and frequency modulation

Dynamic force measurements are obtained via two basic operation modes, known as amplitude modulation and frequency modulation.

Amplitude modulation

In amplitude modulation techniques, the cantilever is driven at a fixed frequency f. Elastic and dissipative interactions will cause a change in both the amplitude and the phase shift (relative to the driving signal) of the cantilever. Such amplitude modulation techniques are for example used in dynamic SFA [2, 22].

In dynamic AFM, the driving frequency is generally chosen close to the resonance frequency f_0, in order to maximize the response of the oscillator for high quality factor. However, changes in amplitude or phase due to variation of the force field will not occur instantaneously, but on a timescale $\tau \sim Q/f_0$. A high Q maximizes the sensitivity but is detrimental in term of response time.

Frequency modulation

Frequency modulation techniques were introduced to combine the benefit of high dynamic sensitivity through high quality factor Q with low response time. With frequency modulation techniques, the oscillator is systematically excited at its resonant frequency, and interactions are measured via measurement of the changes of the resonant frequency and amplitude at resonance. The response time is then given by the time to measure the change in resonant frequency, which scales as the inverse of the oscillator resonant frequency $\tau \sim 1/f_0$ (set by the phase detection bandwidth) [18], and is not related to the intrinsic quality factor Q.

1.1.3 The quartz tuning fork based AFM

The main characteristic of quartz tuning forks is precisely their high quality factor Q, which make them ideal candidates for their use in frequency modulation modes. Their excellent behavior as mechanical resonators has lead to their commercial production and use as oscillators in wristwatch (Fig. 1.3).

Tuning forks were first introduced in the context of scanning probe microscopy by Karrai in 1995 [9]. In particular they were intensively used for Scanning Near Field Optical

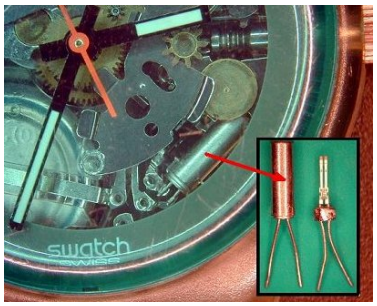

Figure 1.3: Quartz tuning forks are commercially produced for their use as excellent mechanical resonators in wristwatch.

Microscopy [6]. Since then, they have been successfully used in a variety of home-made Atomic Force Microscope set-up for hard condensed matter or surface science measurements [7, 15, 25], for example in the groups of F. Giessibl [3, 4] and E. Meyer [10, 11].

They were introduced in the group by A. Nigues in 2014 in the context of dissipation measurement during interlayer sliding of nanotubes [19].

Interestingly, they were only scarcely used in the context of soft matter [21].

Characteristics of the quartz-tuning fork

When used with frequency modulation techniques in dynamic mode, quartz-tuning forks combine several advantages.

(i) Large static stiffness

In comparison to other force measuring techniques, the main characteristic of the quartz-tuning forks are there extremely large static stiffness, of the order of tens of kN/m. This large stiffness gives the tuning fork a high mechanical stability, allowing perfect control of the tip position even under strong attractive forces (e.g. with the tip immersed in liquids) or strong repulsive forces (e.g. during indentation experiments).

However, this large static stiffness precludes the measurement of static forces with the tuning fork.

(ii) Large quality factor and low dynamic stiffness

The second characteristic of tuning forks is their excellent resonator characteristics, characterized by large quality factors Q of up to 10,000 in air, 50,000 in vacuum and 2,000-5,000 in liquids. These large quality factors confer the tuning fork a low effective dynamic stiffness K/Q, corresponding to an increased dynamic force sensitivity. For a quality factor of 10,000, the effective dynamic stiffness is thus of the order of a few $\mathrm{N.m^{-1}}$, equivalent to standard AFM cantilevers.

(iii) Quantitative impedance measurements

As we will show in the following, working in frequency-modulation AFM mode allows direct quantitative measurements of the conservative and dissipative mechanical impedance of the force field with the tuning fork.

One disadvantage of frequency modulation techniques is that the excitation frequency for the dynamic impedance measurement is fixed by the resonant frequency of the system (of the order of tens of kHz) and cannot be tuned.

1.2 The tuning fork as a mechanical resonator

1.2.1 The tuning fork and its resonant frequencies

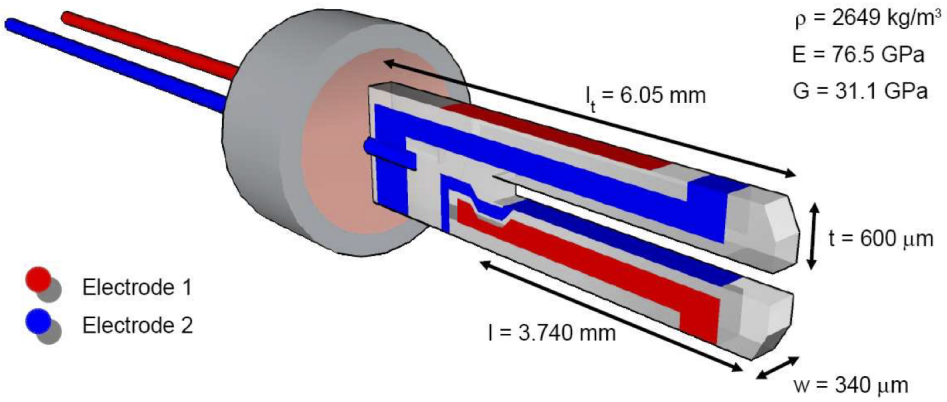

Figure 1.4: Schematic of the quartz-tuning fork used throughout this study, with the principal geometrical and physical parameters [24].

Tuning forks have several resonance frequencies, corresponding to symmetric and antisymmetric motion of there prongs. In this thesis, we used the two fundamental resonances corresponding to *antisymmetric* motion of the prongs (see Fig. 1.5). Because those antisymmetric resonance lead to negligible displacements of the center of mass, the corresponding quality factors are very large, providing an excellent dynamic force sensitivity. When a tip is attached to one prong of the tuning fork, those resonances lead respectively to normal (N) and tangential (T) motion of the attached tip with respect to the substrate, and are thus important in the context of friction studies (see Chapter 4).

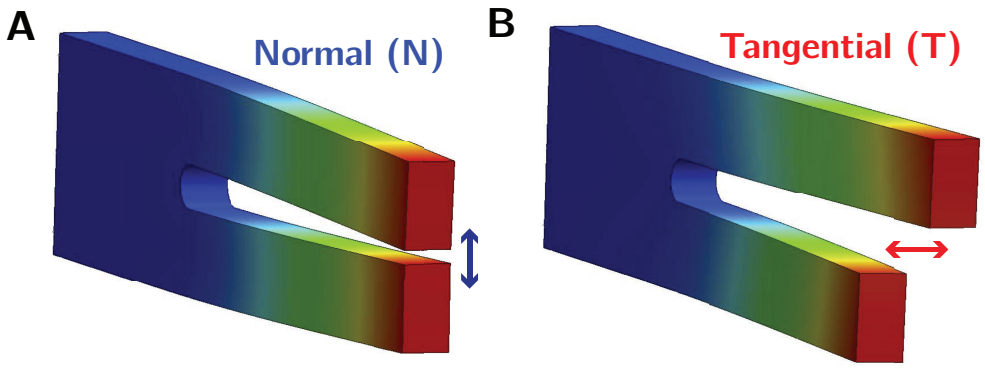

Figure 1.5: Schematic of the two principal antisymmetric oscillation modes for the tuning fork, corresponding to the excitation of **(A)** normal (N) and **(B)** tangential (T) oscillation of the tuning fork with respect to the substrate.

1.2.2 Quartz-based sensing

The prong and body of the tuning fork are made of a single quartz crystal, which has piezoelectric properties. When the tuning fork vibrates, stresses lead to polarization and

charge dissociation inside the quartz material. An alternating stress field, caused by an oscillatory motion, will thus lead to an alternating current. This current is read out using the electrodes deposited on the quartz-tuning fork, making the tuning fork a self-sensing device. In industrially made quartz-tuning forks, as the ones we used, those contacts are positioned at strategic places so as to cancel out any electrical signal stemming from non-antisymmetric deformation of the tuning fork, maximizing the signal to noise ratio for antisymmetric deformations.

One thus has a simple relation between the alternating current $i(t) = i_0 \cdot \exp(i\omega t)$ and the amplitude of oscillation $a(t) = a_0 \cdot \exp(i\omega t)$ of the tuning fork, as:

$$i(t) = \alpha \cdot a(t) \tag{1.2}$$

The factor α has been calibrated using interferometry [24] and its calibration confirmed over the course of this PhD (see Table 1.1).

1.2.3 Mechanical excitation

We excite the tuning fork mechanically, using a piezo-dither glued close to the tuning fork. The piezo-dither induces mechanical vibration of the tuning fork through its holding support. Mechanical excitation allows for a perfect decoupling between the excitation signal sent to the piezo-dither and the electric signal generated by the oscillation of the quartz prongs of the tuning fork. This decoupling contrasts with the standard electrical excitation method, which uses the electrodes and the piezoelectric properties of the quartz to simultaneously excite and detect the oscillation of the tuning fork.

One can model the effect of the piezo-dither as that of an oscillatory force $F = F_0 \exp(i\omega t)$ acting on the tuning fork. We have a perfectly linear relation between this excitation force and the oscillatory voltage $E(t) = E_0 \exp(i\omega t)$ exciting the piezo-dither, with:

$$F_0 \exp(i\omega t) = C \cdot E_0 \exp(i\omega t) \tag{1.3}$$

The transduction factor C depends on the clamping and on the added mass on the tuning fork's prong, and has to be calibrated at the beginning of each experiment (see following section).

1.2.4 Resonance

Close to the resonance, one can in a very good approximation model the tuning fork as an effective one-dimensional mechanical oscillator [1, 24]. The validity of this assumption can be verified by probing the Lorentzian-like shape of the resonance.

Equation of motion

In the absence of interactions, the dynamics of the tuning fork close to its resonant frequency can be simply modeled as a second order mass-spring resonator, with the tuning fork oscillation amplitude $a(t)$ solution of:

$$M_{\text{eff}} \cdot \frac{d^2a}{dt^2}(t) + \gamma_{\text{eff}} \cdot \frac{da}{dt}(t) + K_{\text{eff}} \cdot a(t) = F_{\text{ext}}(t) \tag{1.4}$$

with M_{eff} [kg] the equivalent mass, γ_{eff} [N.s.m^{-1}] a viscous damping coefficient, K_{eff} [N.m^{-1}] the equivalent dynamic spring constant of the tuning fork and F_{ext} [N] the external excitation forcing due to the piezo dither.

Non-dimensionalization

Non-dimensionalizing this equation leads to:

$$\ddot{a} + \frac{\omega_0}{Q} \cdot \dot{a} + \omega_0^2 \cdot a = \frac{F_{\text{ext}}}{M_{\text{eff}}} \tag{1.5}$$

with the natural resonant frequency:

$$\omega_0 = \sqrt{\frac{K_{\text{eff}}}{M_{\text{eff}}}} \tag{1.6}$$

and the quality factor at resonance:

$$Q = \frac{M_{\text{eff}} \cdot \omega_0}{\gamma_{\text{eff}}} \tag{1.7}$$

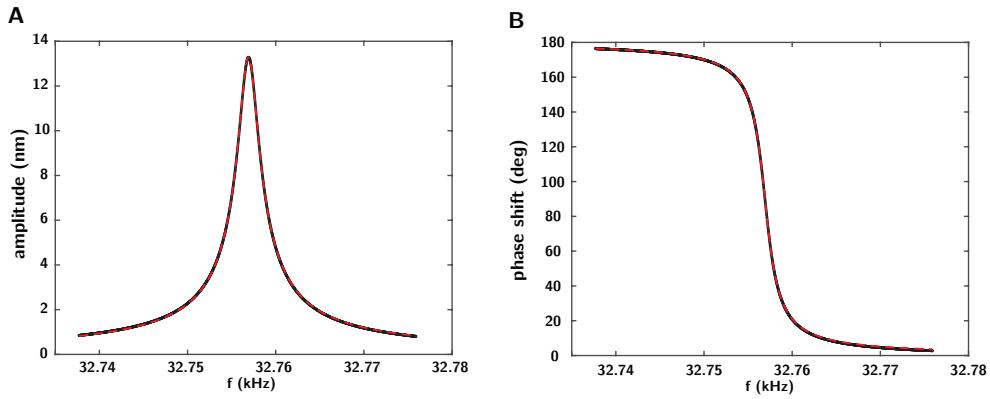

Figure 1.6: Measured amplitude **(A)** and phase shift **(B)** of the tuning fork as a function of excitation frequency f, along with theoretical fits (Eqs. 1.8 and 1.9), for a center frequency $f_0 = 32{,}756$ Hz and quality factor $Q = 13{,}725$.

Resonance

We can solve Eq. 1.5 under the oscillatory forcing $\underline{F}_{\text{ext}}(t) = F_{\text{ext}} \cdot \exp(i\omega t)$, leading to the oscillation $\underline{a}(t) = a \cdot \exp(i\omega t + \phi)$ of the prongs of the tuning fork. The amplitude a around the resonance as a function of the excitation frequency ω is given by:

$$a(\omega) = \frac{F_{\text{ext}}}{M_{\text{eff}}} \cdot \frac{1}{\sqrt{(\omega_0^2 - \omega^2)^2 + \omega^2 \omega_0^2 / Q^2}} \tag{1.8}$$

with the phase shift ϕ between the excitation force $F(t)$ and the tuning fork oscillatory motion $a(t)$ given by:

$$\tan(\phi(\omega)) = \frac{\omega \omega_0}{Q(\omega_0^2 - \omega^2)} \tag{1.9}$$

Finally, the amplitude a_0 at resonance is given by:

$$a_0 = \frac{F_{\text{ext}} Q}{K_{\text{eff}}} \tag{1.10}$$

We show in Fig. 1.6 the measured amplitude and phase shift for the resonance of a free tuning fork, along with fits of the corresponding Eqs. 1.8 and 1.9.

Additionally, we show in Fig. 1.7 the resonance for the normal and tangential oscillation modes of the tuning fork.

Lorentzian approximation

For large quality factor, the resonance (Eq. 1.8) has to a very good approximation a symmetric Lorentzian shape, with oscillation amplitude given by:

$$a = \left(\frac{F}{K_{\text{eff}}}\right) \frac{\omega_0}{\sqrt{4(\omega - \omega_0)^2 + \omega_0^2/Q^2}} \tag{1.11}$$

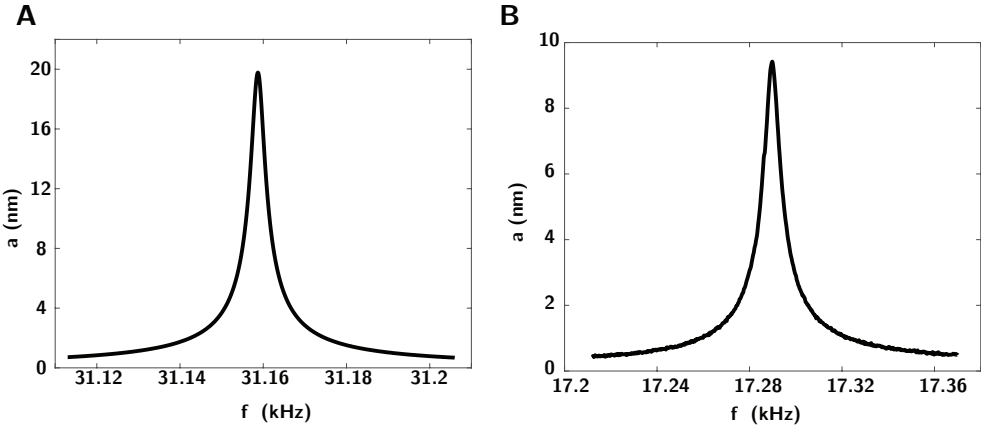

Figure 1.7: Resonance corresponding to normal **(A)** and tangential **(B)** oscillations of the tuning fork

We have $\arctan(x) \sim 1/x$ for $x \gg 1$, and we can express the variation of the phase around the resonance as:

$$\phi \sim -\frac{2(\omega - \omega_0)Q}{\omega_0} \tag{1.12}$$

1.2.5 Quality factor and force sensitivity

Quality factor

The quality factor Q quantitatively determines the sharpness of the resonance and can be related to the resonance half-width $\Delta\omega$ by $Q = \omega_0/\Delta\omega$. It is also related to the sharpness of the phase change around the resonance, with $d\phi/d\omega \sim Q/\omega_0$ (Eq. 1.12).

Additionally, the quality factor characterizes the equilibration time τ of the oscillator, via $\tau \sim Q/\omega_0$.

Force sensitivity

As we saw earlier, the force sensitivity in dynamic mode is given by $s = Q/K$. The quality factor of the resonance is thus a crucial parameter, as it sets the sensitivity of the tuning fork at the resonance.

The sensitivity at the resonance is directly proportional to the quality factor Q.

The limiting parameters for Q are internal damping loss of the quartz-crystal, clamping loss, air damping and added mass the prongs. In vacuum, the quality factor for the normal oscillatory motion can increase from 10,000 up to 50,000.

1.2.6 Parameters calibration

To obtain quantitative information on the force field, we need to calibrate the equivalent parameters describing the tuning fork's motion.

Equivalent stiffness K_{eff}

Among the equivalent parameters characterizing the tuning fork, the equivalent stiffness K_{eff} is calibrated once and for all by pressing on cantilevers of known spring constant, and measuring the resulting frequency shift for the resonance [16, 20, 24] (see following Section). The equivalent stiffness for normal and tangential oscillatory modes are given in Table 1.1.

Quality factor and resonant frequency

The quality factor Q_0 in the absence of interactions and resonant frequency f_0 (Eq. 1.3) are measured for each tuning forks at the beginning of the experiments, by fitting the resonance (Fig. 1.6).

Force transduction

The transduction factor C between the excitation voltage and the force F is also obtained from the quality factor and the amplitude at resonance (Eq. 1.10) for a given excitation voltage E_0, with:

$$C = \frac{F_{\text{ext}}}{E_0} = \frac{K_{\text{eff}} a_0}{Q_0 E_0} \tag{1.13}$$

We summarize in the following table the main parameters for the two oscillatory modes of the tuning fork.

Parameter	Normal Mode	Tangential Mode
Resonant Frequency f_0	≈ 32 kHz	≈ 18 kHz
Equivalent Stiffness K	40 kN.m^{-1}	12 kN.m^{-1}
Piezoelectric Current α	2 nA.nm^{-1}	0.034 nA.nm^{-1}
Typical Quality Factor in air	10,000 – 12,000	8,000

Table 1.1: Parameters for the two oscillatory modes of the tuning fork

1.3 Quantitative measurements of dissipative and conservative response

1.3.1 Conservative and dissipative force field

When submitted to an external force field, the shape of the resonance of the tuning fork is modified. We show in this section that quantitative informations about the conservative and dissipative part of the interacting force field can be obtained, via measurements of the shift of the resonance frequency, amplitude at resonance and external excitation force due to the piezo-dither.

In particular, we show that non-linear dissipative forces such as solid friction forces can also be extracted from such measurements.

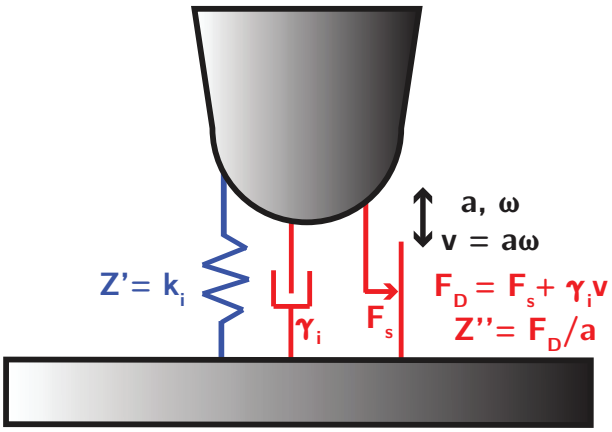

Figure 1.8: Tuning fork's tip oscillating at frequency ω and amplitude a. The tip is interacting with a force field, modeled by a conservative part corresponding to a stiffness k_i or real mechanical impedance Z', and dissipative part F_D, modeled by the sum of viscous like damping force $\gamma_\mathrm{i}\dot{x}$ and solid-like friction force $F_\mathrm{S}\dot{x}/|\dot{x}|$, and characterized by the dissipative mechanical impedance $Z'' = F_\mathrm{D}/a$.

We model the external force field by the sum of conservative and dissipative contributions (Fig. 1.8).

We can also characterize the external force field by its mechanical impedance $Z^* = F^*/a$ [N/m], with F^* the complex force felt by the tuning fork. This notation is especially convenient when measuring materials' properties, for which one need to compare both the elastic and the dissipative mechanical impedance.

Conservative force field

We can describe the conservative component of the force field by the stiffness k_i [N/m], or equivalently the real part Z' [N/m] of the mechanical impedance:

$$Z' = k_\mathrm{i} = -\frac{\partial F}{\partial x} \tag{1.14}$$

Z' or k_i characterizes *elastic forces* which are *in phase with the displacement.*

Dissipative force field

The dissipative inelastic part of the force field is characterized by the dissipative forces F_D. *Dissipative forces are in opposition of phase with the displacement.*

The dissipative part of the force field can also be characterized by the imaginary part Z'' [N/m] of the mechanical impedance, which is the ratio of dissipative forces F_D [N] by the oscillation amplitude a [m]:

$$Z'' = \frac{F_\mathrm{D}}{a} \tag{1.15}$$

To fix the ideas, we can consider the dissipative frictional forces F_D to be expressed as the sum of a viscous and static (constant) friction force:

$$F_\mathrm{D} = \gamma_\mathrm{i}\dot{x} + F_\mathrm{S}\frac{\dot{x}}{|\dot{x}|} \tag{1.16}$$

1.3.2 Tuning fork in interaction

Interacting tuning fork

The non-linear friction force $F_S \dot{x}/|\dot{x}|$ can be express under a periodic forcing as a Fourier series:

$$F_S \frac{\dot{x}}{|\dot{x}|} = \frac{4F_S}{\pi} \sum_{k=0}^{\infty} \frac{\sin((2k+1)2\pi f t)}{2k+1} \tag{1.17}$$

The equation of motion for the interacting tuning fork under an external forcing $\underline{F}_{ext} = F_{ext} \exp(i\omega t)$ becomes, considering only the response at the harmonic forcing frequency:

$$-\omega^2 \underline{X} + i\omega \frac{\gamma_{eff} + \gamma_i}{M_{eff}} \underline{X} + \omega_0^2 \left(1 - \frac{k_i}{K_{eff}}\right)^2 \underline{X} = \frac{1}{M_{eff}} \left(F_{ext} - \frac{4F_S}{\pi}\right) \tag{1.18}$$

with factor $4/\pi$ stemming from the first Fourier coefficient of the square-like shape of the solid friction force (Eq. 1.17).

The restriction to the response at the harmonic frequency is justified by the lock-in detection scheme for the signal, which filters out higher harmonics in the oscillation signal.

Conservative response

Equation 1.18 corresponds to a new resonance, with shifted resonance frequency ω_i such that

$$\omega_i = \omega_0 \sqrt{1 - \frac{k_i}{K_{eff}}} \approx \omega_0 \left(1 - \frac{k_i}{2K_{eff}}\right) \tag{1.19}$$

One obtain thus a fundamental relation between the frequency shift $\delta f = (\omega_i - \omega_0)/2\pi$ of the resonance, and the conservative interaction stiffness k_i or conservative impedance Z', with:

$$Z' = k_i = 2K_{eff} \frac{\delta f}{f_0} \tag{1.20}$$

Dissipative response

Considering Eq. 1.18, the purely viscous-like damping leads to a decrease of the quality factor at resonance $Q_i = \omega_i M_{eff}/(\gamma_{eff} + \gamma_i)$, whereas the solid-like friction force acts as an effective decrease of the external excitation force F_{ext}.

The shift in resonance frequency is typically orders of magnitude smaller than the resonance frequency, with $\delta f/f_0 \approx 10^{-4}$, leading to a change in the effective damping $\delta Q/Q \approx 10^{-4}$, which can be safely neglected. We thus have in an excellent approximation $Q_i = \omega_0 M_{eff}/(\gamma_{eff} + \gamma_i)$.

We thus obtain the following relation between the amplitude a at resonance, the quality factor Q at resonance, the external excitation force F_{ext}, the solid-like dissipative force F_S and the stiffness K_{eff} with:

$$\frac{a_0}{Q} = \frac{(F_{ext} - 4F_S/\pi)}{K_{eff}} \tag{1.21}$$

We first consider the limit where $F_S = 0$.

When all dissipative forces are of purely viscous type, the dissipative forces $F_{\mathbf{D}}$ and dissipative impedance Z'' are directly related to the change in the quality factor from Q_0 to Q, via

$$Z'' = \frac{F_{\mathbf{D}}}{a} = K_{\mathbf{eff}} \left(\frac{1}{Q} - \frac{1}{Q_0} \right) \tag{1.22}$$

In the presence of non-linear solid friction force, one can still measure the dissipative forces F_{D} by measuring the additional force $F_{\mathrm{ext}} - F^0_{\mathrm{ext}}$ necessary to provide to the tuning fork to maintain a constant oscillation amplitude a_0 and compensate for additional dissipation, with

$$F_{\mathrm{ext}} - F^0_{\mathrm{ext}} = \gamma_{\mathrm{i}} \cdot v + \frac{4F_{\mathrm{S}}}{\pi} \approx F_{\mathrm{D}} \tag{1.23}$$

with $F^0_{\mathrm{ext}} = K_{\mathrm{eff}} a_0 / Q_0$ the external excitation force in the absence of interactions (characterizing internal damping of the tuning fork).

The factor $4/\pi \approx 1.27$, corresponds to an error of 27 % and characterizes the largest error on the measurement of non-linear dissipative forces due to the loss of informations in the harmonics.

One can thus directly measure the sum of all dissipative forces (viscous or not) via the measurement of the external excitation force necessary to apply on the tuning fork to keep a constant oscillation amplitude a_0. This excitation force $F_{\mathbf{ext}}$ is directly proportional to the excitation voltage E of the piezo-dither, via:

$$Z'' = \frac{F_{\mathbf{D}}}{a_0} = \frac{K_{\mathbf{eff}}}{Q_0} \left(\frac{E}{E_0} - 1 \right) \tag{1.24}$$

The factor $C = K_{\mathrm{eff}} a_0 / Q_0 E_0$ characterizes the transduction of the piezo-dither, and one can equivalently express the dissipative forces as :

$$F_{\mathrm{D}} = C(E - E_0) \tag{1.25}$$

1.3.3 Ring-down experiments

The nature and amplitude of the dissipative forces can be obtained alternatively from "ring-down" experiments, where we monitor the relaxation of the oscillator after the interruption of the excitation. This is a classical way to measure damping of oscillators, and has been recently applied in the context of tuning forks [27].

The dynamics of the oscillator under both sliding friction and viscous-like damping is not trivial. We follow here Ricchiuto [23], and compute the amplitude at the resonance

frequency, given by:

$$x(t)/a_0 \approx \exp(-\omega_0 t/2Q)\left[1+\alpha+\frac{2\alpha}{1-\exp(-\pi/2Q)}\right] + \left[\alpha-\frac{2\alpha}{1-\exp(-\pi/2Q)}\right] \quad (1.26)$$

with $\alpha = F_S/(ka_0)$. In the limit of a large quality factor $Q \gg 1$, we obtain:

$$x(t)/a_0 \approx \exp(-\omega_0 t/2Q)\left[1+\frac{4\alpha Q}{\pi}\right]-\frac{4\alpha Q}{\pi} \quad (1.27)$$

and the initial velocity is expressed as:

$$\dot{x}(t)/a_0\omega_0 \approx -\left[\frac{1}{2Q}+\frac{2\alpha}{\pi}\right] \quad (1.28)$$

One can thus disentangle the effect of viscous and solid-like friction forces using ring-down experiments (see Chapter 4).

Viscous friction limit

For a purely viscous damping, $\alpha = 0$ and the oscillator relaxes purely exponentially, with a characteristic time $\tau = 2Q/\omega_0$.

Sliding friction limit

For an oscillator damped only by sliding friction, $Q = \infty$ and we recover a linear decay of the motion, with $x(t) \approx a_0(1-\mu\omega_0 t)$ and $\dot{x}(t) = a_0\omega_0\mu$.

1.4 Tuning-Fork based AFM set-up

Commercially available tuning forks have to be prepared before each experiment, to become usable AFM probes. In this Section, we present briefly the workflow necessary to prepare the tuning forks.

1.4.1 Tuning Fork preparation

Getting to the quartz-crystal

The tuning forks are commercially available (*Radiospare*). They are stored under controlled atmosphere in a shell. The first step is to get the tuning fork out of its shell.

Wire Gluing

The second step is the gluing of the tip to one of the prong of the tuning fork (typically tungsten or gold). The wire of 200 µm diameter is cut to a few centimeters and cleaned with ethanol. A dot of conductive epoxy glue is deposited on one prong of the tuning fork (preferentially touching one of the tuning fork's electrodes in order to ground the tip). The wire is put in contact to the glue, which can be cured using a hair-dryer.

Tip Etching

To get reliable data, an important step relies in obtaining clean and controlled etched tips [17]. We used the so-called double lamellae drop-off etching, which takes advantage of small ring electrodes [14].

To etch the tungsten tips, a drop of 1 M NaOH in each ring creates an electrolytic cell in which the tungsten wire is etched. After an etching time of less than 5 minutes, the wire becomes so thin that the lower portion of the tungsten wire falls down under its weight, opening the circuit and thus stopping the etching process automatically. The upper part of the tip has a radius typically smaller than 100 nm.

In some applications, it may be necessary to increase the tip radius to larger values. To do so, we connect the cathode to one electrode of the tuning fork, which is contacting the tungsten wire via conductive glue. Tip end radii up to 10 µm can be obtained with this technique.

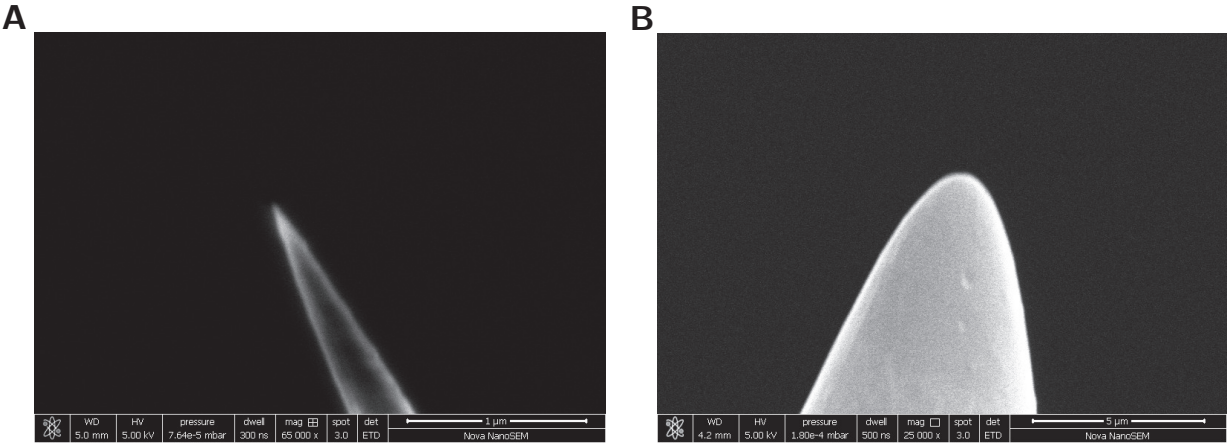

Figure 1.9: Typical AFM tip obtained after the etching process. **(A)** thin tip of ≈ 50 nm radius **(B)** Large tip of 2 µm radius, for rheological measurements.

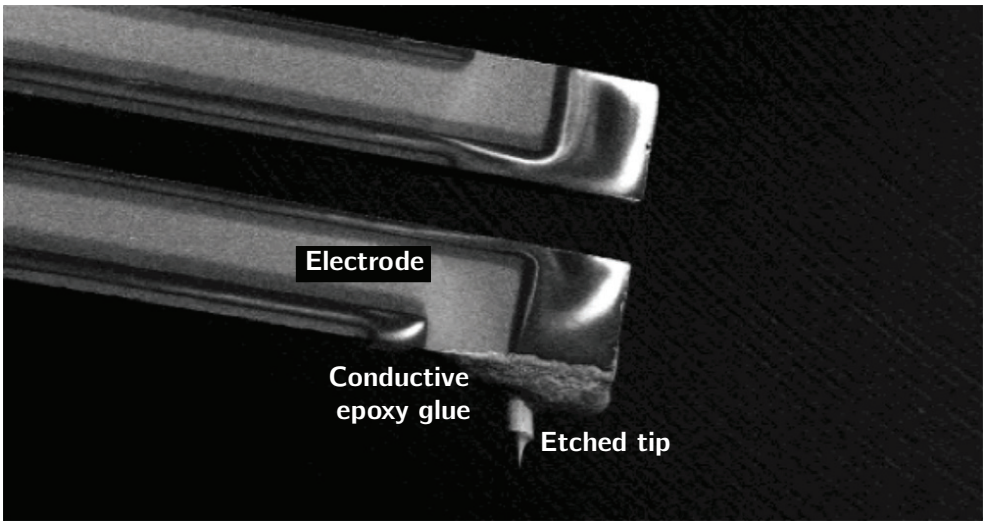

Figure 1.10: SEM image of a prepared tuning fork with etched tip glued on one prong.

1.4.2 Integrated AFM Set-up

We present in this section the integration of the tuning fork in the global AFM set-up.

AFM Set-up

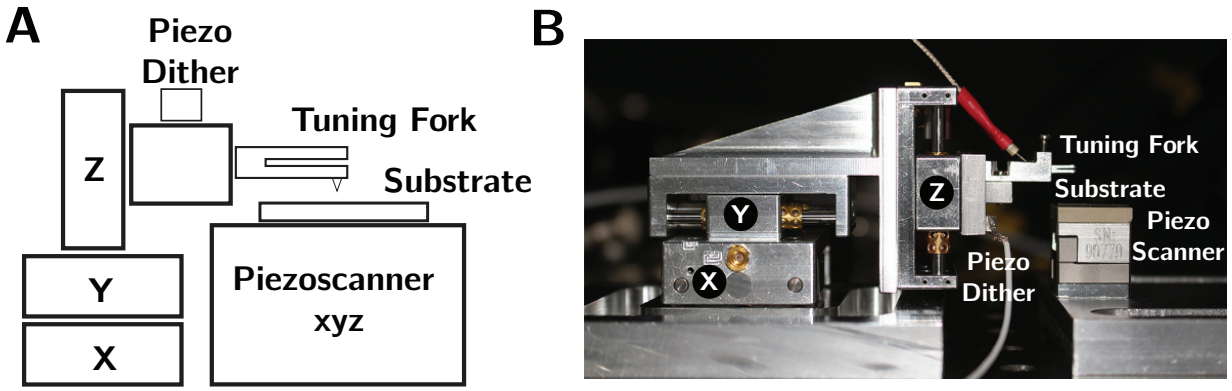

Figure 1.11: Schematic of the AFM set-up, with coarse positioning motors (X, Y, Z), a 3-axis piezoelectric scanner (xyz), the tuning fork, substrate and piezo dither.

The AFM set-up is composed of two kinds of actuators/positioners.

Coarse positioning motors allow the approach of the tip from the substrate. They are inertial MechOnics motors. They can move with a step size of 30 nm over a total course of 1 cm.

For AFM imaging or force spectroscopy, we use a piezoelectric scanner from Piezosystem Jena. The scanner allows smooth displacements of up to 8 µm in the 3 spatial directions, with a precision below 100 pm.

The coarse approach motors are first used to approach the tip of the tuning fork at several micrometers above the substrate (see Fig. 1.12). Smooth displacements of the piezo scanner are then used to measure interactions of the tip with the substrate.

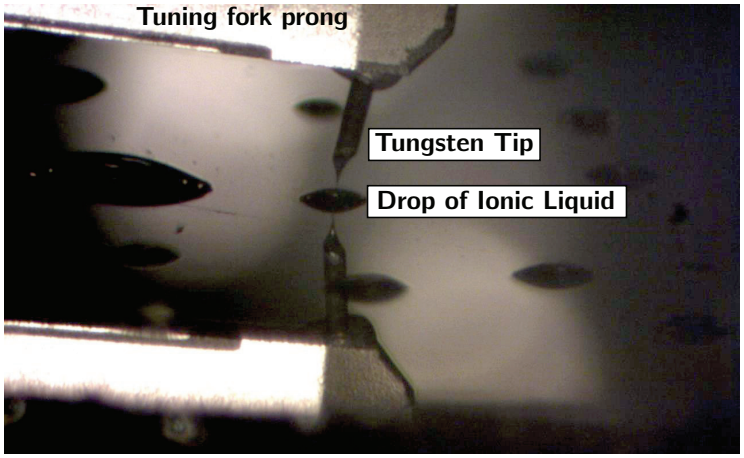

Figure 1.12: Photograph of the tuning fork tip standing close to the substrate, along with its reflection.

Isolation and stability

The environment and isolation of the AFM is critical for some measurements. The AFM stands on a passively damped breadboard table, which is enclosed in an acoustic box. The acoustic box sits on a 1 tonne marble table, coupled to the floor with rubber pads. All passive damping elements act as low pass filters for acoustic or mechanical vibrations. The acoustic box is also critical to reduce thermal drift in the set-up.

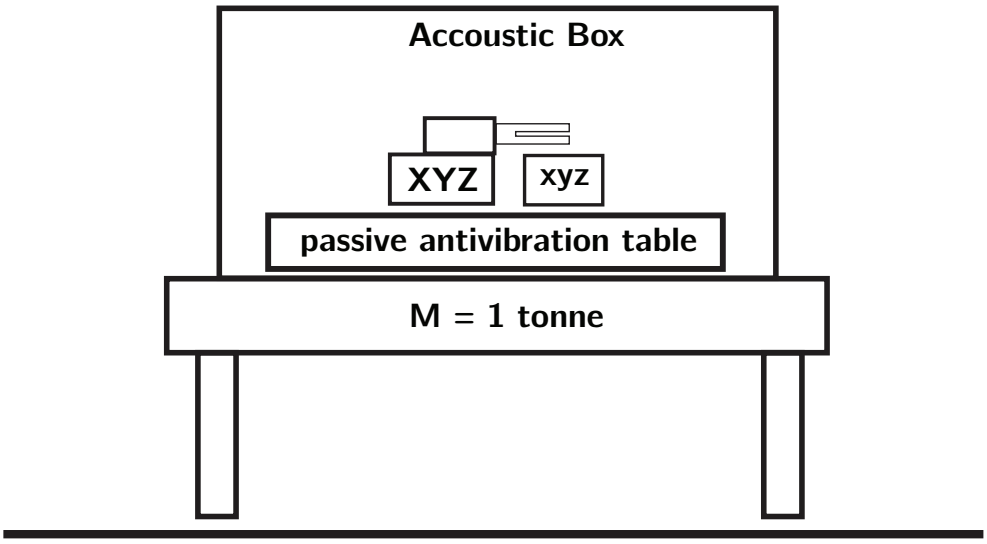

Figure 1.13: Schematic of the environment isolation for the quartz-tuning fork AFM set-up.

External environment

In several cases, it can be important to control the external environment of the set-up in term of vapor pressure. To control humidity, we place around the set-up a plexiglass box, initially filled with nitrogen and containing desiccants. The AFM can also be adapted to work in a vacuum chamber.

1.4.3 Signal acquisition

Detection of the oscillation amplitude

The piezoelectric current generated by the oscillation of the tuning fork is amplified using a commercial femto preamplifier (DLPCA-200), typically with a gain of 10^7 V/A, corresponding to a 50 kHz bandwidth.

Tip sample bias and current monitoring

In addition, we can apply a bias between the metallic tip and the sample as shown in Fig. 1.14. The current is measured via another femto preamplifier (DLPCA-200).

1.4.4 Signal processing and control

To measure the mechanical impedance of the force field applied on the tuning fork, we have to measure the shift of resonance frequency δf [Hz], the amplitude at resonance a [m], and the excitation voltage E [V] of the piezo-dither. We thus use systematically frequency-modulation AFM techniques, which allow to measure those parameters in real time, without having to perform a resonance at each time step.

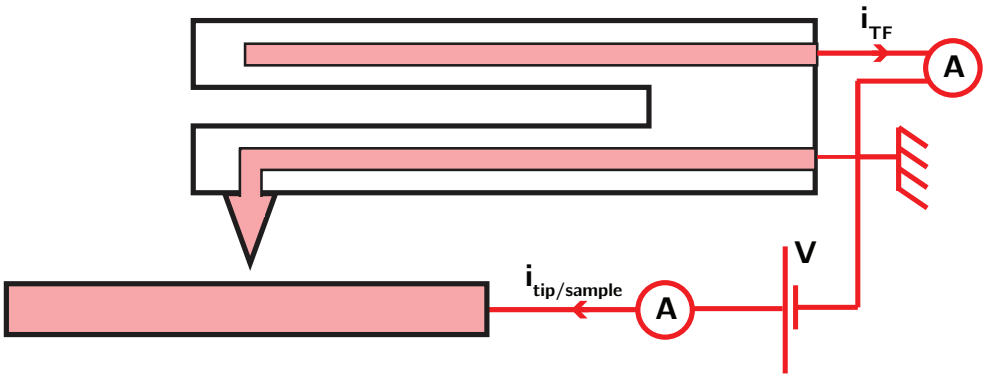

Figure 1.14: Configuration used to apply a tip/sample bias V, and measuring tip/sample current $i_{\text{tip/sample}}$.

The detection and processing of the tuning fork signals is done via a Specs-Nanonis package, designed for local probe control. It consists of a real time module RT4, one or two Oscillation Controller OC4 for detection and servo control of the tuning fork signal, a high voltage amplifier for piezoelectric scanner control and a module SC4 for data acquisition.

Lock-in

The motion of the tuning fork at the excitation frequency and the phase shift between the excitation signal and the tuning fork oscillation is detected via a lock-in amplifier. The lock-in amplifier can be thought of as a band-pass filter amplifier, with an extremely small bandwidth and extremely high Q factor, that cannot be achieved by conventional RLC circuits. It can thus extract a signal with a known frequency from a very noisy environment. In essence, a lock-in amplifier takes the input signal, multiplies it with the reference signal (Fig. 1.15, mixer) and integrates it over a specified time to obtain the DC component (Fig. 1.15, low pass filter).

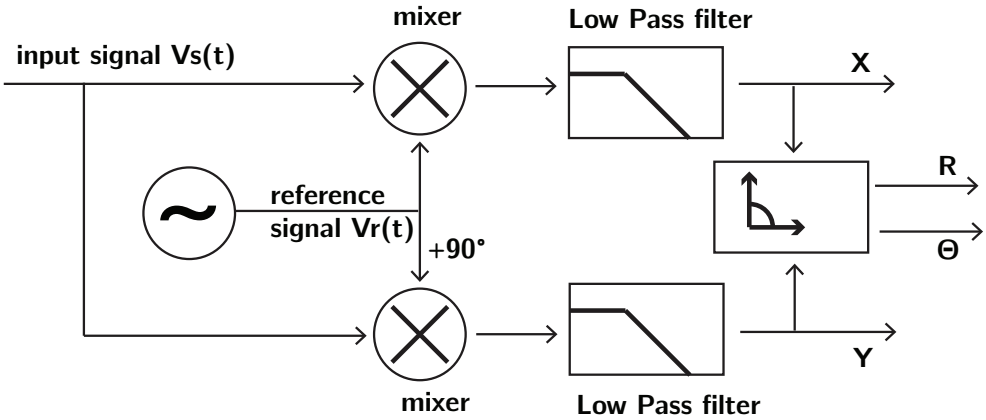

Figure 1.15: Schematic diagram of the operation principle for lock-in detection.

The outputs of the lock-in are the amplitude of oscillation a [m] and the phase shift ϕ [rad] of the tuning fork oscillation $a(t)$ with respect to the excitation voltage $E(t)$ at the excitation frequency ω. The properties of the lock-in are essentially determined by the cut-off frequency (or equivalently the bandwidth) and the order of the low pass filter (Fig. 1.15).

PLL

To measure the change in resonance frequency f of the tuning fork under an interacting force field, we use a Phase Lock Loop (PLL). In essence, the PLL tunes the excitation frequency f of the piezo-dither to keep a constant phase shift $\phi = \pi/2$ between the excitation signal and the tuning fork oscillation, allowing to systematically excite the tuning fork at its resonance frequency.

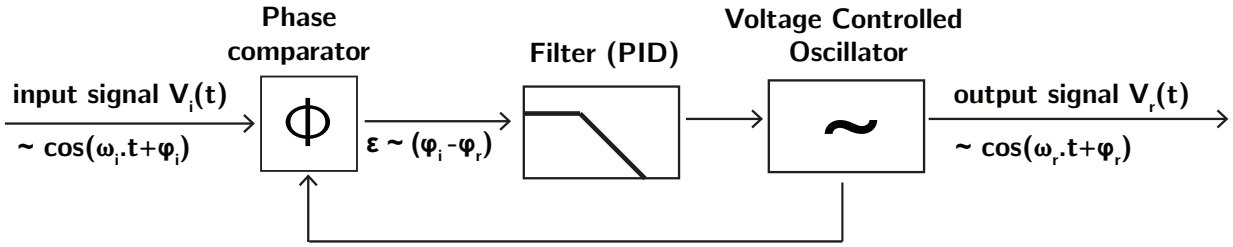

Figure 1.16: Schematic of the PLL operation principle.

A schematic diagram representation is given in Fig. 1.16. The phase shift between excitation and oscillation is measured via a lock-in amplifier. The bandwidth of the PLL is set by the gain of the PID filter and of the lock-in.

PID

Finally, we use an additional PID servo loop, which tunes the excitation voltage E of the piezo-dither to maintain constant the oscillation amplitude a of the tuning fork at the resonance. The bandwidth of the PID is again determined by the choice of the PID gain.

Frequency-modulation AFM techniques are implemented using a Phase Locked Loop, allowing to systematically excite the tuning fork at its resonant frequency. The shift in resonance frequency gives a direct measurement of the conservative force field applied on the tuning fork. The excitation of the piezo dither, i.e. the external force applied on the tuning fork is adjusted by an additional PID servo loop, to maintain a constant oscillation amplitude at the resonance. This excitation voltage gives a direct measurement of the dissipative forces applying on the tuning fork.

Other operation modes

Note that the tuning fork can also be used simply in amplitude modulation mode. This mode of operation is used in standard dynamic AFM imaging.

It remains possible to extract conservative and dissipative interactions in amplitude modulation mode, but at the price of approximations and more complex analysis of the phase and amplitude signals. As discussed in the first section of this chapter, amplitude modulation also leads to slow response time when using large quality factors. Due to the typically large quality factor of the resonance one also experiences a very quick loss in sensitivity in the presence of strong force gradients without frequency modulation techniques.

1.5 Limitation for dynamic force measurement

1.5.1 Fundamental limitations

We discuss in this section the limitation for dynamic force measurement with frequency modulation techniques [5, 28].

In frequency modulation AFM, the limitation for dynamic force measurement is related to the measurement of the oscillation period of the cantilever.

We can assume that the deflection $a(t)$ of the cantilever is subjected to a noise level δa. The deflection noise δa has two major contributions: thermal fluctuations of the cantilever $\delta a_{\text{thermal}}$ and instrumental noise $\delta a_{\text{detector}}$.

The oscillation period Θ of the oscillator can thus only be measured with accuracy $\delta\Theta$. The uncertainty in this oscillation period $\delta\Theta$ can be related to f_0 and δa as:

$$\delta\Theta = 2 \cdot \frac{\delta a}{2\pi f_0 a} \tag{1.29}$$

We have $f_0 = 1/\Theta$ and the relative error in frequency shift is given by:

$$\frac{\delta f}{f_0} = \delta\Theta f_0 = \frac{\delta a}{\pi a} \tag{1.30}$$

The two sources of noise on the oscillation frequency are statistically independent. We thus have

$$\delta f = \sqrt{\delta f_{\text{detector}}^2 + \delta f_{\text{thermal}}^2} \tag{1.31}$$

Thermal noise

For an oscillator submitted to white thermal noise, the spectral noise density $\tilde{a}$ [m.Hz^{-1}] for the amplitude is given by:

$$\tilde{a} = \sqrt{\frac{2k_{\text{B}}T}{\pi K f_0 Q}} \tag{1.32}$$

The thermal deflection noise is then given as a function of the measurement bandwidth:

$$\delta a = \sqrt{\frac{2k_{\text{B}}TB}{\pi K f_0 Q}} \tag{1.33}$$

This corresponds to a relative frequency noise:

$$\tilde{\delta f}_{\text{thermal}} = \sqrt{\frac{k_{\text{B}}TBf_0}{\pi K a^2 Q}} \tag{1.34}$$

At room temperature for an oscillation amplitude of 1 nm, frequency of 32 kHz and quality factor of the order of 10,000 one obtains a frequency noise density $\tilde{f}_{\text{thermal}} = 3 \cdot 10^{-4}$ Hz.Hz$^{-1/2}$.

Detector noise

In practice, the limitation for frequency measurement is given by the detector noise for the oscillation amplitude. One can characterize the detector by its noise density n_q [m.Hz$^{-1/2}$].

Eq. 1.30, characterizes the error in the frequency measurement for a bandwidth $B = f_0$ (i.e. over one oscillation cycle). In practice, the number of oscillation cycles which are available for frequency measurements is given by $N = f_0/B$ and the positional noise δa is related to the detector noise density n_q with $\delta a = n_q\sqrt{B}$.

We find

$$\delta f_{\text{detector}} = f_0 \frac{1}{N}\frac{\delta a}{\pi a} = \frac{n_q}{\pi a} B^{3/2} \tag{1.35}$$

The detector frequency noise $\delta f_{\text{detector}}$ has thus a strong dependence (power 3/2) on the measurement bandwidth B. The bandwidth B should thus be chosen properly, in order to keep low frequency noise while maintaining fast response time.

1.5.2 Experimental limitations

In practice force measurement are limited by the detector noise, as well as vibrations and thermal drift.

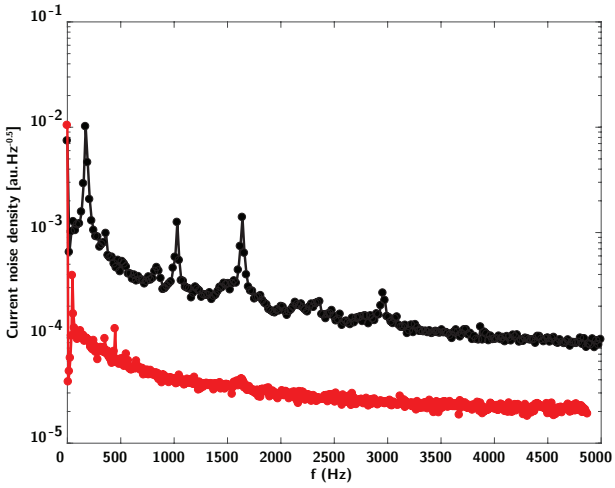

Figure 1.17: Current noise for a conductive gold tip touching a conductive gold substrate. **Black curve** corresponds to current noise density with 3 MechOnics, and camera motors turned on. One can clearly see mechanical resonance associated with vibration modes of the set-up. **Red curve** corresponds to current noise with one MechOnics, camera motors turned off and low pass filter on the control lines of the PiezoScanner.

Limitations in force measurements

For a bandwidth of 50 Hz for the PLL and PID, at an oscillation amplitude of 1 nm, for the 32 kHz resonance, one obtains a power spectrum density for the frequency shift of $\approx 10^{-3}$ Hz.Hz$^{-1/2}$, corresponding to a force gradient spectral density of ≈ 2 mN.m^{-1}.Hz$^{-1/2}$.

Similarly, the noise in the excitation signal due to the control loop for the excitation corresponds to a noise density for dissipative force of the order of 0.0024 nN.Hz$^{-1/2}$.

Vibration stability

Mechanical stability can also be crucial in some experiments.

For the experiments described in Chapter 3, we added low pass filters with cutoff frequency of 1 Hz to the control lines for the piezoscanner. We also found that reducing the number of MechOnics coarse approach motors leads to significant improvement in stability. Finally, all additional motors coupled to the breadboard (e.g. controlling the camera) were also turned off. Fig. 1.17 shows a comparison of the current noise for a conductive gold tip touching a conductive gold substrate in those two configuration.

Thermal drift

Thermal drift can also be an issue in the case of slow approach speeds. Letting the set-up at rest for several hours before performing experiments already leads to a significant reduction of thermal drift. For set-up left to rest several days, we could achieve thermal drift below 0.01 nm/s (Fig. 1.18).

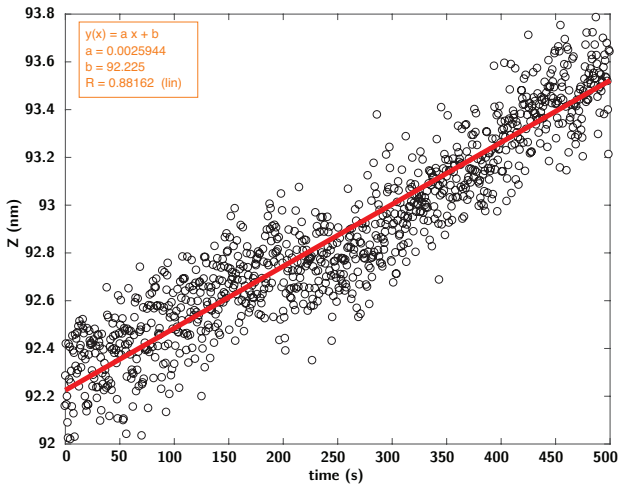

Figure 1.18: Drift in position, for regulation at constant frequency shift. The thermal drift is of order 0.003 nm/s

1.6 Conclusion

In this Chapter, we showed that the tuning fork based Atomic Force Microscope is a valuable tool for force measurement at the nanoscale. The main advantages of this device are:

1. **An ultrahigh stiffness, which leads to excellent mechanical stability e.g. when working in liquid environments or under strong attractive or repulsive force gradients.**
2. **Excellent mechanical resonator characteristics, conferring the tuning fork a large dynamic force sensitivity.**
3. **The ability to quantitatively disentangle conservative and dissipative forces acting on the tip of the tuning fork via frequency-modulation AFM techniques, enabling the tuning fork to work as a kind of nanorheometer.**

Using frequency-modulation techniques, we have a direct access to the conservative force gradient $-\partial F/\partial z$ [N/m] and dissipative forces F_{D} [N], or equivalently to the conservative and dissipative mechanical impedance Z' and Z'' [N/m] of the force field. Conservative force response is related to the frequency shift δf [Hz] of the resonance, and dissipative forces are related to the external excitation force (voltage) necessary to keep constant the oscillation amplitude of the tuning fork at resonance.

Bibliography

1. Castellanos-Gomez, a., Agraït, N. & Rubio-Bollinger, G. Dynamics of quartz tuning fork force sensors used in scanning probe microscopy. *Nanotechnology* **20,** 215502 (2009).
2. Garcia, L. *et al.* A micro-nano-rheometer for the mechanics of soft matter at interfaces. *Review of Scientific Instruments* **87** (2016).
3. Giessibl, F. J. Atomic resolution on Si (111)-(7\times 7) by noncontact atomic force microscopy with a force sensor based on a quartz tuning fork. *Applied Physics Letters* **76,** 1470–1472 (2000).
4. Giessibl, F. J. High-speed force sensor for force microscopy and profilometry utilizing a quartz tuning fork. *Applied Physics Letters* **73,** 3956–3958 (1998).
5. Giessibl, F. J. Advances in atomic force microscopy. *Reviews of Modern Physics* **75,** 949–983 (2003).
6. Hecht, B., Sick, B., Wild, U. P., Martin, O. J. F. & Pohl, D. W. Scanning near-field optical microscopy with aperture probes : Fundamentals and applications. **112,** 7761–7774 (2000).

7. Heyde, M., Kulawik, M., Rust, H. P. & Freund, H. J. Double quartz tuning fork sensor for low temperature atomic force and scanning tunneling microscopy. *Review of Scientific Instruments* **75,** 2446–2450 (2004).

8. Israelachvili, J. N. & Tabor, D. The Measurement of Van Der Waals Dispersion Forces in the Range 1.5 to 130 nm. *Proceedings of the Royal Society A: Mathematical, Physical and Engineering Sciences* **331,** 19–38 (1972).

9. Karraï, K. & Grober, R. D. Piezo-electric tuning fork tip-sample distance control for near field optical microscopes. *Ultramicroscopy* **61,** 197–205 (1995).

10. Kawai, S. *et al.* Superlubricity of graphene nanoribbons on gold surfaces. *Science* **351,** 957–961 (2016).

11. Kawai, S. *et al.* Direct quantitative measurement of the C==O···H-C bond by atomic force microscopy. *Science Advances* **3,** e1603258 (2017).

12. Klein, J. *Forces between mica surfaces bearing layers of adsorbed polystyrene in cyclohexane* 1980.

13. Klein, J. Forces between mica surfaces bearing adsorbed macromolecules in liquid media. *Journal of the Chemical Society, Faraday Transactions 1: Physical Chemistry in Condensed Phases* **79,** 99 (1983).

14. Kulawik, M. *et al.* A double lamellae dropoff etching procedure for tungsten tips attached to tuning fork atomic force microscopy/scanning tunneling microscopy sensors. *Review of Scientific Instruments* **74,** 1027–1030 (2003).

15. Labardi, M. & Allegrini, M. Noncontact friction force microscopy based on quartz tuning fork sensors. *Applied Physics Letters* **89,** 24–27 (2006).

16. McGraw, J. D., Niguès, A., Chennevière, A. & Siria, A. Contact Dependence and Velocity Crossover in Friction between Microscopic Solid/Solid Contacts. *Nano Letters* **17,** 6335–6339 (2017).

17. Melmed, A. J. The art and science and other aspects of making sharp tips. *Journal of Vacuum Science & Technology B: Microelectronics and Nanometer Structures* **9,** 601 (1991).

18. Meyer, s. M. R. W. E. *Noncontact Atomic Force Microscopy* ISBN: 978-3-642-62772-9 (2002).

19. Niguès, a., Siria, a., Vincent, P., Poncharal, P. & Bocquet, L. Ultrahigh interlayer friction in multiwalled boron nitride nanotubes. *Nature materials* **13,** 688–93 (July 2014).

20. Niguès, A. *Manipulation dans le micro / nanomonde : Dispositif haptique préhensile* PhD thesis (2006).

21. Rensen, W. H. J. *Tuning Fork Tunes: exploring new scanning probe applications* PhD thesis (2002).

22. Restagno, F., Crassous, J., Charlaix, É., Cottin-Bizonne, C. & Monchanin, M. A new surface forces apparatus for nanorheology. *Review of Scientific Instruments* **73,** 2292 (2002).

23. Ricchiuto, A. & Tozzi, A. Motion of a harmonic oscillator with sliding and viscous friction. *American Journal of Physics* **50,** 176–179 (1982).

24. Rodrigues, M. S. *Bringing light into the nanoworld. What can you do with an atomic force microscope on top of your synchrotron radiation sample holder ?* PhD thesis (2009).

25. Seo, Y., Jhe, W. & Hwang, C. S. Electrostatic force microscopy using a quartz tuning fork. *Applied Physics Letters* **80,** 4324–4326 (2002).

26. Tabor, D. & Winterton, R. H. S. The Direct Measurement of Normal and Retarded van der Waals Forces. *Proceedings of the Royal Society A: Mathematical, Physical and Engineering Sciences* **312,** 435–450 (1969).

27. Vitorino, M. V., Vieira, A. & Rodrigues, M. S. Effect of sliding friction in harmonic oscillators. *Scientific Reports* **7,** 1–7 (2017).

28. Wiesendanger, R., Giessibl, F. J. & Morita, S. *Noncontact Atomic Force Microscopy* 410. ISBN: 3642014941, 9783642014949 (2009).

Chapter 2

Capillary Freezing in Ionic Liquids

Contents

In this Chapter, we use nanorheological measurements to explore the properties of ionic liquids in nanometric confinement. We unveil a dramatic change of the ionic liquid towards a solid-like phase below a threshold thickness, pointing to a capillary freezing transition in confinement. This threshold thickness is found to be intimately related to the metallic nature of the confining materials, with more metallic surfaces facilitating freezing. This behavior is interpreted theoretically in terms of the shift of the freezing transition, taking into account the influence of the electronic screening on ionic liquid wetting of the confining surfaces, as described by a simple Thomas-Fermi approach.

This Chapter is based on the following articles:

- Comtet, J., Niguès, A., Kaiser, V., Coasne, B., Bocquet, L., & Siria, A. Nanoscale capillary freezing of ionic liquids confined between metallic interfaces and the role of electronic screening. *Nature materials*, 16**(6)**, 634. (2017).

- Kaiser, V., Comtet, J., Niguès, A., Siria, A., Coasne, B., & Bocquet, L. Electrostatic interactions between ions near Thomas–Fermi substrates and the surface energy of ionic crystals at imperfect metals. *Faraday discussions*, 199, 129-158. (2017).

2.1 General Context

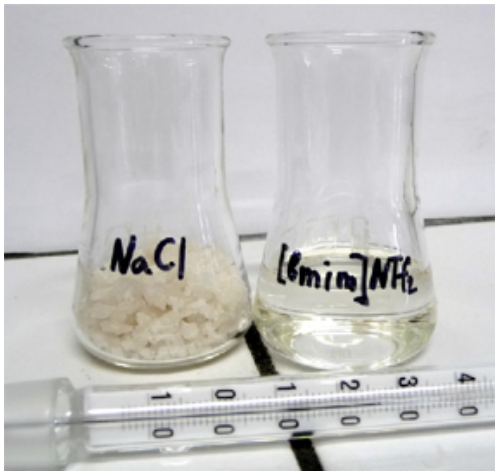

Figure 2.1: Table salt NaCl and the ionic liquid 1-butyl-3-methylimidazolium bis(trifluoromethylsulfonyl)imide at 27 °C.

Room Temperature Ionic Liquids are liquid salts in the ambient (Fig. 2.1). They are new materials with peculiar properties, leading to a wealth of emerging applications for energy storage, lubrication and catalysis [27, 36, 60]. As solvent-free electrolytes composed solely of ions, ionic liquids also challenge the fundamental framework of electrolytes and of the liquid state.

Applications: from supercapacitor to lubrication

The large electrochemical window, low vapor pressure, thermal stability and low melting point of ionic liquids make them ideal candidates for their use in applications related to energy storage, for example in supercapacitors [5, 57]. Fig. 2.2 shows a schematic of a supercapacitor composed of two porous carbon electrodes immersed in an electrolyte. The principal reason for the use of ionic liquids in supercapacitors is their large electrochemical window, of up to 5 V [22] (to be compared to the 1 V electrochemical window of water based electrolytes) which can maximize the energy $1/2 \cdot C \cdot \Delta V^2$ capacitively stored using those electrolytes (with ΔV [V] the potential drop and C [F] the capacitance)

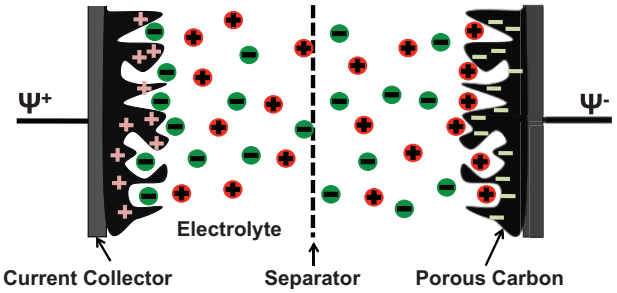

Figure 2.2: Cross-sectional section of a supercapacitor. The application of a potential drop between the two electrodes leads to accumulation of ions on the electrodes [38]

Due to their strong interaction with surfaces, ionic liquids are also promising materials for applications related to friction, and have shown unexpected lubricating and anti-wear properties [42, 58]. They are particularly interesting in the context of boundary lubrication, as they can prevent direct contacts between sliding surfaces [34, 50]. Ionic liquids also raise significant interests in the context of active or voltage controlled lubrication, with recent experimental and theoretical work showing that their frictional properties could be tuned and controlled by the application of electric fields [14, 16, 46].

Fundamental challenges

The unique properties of ionic liquids result from the competition of strong electrostatic interactions between ions with properly designed molecular structure to avoid crystallization at room temperature. This inhibited crystallization stems from the relative large ion size (which reduces electrostatic interactions), the asymmetry between the anion and the cation, and conformational entropic effects of the molecules. Ionic liquids are thus a prototype for dense electrolytes, composed of pure ions. Interestingly, at such densities, standard mean-field response, such as Poisson-Boltzmann theory, which constitutes the toolbox of dilute electrolytes, cannot account for the structure of the ionic liquid close to surfaces.

We can grasp the peculiarities associated with ionic liquids by evaluating two characteristic lengths. The Bjerrum length, which characterizes the typical inter-ionic distance at which electrostatic interactions start to overcome thermal fluctuations can be expressed as $\lambda_B = e^2/(4\pi\epsilon k_B T)$, with e the elementary charge, ϵ the dielectric constant and $k_B T$ the thermal energy. In standard ionic liquids, this length is of the order of 5 to 10 nm, i.e. up to 10 times the ion pair size, characterizing the strong electrostatic interactions at play in those liquids. To compare, the Bjerrum length is only of the order of 0.7 nm in water.

Second, the expected Debye screening length for the electric field in the electrolyte is of the order of $\lambda_D = \sqrt{\epsilon k_B T/2c_0 e^2}$ with c_0 the concentration of charge carrier (here ions).

This screening length is of order $0.1 - 0.6$ nm in ionic liquids, i.e. smaller than the ion pair size and than the Bjerrum length. As a comparison, the Debye screening length is of order $1 - 100$ nm for dilute aqueous electrolytes ($c < 100$ mmol/L).

Those estimates highlight the peculiar nature of ionic liquids as dense disordered liquid systems, controlled by strong electrostatic interactions between ions.

Behavior of ionic liquids at interfaces and in confinement

Like several other liquids, ionic liquids tend to adopt ordered layered structures extending over several molecular lengths parallel to surfaces. These molecularly ordered structures can be probed mechanically via SFA or AFM. Clear mechanical signatures of this molecular ordering close to surfaces have been reported [10, 26, 28, 44, 51].

Interestingly, several other studies have also reported changes in the mechanical properties of confined ionic liquid at distances exceeding several molecular lengths. Hoth and coworkers reported layering of ionic liquid with AFM at distances up 10 nm from surfaces [29]. Bou-Malham and Bureau reported viscosity enhancement for ionic liquids confined to 20 nm between charged Mica surfaces [10]. Solid-like behavior of ionic liquid confined between silica surface to distances of 10 nm were reported by Ueno et al. [56]. Solid structures with thickness of tens of nanometers were grown by successive nanoconfinements between mica surfaces in Jurado et al. [30]. Similarly, solid-like terraces were reported by Bovio et al. on silica, mica and HOPG surfaces, for ionic liquids deposited by dropcasting techniques [11, 12, 59].

Due to the dominant role of electrostatic forces in ionic liquids, one may anticipate even more peculiar behavior of ionic liquids at metallic surfaces [21, 32, 39, 47]. 2D like ordering of ionic liquids at electrified interfaces have indeed been revealed by AFM and STM studies [6, 13, 17, 18, 52, 59]. Structures of the order of 1000 nm have also been reported via spectroscopic methods at silver and gold surfaces, independently of surface chemistry [3]. Finally, there are some reports in which the melting points of ionic liquids has been found to increase when confined in nano porous conducting matrices like silver and single and multi-wall carbon nanotube [48].

Confinement therefore opens an interesting window on the physics of ionic liquids and their interaction with the confining interfaces [43]. In particular, due to the dominant role of electrostatic forces, one may anticipate that the metallic nature of the confining surfaces should affect the static and dynamic properties of confined ionic liquids. Such relationships have not been explored up to now.

2.2 Experimental Set-up

2.2.1 General Set-up

We present in Fig. 2.3 a sketch of the experimental set-up. We glue the electrochemically etched tungsten tip of end radius from 50 nm to 2.5 μm to the quartz tuning fork. The tip of the tuning fork is immersed in a drop of liquid deposited on the substrate. The probed liquid is confined between the oscillating tungsten tip and substrates of various nature. Importantly, the entire set-up is placed in a vacuum chamber at a pressure of approximately 10^{-6} mbar, to prevent contamination of the liquid with ambient water vapor. The fact that we operate in vacuum might be important, as the mechanical properties of ionic liquids under confinement have been found to be strongly dependent on environmental

humidity [31].

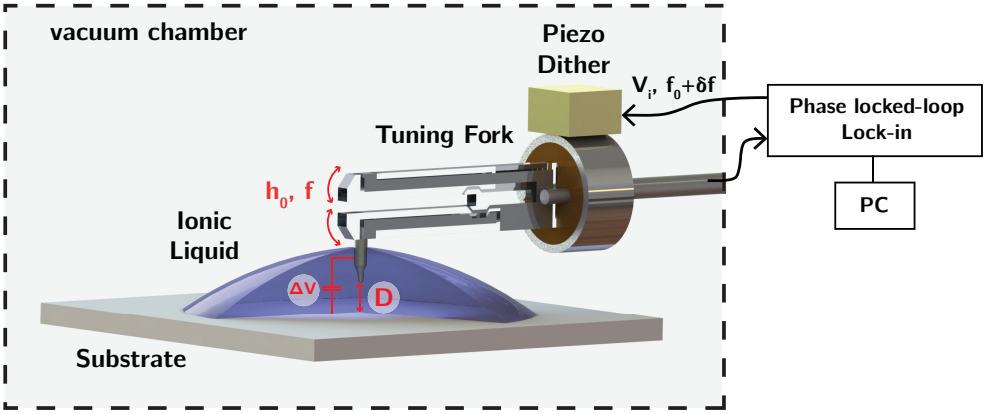

Figure 2.3: **Experimental Set-up and schematic of the experiment**. An etched tungsten tip of end radius of curvature R between 50 nm and 5 μm is glued to the tuning fork, and immersed in the ionic liquid. The substrate can be biased with respect to the tip with a potential difference ΔV. The experimental set-up is placed in a vacuum chamber at a pressure of $\approx 10^{-6}$ mbar.

2.2.2 Ionic Liquids

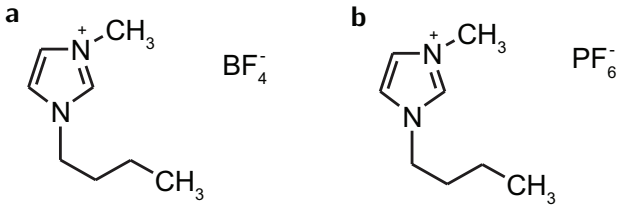

Figure 2.4: **(a)** 1-Butyl-3-methylimidazolium tetrafluoroborate (BmimBF4) **(b)** 1-Butyl-3-methylimidazolium hexafluorophosphate (BmimPF6).

The ionic liquids under investigation are BmimBF4 and BmimPF6 (Sigma Aldrich, 98.5% purity) (Fig. 2.4). BmimBF4 is the main ionic liquid used throughout this study, and a comparison with BmimPF6 is made in Section 2.6.2. The thermodynamic and physical properties of these ionic liquids are summarized in Tables 2.1 and 2.2.

Ionic liquids are filtered through a 100 nm hole teflon membrane before use. A drop is deposited on the substrate and the AFM tungsten tip is immersed in the liquid. The liquid is left at rest in the vacuum chamber at least for 12h to remove water impurities. The substrate can be biased with respect to the tip by a potential difference ΔV. To verify the high purity of the ionic liquid, we systematically check the absence of long-term electrochemical current when applying a potential drop between -1.8 V and 1.8 V, which is smaller than the electrochemical window for those liquids [41].

BmimBF4		
Parameter	Explanation	Value
T_B	Bulk freezing temperature	-71° C [8]
L_h	Latent heat of melting	47 kJ/kg [8]
ρ	Liquid phase density	1.21 g/mL
v_m	Molar volume	187 mL/mol
$2a$	Lattice constant	0.67 nm
η	Viscosity	150 mPa.s

Table 2.1: Summary of BmimBF4 bulk properties. Lattice constant of the crystalline phase can be defined as $2a = (v_m/\mathrm{Na})^{1/3} = 0.67$ nm with $v_m = 187$ mL/mol the ionic liquid molar volume.

BmimPF6		
Parameter	Explanation	Value
T_B	Bulk freezing temperature	7° C [55]
L_h	Latent heat of melting	19.9 kJ/kg [55]
ρ	Liquid phase density	1.38 g/mL
v_m	Molar volume	205.9 mL/mol
$2a$	Lattice constant	0.7 nm
η	Viscosity	300 mPa.s

Table 2.2: Summary of BmimPF6 bulk properties.

2.2.3 Substrates

We have performed experiments by confining the liquid between various substrates, namely mica, HOPG, doped silicon, and platinum, whose characteristics are described in the following. Note that doped silicon and the tungsten tips may be coated by natural oxide layers of up to 1 nm in thickness [4, 40]. However, this length remains much smaller than the typical length at which the phenomena under investigation occurs, in the range of tens of nanometers.

Substrate Preparation

The samples were prepared and characterized before experiments to discard any artifacts in our measurements. Sample preparation and cleaning were done in a cleanroom environment, and substrates and ionic liquids were immediately transferred to the vacuum chamber.

- **Mica**: Mica was purchased from Sigma Aldrich and cleaved right before use.
- **HOPG**: HOPG was purchased from Sigma Aldrich and cleaved with adhesive tape right before use.
- **Doped Silicon:** Silicon (100) P-Bore doped, was purchased from Sil'Tronix. Substrates were sonicated in acetone and isopropanol, and dried with nitrogen before use.

- **Platinum:** Platinum was vacuum deposited on intrinsic (100) Silicon with native oxide using a 5 nm thick nickel adhesion layer. The final thickness of the Pt film is ≈ 100 nm. The substrates were sonicated in acetone and isopropanol, and dried with nitrogen before use.

Substrate Topography

The surface topography of the different substrates has been firstly characterized in air using Atomic Force Microscopy. The samples have been prepared and cleaned following the same procedure as during experiments with ionic liquid. In Fig. 2.5 we present the images for the 4 different materials. Mica surface is atomically flat with a rms roughness below 0.3 nm. HOPG present the standard terrace like feature of a multilayer surface: on the terrace the surface is atomically flat with a rms roughness below 0.3 nm. Doped Silicon and Platinum presents a very uniform and flat surface with a with a rms roughness below 0.3 nm for Doped Silicon and below 0.8 nm for Platinum

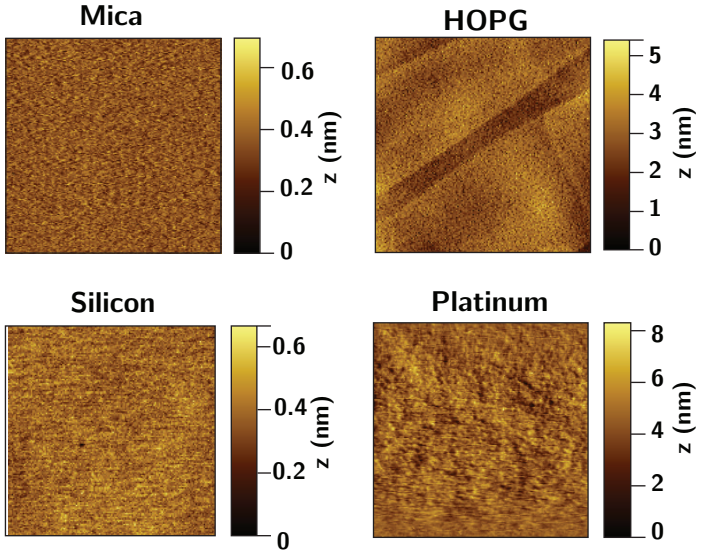

Figure 2.5: Atomic Force Microscope Topography in air of the four different substrates. Scan size is 3×3 μm.

Conductivity, Carrier density and Thomas-Fermi length

As we will show in the following, the electronic properties of the confining substrates might determine strongly the behavior of the confined liquid. We characterize here the electronic screening in the substrate by the Thomas-Fermi screening length for the electric field.

The Thomas-Fermi wave vector k_{TF} can be expressed in terms of the density of states $D(E_F)$ at the Fermi level E_F, elementary ionic charge e and dielectric permittivity ϵ_0:

$$k_{\mathrm{TF}}^2 = \frac{e^2}{\epsilon_0} D(E_F) \tag{2.1}$$

To obtain a coarse estimation of the Thomas-Fermi length for the three conductive substrates, we assume that they can be described as ideal 3D Fermi gas, for which

$$D(E) = \frac{3n}{2E} \text{ and } E_F = \frac{\hbar^2}{2m_e}(3\pi^2 n)^{2/3} \tag{2.2}$$

where n is the carrier density, $\hbar$ is Planck's constant and m_e is the electron mass. This gives:

$$\ell_{\mathrm{TF}} \approx \frac{1}{2}\left(\frac{a_0^3}{n}\right)^{1/6} \text{ with } a_0 = \frac{4\pi\epsilon_0\hbar^2}{m_e e^2} \approx 0.57 \text{ Å} \tag{2.3}$$

The carrier density and the Thomas-Fermi length are then estimated as follow:

- **Mica:** Mica is a band-gap insulator, for which the Thomas-Fermi length $\ell_{\mathrm{TF}} \to \infty$.
- **HOPG:** the carrier concentration is approximately equal to 10^{-4} per carbon atoms [7]. From HOPG density, we find an atomic density of $1.14 \cdot 10^{29}$ m^{-3}. We thus obtain a carrier density of $n(\mathrm{HOPG}) = 1.1 \cdot 10^{-24}$ m^{-3}. Conductivity in Table 2.3 corresponds to the graphite out-of-plane conductivity [45].
  The corresponding Thomas-Fermi length is $\ell_{\mathrm{TF}} \approx 3.6$ Å.
- **Doped Silicon:** using standard conductivity/carrier charts [54], we estimate a dopant density of $n(\mathrm{Si}) = 1 - 3 \cdot 10^{26}$ m^{-3}, taking substrate conductivity given by the seller (0.5-0.8 mΩ.cm).
  The corresponding Thomas-Fermi length is $\ell_{\mathrm{TF}} \approx 1.5$ Å.
- **Platinum:** carrier density is equal to atomic density, calculated as $n(\mathrm{Pt}) = \rho(\mathrm{Pt})/N_A = 6.62 \cdot 10^{28}$ m^{-3} where ρ_{Pt} [g/cm^3] is Platinum density.
  The corresponding Thomas-Fermi length is $\ell_{\mathrm{TF}} \approx 0.5$ Å.

We summarize the properties of the samples used in our experiments in Table 2.3.

Substrate	Roughness (RMS)	Conductivity	Carrier Density	TF-length ℓ_{TF}
Mica	< 0.3 nm	insulator	-	$\ell_{\mathrm{TF}} \to \infty$
HOPG, ZYA grade	< 0.3 nm	300 mΩ.cm	$1.1 \cdot 10^{24}$ /m^3	$\ell_{\mathrm{TF}} = 3.6$ Å
Doped (100) Silicon	< 0.3 nm	0.5-0.8 mΩ.cm	$1 - 3 \cdot 10^{26}$ /m^3	$\ell_{\mathrm{TF}} = 1.46 - 1.75$ Å
Platinum	≈ 0.8 nm	0.1 mΩ.cm	$6.6 \cdot 10^{28}$ /m^3	$\ell_{\mathrm{TF}} = 0.55$ Å

Table 2.3: Summary of Substrate Properties.

2.2.4 Tip

A chemically etched tungsten tip with a radius in the range 50 nm to 5 µm is glued with conductive epoxy to one prong of the tuning fork. In Fig. 2.6, we show a SEM image of a typical tungsten tip used during the experiments. The end diameter is measured here as D = 1.85 µm and the tip is perfectly smooth at the end.

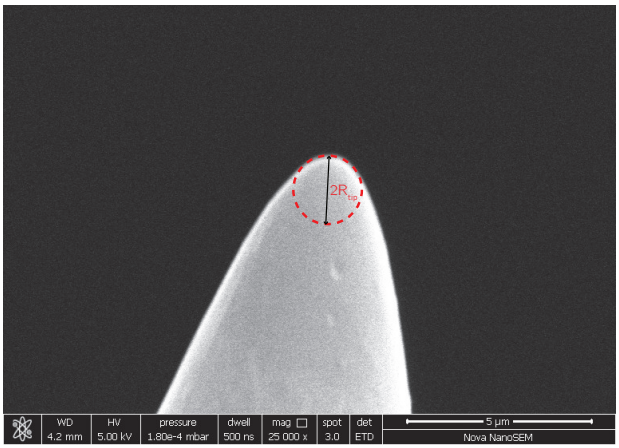

Figure 2.6: SEM image of typical tungsten tips used in this study. The end diameter is measured here as $D = 1.85$ µm and the tip is perfectly smooth at the end. Typical tip diameters used in our experiments range from 1.5 to 5 µm.

2.3 Solid-like response and prewetting

2.3.1 Dissipation of an AFM tip oscillating in a viscous fluid

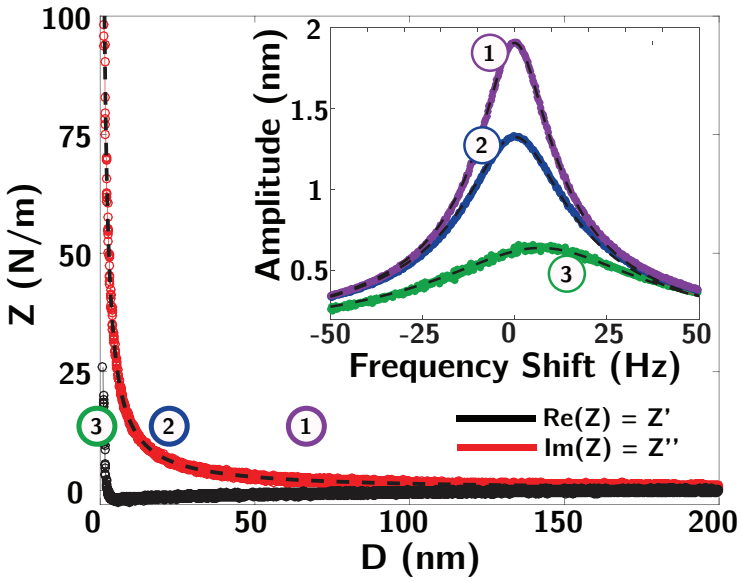

Figure 2.7: **Benchmark on a silicon oil.** Nanorheological measurement on a silicon oil confined between a tungsten tip and a mica sample, showing the variation of conservative (Z' - black) and dissipative (Z" - red) mechanical impedance; black dotted line is a fit based on Eq. 2.4. Inset shows typical resonance curves of the tuning fork with the tip immersed in the liquid and far from the surface (1), close to the surface (2) and in contact with the substrate (3).

As shown in Fig. 2.7, the experimental set-up has been fully benchmarked using a newtonian silicon oil with viscosity $\eta \approx 0.1$ Pa.s, comparable to the viscosity of the ionic liquid used in this study.

Reynolds Force

Quantitatively, the increase of dissipation Z'' with decreasing confinement D for a viscous newtonian fluid sheared under an oscillating sphere can be described by the Reynolds force [33]:

$$Z''_{\text{Reynolds}}(D) = \frac{6\pi\eta R^2 \cdot 2\pi f_0}{D} \tag{2.4}$$

where R is the radius of curvature of the tip, $\eta \approx 0.1 - 0.3$ Pa.s the bulk viscosity of the confined liquid, $f_0 \approx 32$ kHz the oscillation frequency and D [nm] the distance between the tip and the substrate. This expression assumes no slip at the liquid/substrate interfaces, which is expected for strongly interacting systems such as ionic liquids [9], or for the viscous silicon oil.

Dissipation of the AFM tip

When the tip is oscillating close to the surface, the viscous impedance $Z''(z)$ varies as: $Z''(z) = Z''_{\text{Reynolds}}(z - z_0) + Z''_0(z)$ with z_0 the absolute position of the substrate, $D = z - z_0$ the distance between the tip and the surface. The second term $Z''_0(z)$ characterizes viscous dissipation along the immersed tip and at the meniscus, which can be in principle dependent on the tip/substrate position. Over the course of an approach to the substrate (≈ 300 nm), this term varies approximately linearly with position, i.e. $Z''_0(z) \sim z$. This second term is accordingly taken into account for obtaining the expression of the Reynolds dissipation, and the absolute position of the tip with respect to the hydrodynamic origin.

We show in the following only dissipative impedance corrected for this additional dissipation.

2.3.2 Approach curve in the ionic liquid

Long-range hydrodynamic variations

We plot in Fig. 2.8a the typical variation of the elastic $Z' = \text{Re}(Z^*)$ (black curve) and dissipative $Z'' = \text{Im}(Z^*)$ (red curve) parts of the mechanical impedance, as the tungsten tip approaches a HOPG surface in the ionic liquid. Far from the substrate - zone (i) - the elastic response is $Z' \approx 0$ within the experimental precision. One can observe a minute attractive component reminiscent of long-ranged forces recently reported in several SFA experiments [23–25, 49]. The dissipative component Z'' increases gently as the confinement thickness decreases; quantitatively, the increase of Z'' with decreasing confinement D can be described by the Reynolds dissipative response of a viscous newtonian fluid sheared under an oscillating sphere [33] $Z''(D) = 6\pi\eta R^2 \cdot 2\pi f_0/D$ (see Eq. 2.4). Fitting this initial increase in dissipation allows us to estimate the absolute position D between the confining tip and the surface.

Solid-like response

As shown in Fig. 2.8a, in ionic liquids, before reaching the hydrodynamic "zero" $D \to 0$, both the elastic Z' and dissipative part Z'' of the response suddenly diverge at a critical confinement $D = \lambda_S$. This occurs for a confinement D in the range of a few tens of nanometers, depending on the substrate. We have changed the tip oscillation amplitude h_0 over one decade, between 0.1 nm and 1 nm, verifying that λ_S does not depend on oscillation amplitude and shear rates. Within our experimental precision, the retract and approach curves over one approach are similar, showing no or negligible hysteresis.

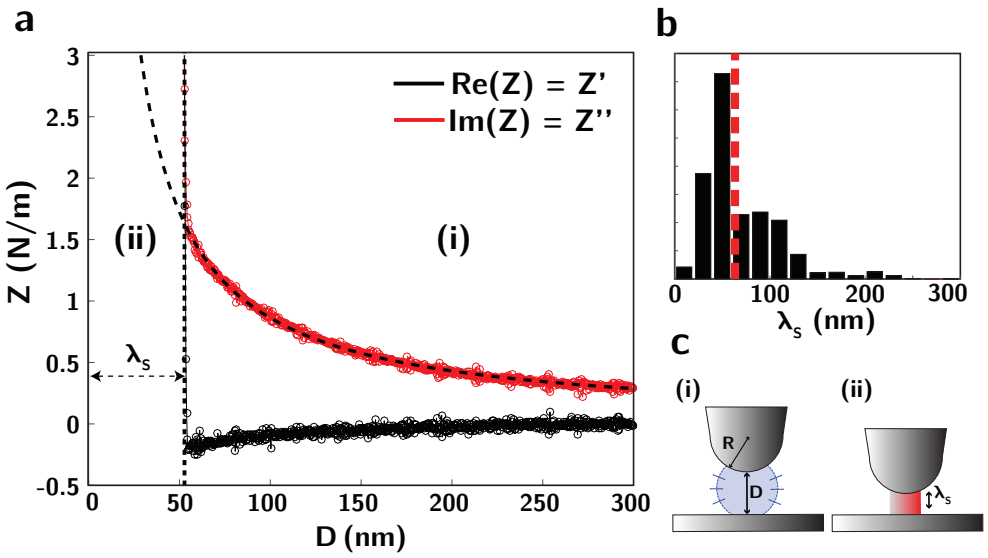

Figure 2.8: **Confinement induced freezing transition (a)** Real (Z', black) and complex (Z'', red) part of the mechanical impedance characterizing conservative and dissipative response of the liquid, versus tip-substrate position D, performed on a HOPG sample. The origin of the tip-substrate position is defined as the hydrodynamic zero obtained by fitting Z'' with Eq. 2.4. Upon a critical confinement distance λ_S, Z^* changes from a liquid-like response to a solid-like response, characterized by the onset of an elastic contribution (Z', black dots) and a sharp increase of the dissipation (Z'', red dots). **(b)** Distribution of λ_S on HOPG; $\approx$ 12,000 cycles were performed, over 18 distinct locations. Red vertical line is the mean of the distribution. **(c)** Sketch of the freezing induced by confinement: upon a critical confinement the ionic liquid changes from liquid (i) to solid-like (ii).

This strong repulsive elastic response (with $Z' \approx 30$ N/m) shows that the ionic liquid can now sustain a yield stress of order $\tau \approx Z'h_0/\pi R^2 \approx 1$ kPa, providing a clear signature of the solid-like response of the confined ionic liquid for $D < \lambda_S$. This behavior was found repeatedly when performing approach and retract cycles of the tip, either at the same or at distinct locations; typically $\approx$ 10,000 cycles were performed for each material, over $\approx$ 20 distinct locations. We measured accordingly the distribution of threshold confinement thickness, as reported in the inset of Fig. 2.8b for HOPG, allowing to extract the mean transition thickness, found to be $\lambda_S \simeq 60$ nm for HOPG.

Going further, the same phenomenon was observed for the various substrates under investigation, Mica, HOPG, doped Silicon and Platinum, with a mean transition thickness λ_S increasing in the order: Mica (15 nm) < HOPG (60 nm) < doped Silicon (110 nm) < Platinum (160 nm). Interestingly this order corresponds to substrates with increasing metallic character, as for example characterized by the conductivity, from the insulating Mica to the highly conductive Platinum (see Fig. 2.10).

2.3.3 Prewetting

As a first interpretation of the approach curve shown in Fig. 2.8a, one may infer the presence of solid layers pre-existing on the surface of the substrates. To explore this assumption, we have performed AFM images of the surfaces using sharp tips with 10 - 50 nm of radius of curvature (Fig. 2.9). While in vacuum, the substrates surface appear

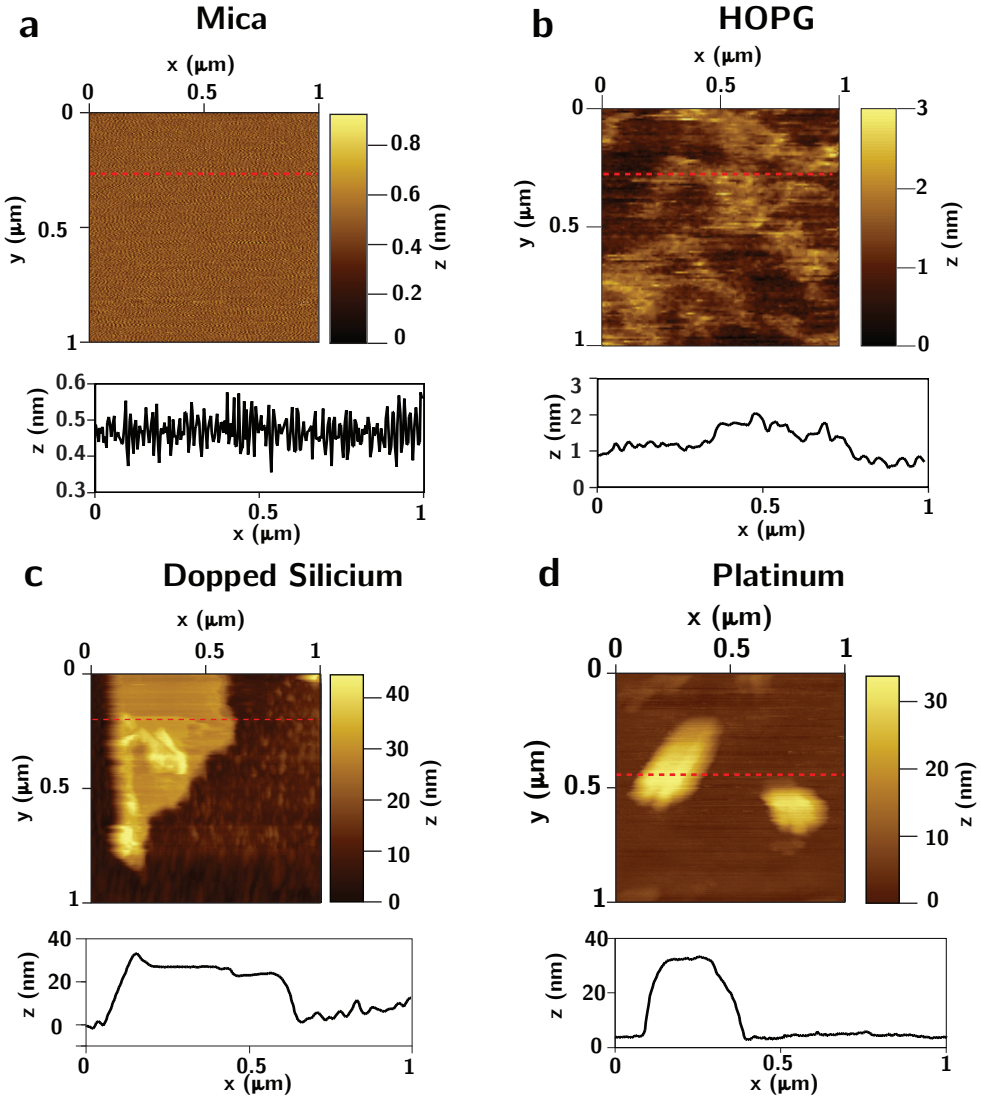

Figure 2.9: Atomic Force Microscope Topography in Ionic Liquid of the four different substrates: **(a)** Mica, **(b)** HOPG, **(c)** Doped Silicon and **(d)** Platinum.

atomically smooth on micrometric scales – with a typical rms roughness between 0.3 nm and 1 nm depending on the substrate (Fig. 2.5) – one indeed observes solid-like terrace structures on the surfaces when immersed in the ionic liquid. This thickness is measured below 1 nm for HOPG and typically in the range of $\sim 20 - 30$ nm for doped silicon and platinum; no such terrace is evident on Mica (Fig. 2.9). Such structures are reminiscent of observations using STM and AFM imaging [13, 17, 18, 59]. That such thick structures are present on the substrate surfaces is unexpected *per se* and raises the question of the prewetting of the surfaces by the ionic liquid, and the role of the metallic nature of the substrates on this prewetting. We note however that the characteristic height of these solid "prewetting" films is much smaller than the critical thickness at which the transition occurs for each substrates (Fig. 2.10a, blue dots). Accordingly an alternative thermodynamic explanation for the solid-like response of the liquid shown in Fig. 2.8 should be sought.

2.4 Confinement-induced freezing transition

2.4.1 Gibbs-Thompson effect

Looking at Fig. 2.8a, the drastic change in both elastic response and dissipation from $D > \lambda_S$ to $D < \lambda_S$ would actually rather suggest a complete confinement induced phase change, with a freezing of the confined ionic liquid inside the gap. A confinement induced phase transition is expected when the unfavorable bulk free energy is balanced by favorable (wetting) surface contributions, thus stabilizing the unfavored phase in confinement. This results in a shift for the phase transition, as observed for capillary condensation (the shifted liquid-gas phase transition) or capillary freezing (shifted crystallization) [2]. The balance of free energy leads to the so-called Gibbs-Thompson equation, which characterizes the critical confinement λ_S at which the free energies of the liquid and solid phase become equal [2]:

$$\Delta T = T_C - T_B = 2\frac{T_B \Delta\gamma}{\rho\, L_h\, \lambda_S} \text{ with } \Delta\gamma = \gamma_{wl} - \gamma_{ws} \tag{2.5}$$

where $\Delta T = T_C - T_B$ is the shift in transition temperature, in confinement T_C as compared to the bulk transition occurring at T_B. For the specific ionic liquid used here, $T_B = -71°$ C; γ_{wl} and γ_{ws} are the surface energy of the liquid and solid phase with respect to the wall/substrate, $\rho = 1.21$ g/mL the density of the liquid phase and $L_h = 47$ kJ/kg the latent heat of melting [8] (see Table 2.1). Eq. (2.5) shows that if wetting of the solid-phase on the substrate is favored compared to that of the liquid ($\gamma_{ws} < \gamma_{wl}$) the freezing temperature of the confined phase T_C is larger than the bulk freezing temperature T_B ($T_C > T_B$ in Eq. 2.5). Putting numbers, one gets $T_C \sim 25°$ C for a an ionic liquid confined in a gap of ~ 20 nm with $\Delta\gamma \sim 0.3$ J/m^2 (anticipating on the values below). In other words, the ionic liquid may freeze in nanoconfinement at room temperature. In this scenario, the distribution of confinement length measured experimentally, see inset if Fig. 2.10, can be understood as a signature of activation due to the first order character of the freezing transition, potentially facilitated by the prewetting phase on the substrate.

2.4.2 Dependence on the metallicity of the substrate

A delicate question though is to understand the variations with the metallic nature of the substrate. Following the argument above in terms of the shifted liquid-solid transition, this raises the question of the surface energy of the solid (crystal) phase with the substrate and how it is influenced by the metallic character of the substrate. Physically, one may propose a simple explanation in terms of image charges. To highlight the argument, let us consider a semi-infinite ionic crystal at the interface with a perfect metal, as sketched in Fig. 2.10b. The network of image charges builds a crystal structure with a (nearly) perfect symmetry with respect to the real upper half-lattice. Accordingly one expects the electrostatic contribution to the surface free energy to (nearly) vanish, as the system behaves as a single bulk lattice: $\gamma_{ws}^{elec} \to 0$. This requires of course a perfectly symmetric crystalline structure and this cancellation is not expected to occur for insulating substrates, or for disordered liquid phases. In other words, the (semi-infinite) ionic crystal has a lower surface energy at the interface with a metal wall as compared to an insulating substrate: $\gamma_{ws}^{insulating} > \gamma_{ws}^{metal}$. This shows that the crystal phase is favored on metallic surface as compared to an insulating one and the Gibbs-Thompson equation (Eq. 2.5) accordingly

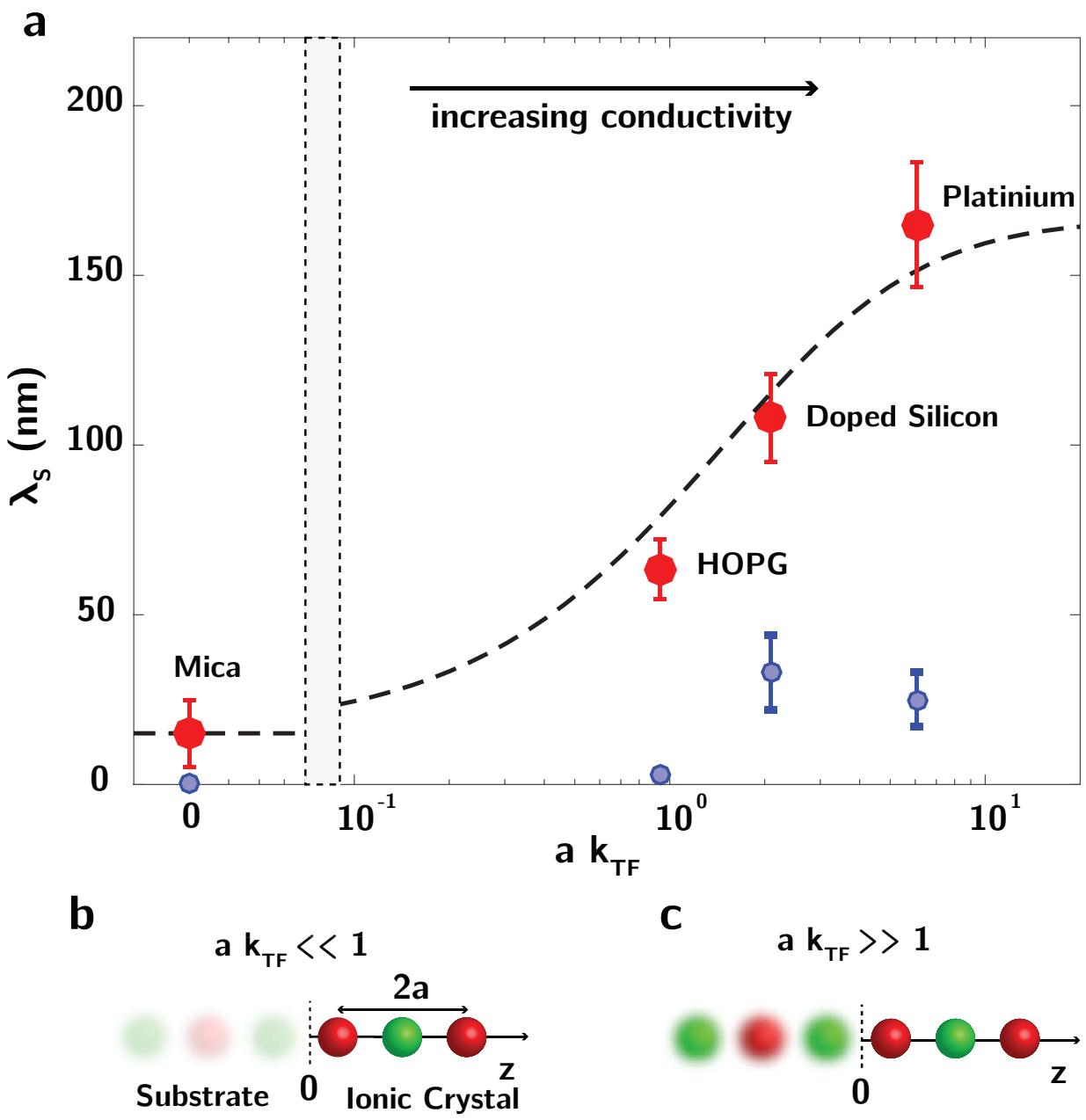

Figure 2.10: **Effect of substrate electronic properties on the freezing transition. (a)** Red dots: Variation of the mean solidification length (red dots) λ_S on Mica and three conductive substrates: HOPG, Doped Silicon and Platinum versus the normalized Thomas-Fermi wavevector, $a \cdot k_{TF}$, with $2a$ the typical ionic crystal lattice constant. Error bars indicate standard deviation for Mica and standard error for the three conductive substrates, with $N \approx 20$ the number of positions investigated in each substrates. Blue open dots represent the typical size of the preexisting solid layers measured with a sharp tip. Error bar represents standard deviation of estimated height. Dotted line is the prediction from Eq. 2.9. **(b, c)** Schematic representation of the ionic crystal close to an insulator ($\alpha k_{TF} \ll 1$, (b)) and a perfect metal ($\alpha k_{TF} \gg 1$, (c)) for which image charges induced in the substrate decrease the energy of the system.

implies that the threshold confinement for the freezing transition should be larger with metal as compared to insulating confining surfaces.

2.5 Role of electronic screening

2.5.1 Electronic screening by a Thomas-Fermi metal

In order to account for the non-ideal metallic nature of the confining walls, one should model the electronic screening inside the substrates. To this end, we use the simple Thomas-Fermi framework, based on a local density approximation for the free electrons gas [37]. This description provides a simple screening equation for the electric potential V (V) in the metal, where the screening length $\lambda_{\rm TF} = 1/k_{\rm TF}$ [m] characterizes the typical length over which a defect charge is screened in the metal and is defined in terms of the density of states at the Fermi level, according to $k_{\rm TF}^2 = 4\pi e^2 \frac{\partial n}{\partial \epsilon_F}$; n_T the state occupation and ϵ_F the Fermi level (see Section 2.2.3). The limit of large $k_{\rm TF}$ (small $\lambda_{\rm TF}$) corresponds to the perfect metallic case for which V is uniformly zero.

2.5.2 Influence of the electronic screening on charges in the ionic liquid

The electronic screening therefore modifies the interactions of charge close to the liquid-wall interface. The Green function Ψ for the electrostatic interaction, replacing the Coulomb interaction, obeys equations:

$$\Delta\psi = -\frac{Q}{\epsilon}\delta(\mathbf{r}-\mathbf{r_0}) \text{ for } z>0 \tag{2.6}$$

$$\Delta\psi - k_{\rm TF}^2\psi = 0 \text{ for } z<0 \tag{2.7}$$

This allows us to calculate the energy of a semi-infinite ionic system in the presence of the metal wall, as $U = \frac{1}{2}\int \mathbf{dr}\rho_{\rm c}(\mathbf{r})\psi(\mathbf{r})$, with $\rho_{\rm c}$ the charge density. For the crystal phase $\rho_{\rm cr}(\mathbf{r}) = Q\sum_n (-1)^n \delta(\mathbf{r}-\mathbf{R_n})$, with R_n the lattice sites, while for the liquid phase, the charge density $\rho_{\rm liq}(\mathbf{r})$ vanishes beyond a few molecular layer close to the wall. The calculation of this energy is a very challenging task, because both the one-body interaction of ions with their image charges, and the two-body interactions between ions are strongly modified by the presence of the confining metallic (TF) wall. Here, we develop a simplifying description which captures the main effects of wall metallicity on the surface electrostatic energies, with the objective to rationalize the experimental data. This framework is described in Appendix A.

2.5.3 Effect of metallicity on surface tensions

Overall, we predict that the surface tension excess, of the ionic liquid-metal *versus* the ionic crystal-metal interfaces, is a function of the TF screening parameter $k_{\rm TF}$, taking the form

$$\Delta\gamma = \gamma_{\rm WL} - \gamma_{\rm WC} \approx \Delta\gamma^{\rm ins} + \frac{Q^2\,\Delta\rho}{16\pi\epsilon} \times \mathcal{F}(k_{\rm TF}a) \tag{2.8}$$

where $\Delta\gamma^{\rm ins} = \gamma_{\rm WL}^{\rm ins} - \gamma_{\rm WC}^{\rm ins}$ [J.m^{-2}] is the difference in surface energies at *insulating walls*, $\Delta\rho = \rho_{\rm C} - \rho_{\rm L}$ [m^{-3}] is the density difference between the ionic crystal and ionic liquid

phases ($\Delta\rho > 0$), a [m] is an ionic molecular size (typically given by the ionic crystal lattice constant), $Q = e$ [C] is the elementary ionic charge. The dimensionless function $\mathcal{F}$, whose expression is given in Appendix A, is an increasing function of the TF screening $k_{\rm TF}$; it interpolates between 0 and 1 with a cross-over occuring for $k_{\rm TF}a \sim 1$. As a guideline, it can be well approximated as $\mathcal{F}(x) \approx x/(\nu + x)$ with $\nu \simeq 1.7$. The steps leading to this expression are discussed in details in the Appendix A. Overall, the physical picture underlying Eq. (2.8) is that the electrostatic contribution to the surface energy – in excess to the insulating wall situation – originates merely from the direct interaction of ions close to the surface with their image charge, the latter being modified by the TF screening. Interestingly this approximated approach emerges from exact calculations for the 1D crystal-wall interface, which capture the main ingredients at stake and allows us to calculate analytically the surface energy for any TF screening parameter $k_{\rm TF}$. These calculations validate the simplified estimate of the excess surface energy in terms of image charge interactions for a dense ionic system at the interface with a metallic wall, which is then extended to the liquid-wall interface. As a complementary check of the framework, molecular simulations of a model ionic system at finite temperature confirm the lower energy of the crystal-wall interface as compared to the liquid-wall interface in the case of insulating confining substrate, as well as the order of magnitude of the various contributions to the surface energies (see Appendix A.5).

2.5.4 Effect of metallicity on the freezing transition

Altogether we obtain $\Delta\gamma = \Delta\gamma^0\,(1 + \delta \cdot \mathcal{F}(k_{\rm TF}a))$, where $\Delta\gamma^0$ [J/m^2] is the surface tension difference between of the liquid-wall versus crystal-wall interfaces for an insulating substrate and including also the non-electrostatic contributions to the surface energy (van der Waals, ...) and the possible (constant) contribution from the tungsten tip. The dimensionless parameter $\delta = e^2(\rho_{\rm C} - \rho_{\rm L})/(16\pi\epsilon\Delta\gamma_0)$ quantifies the contribution of metallicity to the surface energies.

Now using the Gibbs-Thomson result, Eq. 2.5, one predicts that the increase in surface energy difference for better metals, i.e. for larger Thomas-Fermi wavevector $k_{\rm TF}$ (Eq. 2.8) will lead to a shift in the critical confinement distance for the freezing transition according to

$$\lambda_{\rm S} = \lambda_{\rm S}^0(1 + \delta \cdot \mathcal{F}(k_{\rm TF}a)). \tag{2.9}$$

with $\lambda_{\rm S}^0$ the value for the perfectly insulating material defined in terms of $\Delta\gamma_0$ (here Mica).

2.5.5 Comparison with the experimental data

In Fig. 2.10, we compare the prediction for $\lambda_{\rm S}$ with the experimental data for the various substrates investigated. Note that in doing this comparison, we estimated the values of Thomas-Fermi length based on the substrate conductivity and carrier density (Section 2.2.3). We also fixed the molecular length to the crystal lattice constant as $2a = 0.67$ nm (as estimated from the molar volume of the ionic liquid). As shown in Fig. 2.10, a good agreement between the theoretical predictions and the experimental results is obtained, yielding $\lambda_{\rm S}^0 = 15$ nm and $\delta = 10.1$. From the value for λ_0 and Eq. 2.5, one gets $\Delta\gamma_0 \approx 0.2$ J/m^2. Using Eq. 2.9, and assuming $\rho_{\rm L}/\rho_{\rm C} \sim 0.8$ as typical from such systems [15], this would predict a value of $\delta \approx 10^0$, in fair agreement with the one obtained from the fit of the experimental data, $\delta \approx 10$.

2.6 Effect of tension and bulk melting temperature

2.6.1 Effect of tension

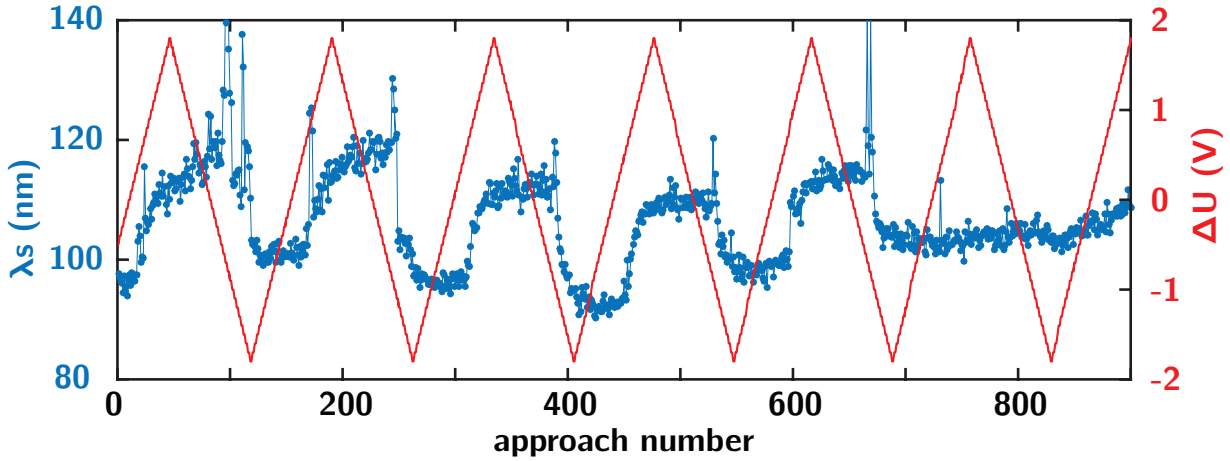

Figure 2.11: Successive measurements of the solidification length λ_S (blue points) when varying the bias voltage ΔU (red points) between the tungsten tip and a HOPG substrate. Each point corresponds to one approach and retract (indicated by approach number, lower axis).

Finally, we might also expect the bias voltage ΔU [V] applied between the two confining surfaces to affect the observed freezing transition. As shown in Figure 2.11, we sweep the applied voltage ΔU between -1.8 V and +1.8 V (red curve), while simultaneously measuring the critical confinement distance λ_S (blue points) for each bias voltage between the tungsten tip and a HOPG substrate. We observe hysteresis cycles in the critical confinement length, with a peak to peak amplitude of approximately 20 nm. Note that such hysteretic effects of the tension are not observed systematically (see for example the last bias cycle for which no effect on critical confinement length is observed). This is not surprising, considering the fact that hysteresis evidence the presence of metastable effects in the freezing transition.

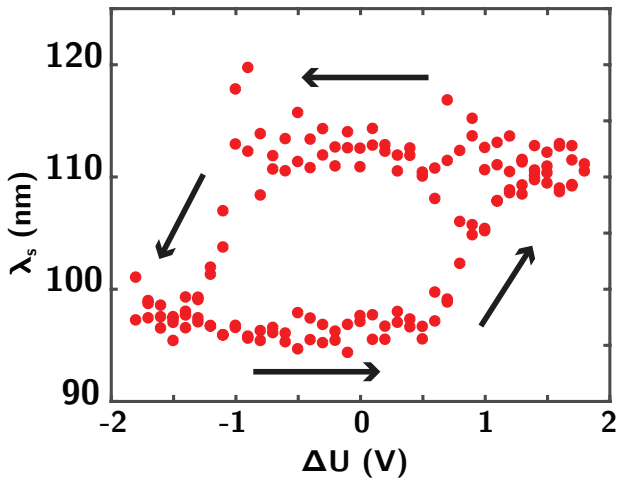

Figure 2.12: Hysteresis cycle for one of the bias cycle shown in Fig. 2.11

In Fig. 2.12, we show the critical confinement length as a function of bias for one hysteresis cycle. The critical onset tension for the hysteretic effect is of the order of ± 1 V.

Following Eq. 2.5, we can interpret the dependence of critical confinement length λ_S on bias voltage ΔU by considering the additional contributions to surface energies due to the charged capacitance at the substrate/ionic liquid interface as:

$$\Delta\gamma = \tilde{\Delta}\gamma + \frac{1}{2}C \cdot \Delta U^2 \tag{2.10}$$

where the last term is the area energy density stored in the capacitor, with C the interfacial capacitance per surface area, and $\tilde{\Delta}\gamma$ takes into account all of the other electronic and non-electronic contributions to surface energies. Considering a typical capacitance of the order of 0.1 F.m^{-2} [1], we obtain an additional surface energy of 0.2 J.m^{-2}, leading to a predicted cycle amplitude of 15 nm, in very good agreement with our experimental results. Those results suggest voltage induced controls of ionic liquid materials, as experienced in previous experiments [35, 53] and theoretical work [19, 20, 46]. Furthermore, the dependence of the critical solidification length on an external control parameter such as the bias voltage is fully consistent with a capillary freezing mechanism implying bulk phase change between the confining tip and the substrate.

2.6.2 Effect of bulk melting temperature

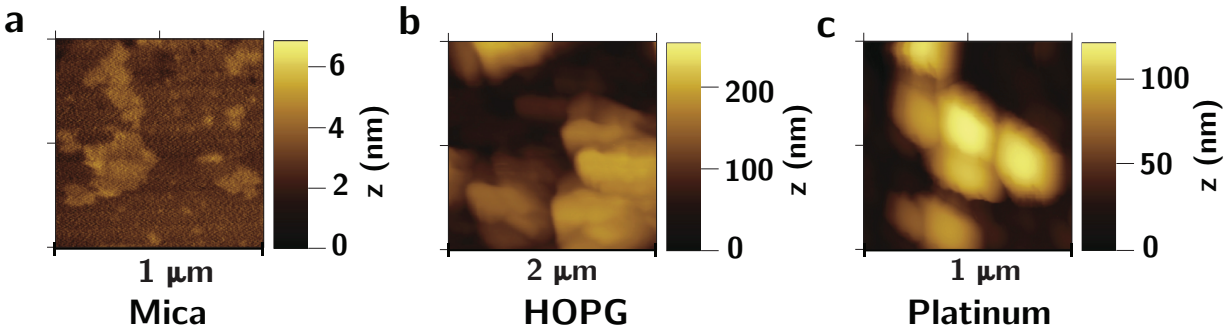

Figure 2.13: AFM images of the surface of the various substrates immersed in BmimPF6.

In the framework of a confinement-induced freezing transition, due to an increase of the melting temperature under confinement, one expect the external temperature and the bulk freezing temperature of the ionic liquid to have an effect on the observed transition. To test these dependence, we performed additional experiments on [Bmim][PF6], a second ionic liquid with a much larger bulk freezing point of $T_B^{PF6} = 7°$ C (Table 2.2), compared to $T_B^{BF4} = -71°$ for BmimBF4 (Table 2.1)

Fig. 2.13 reports experiments consisting of AFM scans of the various surfaces immersed in [Bmim][PF6] using a sharp AFM tip with less than 50 nm end radius. As discussed in Section 2.3.3, this allows us to image the prewetting structures (if any) on the substrates. These experimental scans for [Bmim][PF6] with a small tungsten tip show the presence of very large prewetting layers on the metallic substrates HOPG and Platinum as compared to the Mica substrate. Importantly, we observe an increase in the height of these prewetting layers for [Bmim][PF6], as compared to the prewetting layers on [Bmim][BF4] (see Fig. 2.9). These observations confirm, at least qualitatively, the effect of the ionic liquid bulk melting temperature on its structuration (prewetting) at interfaces.

2.7 Conclusion

In this Chapter, we used nanorheological measurements to explore the properties of ionic liquids in nanometric confinement.

1. **Confining the ionic liquid between tungsten tips of few μm radius and substrates of various nature, we unveil a dramatic change of the ionic liquid towards a solid-like phase below a threshold confinement of the order of tens of nanometers, pointing to a capillary freezing transition in confinement.**

2. **Varying the nature of the substrates from Mica, HOPG, Doped Silicon and Platinum, we find this threshold confinement to be related to the metallicity of the confining materials, with more conductive substrates facilitating freezing.**

3. **We evidence a dependence of this threshold thickness on the bias voltage between the tip and the substrates, leading to well-defined hysteresis cycles. This dependence validates the interpretation of the observed transition as of a *bulk* freezing transition, potentially facilitated by the presence of prewetting solid-like layers.**

4. **We interpret the observed freezing transition by a Gibbs-Thompson effect favoring the solid crystalline phase in confinement. We rationalize the observed dependence of the freezing transition on substrate metallicity by taking into account the influence of the electronic screening (described by a simple Thomas-Fermi approach) on ionic liquid wetting of the confining surfaces.**

Bibliography

1. Alam, M. T., Islam, M. M., Okajima, T. & Ohsaka, T. Capacitance measurements in a series of room-temperature ionic liquids at glassy carbon and gold electrode interfaces. *Journal of Physical Chemistry C* **112,** 16600–16608 (2008).

2. Alba-Simionesco, C. *et al.* Effects of confinement on freezing and melting. *Journal of physics. Condensed matter : an Institute of Physics journal* **18,** R15–R68 (2006).

3. Anaredy, R. S. & Shaw, S. K. Long-Range Ordering of Ionic Liquid Fluid Films. *Langmuir* **32,** 5147–5154 (2016).

4. Anson, F. & Lingane, J. Chemical evidence for oxide films on platinum electrometric electrodes. *Journal of the American Chemical Society* **1315,** 4901–4904 (1957).

5. Armand, M., Endres, F., MacFarlane, D. R., Ohno, H. & Scrosati, B. Ionic-liquid materials for the electrochemical challenges of the future. *Nature Materials* **8,** 621–629 (2009).

6. Atkin, R. *et al.* AFM and STM Studies on the Surface Interaction of [BMP]TFSA and (EMIm]TFSA Ionic Liquids with Au(111). *Journal of Physical Chemistry C* **113,** 13266–13272 (2009).

7. Banerjee, S., Sardar, M., Gayathri, N., Tyagi, A. K. & Raj, B. Conductivity landscape of highly oriented pyrolytic graphite surfaces containing ribbons and edges. *Physical Review B - Condensed Matter and Materials Physics* **72,** 1–7 (2005).

8. Bhatt, V. D., Gohi, K. & Mishra, A. Thermal energy storage capacity of some phase changing materials and ionic liquids. *International Journal of ChemTech Research* **2,** 1771–1779 (2010).

9. Bocquet, L. & Charlaix, E. Nanofluidics, from bulk to interfaces. *Chemical Society Reviews* **39,** 1073–1095 (2010).

10. Bou-Malham, I. & Bureau, L. Nanoconfined ionic liquids: effect of surface charges on flow and molecular layering. *Soft Matter* **6,** 4062 (2010).

11. Bovio, S., Podestà, A., Milani, P., Ballone, P. & Del Pópolo, M. G. Nanometric ionic-liquid films on silica: a joint experimental and computational study. *Journal of physics. Condensed matter : an Institute of Physics journal* **21,** 424118 (2009).

12. Bovio, S., Podestà, A., Lenardi, C. & Milani, P. Evidence of extended solidlike layering in [Bmim][NTf2] ionic liquid thin films at room-temperature. *Journal of Physical Chemistry B* **113,** 6600–6603 (2009).

13. Buchner, F., Forster-Tonigold, K., Bozorgchenani, M., Gross, A. & Behm, R. J. Interaction of a Self-Assembled Ionic Liquid Layer with Graphite(0001): A Combined Experimental and Theoretical Study. *The Journal of Physical Chemistry Letters* **7,** 226–233 (2016).

14. Capozza, R., Vanossi, A., Benassi, A. & Tosatti, E. Squeezout phenomena and boundary layer formation of a model ionic liquid under confinement and charging. *The Journal of Chemical Physics* **142,** 064707 (2015).

15. Dibrov, S. M. & Kochi, J. K. Crystallographic view of fluidic structures for room-temperature ionic liquids: 1-butyl-3-methylimidazolium hexafluorophosphate. *Acta Crystallographica Section C: Crystal Structure Communications* **62,** 19–21 (2006).

16. Dold, C., Amann, T. & Kailer, A. Influence of electric potentials on friction of sliding contacts lubricated by an ionic liquid. *Phys. Chem. Chem. Phys.* **17,** 10339–10342 (2015).

17. Elbourne, A. *et al.* Nanostructure of the Ionic Liquid-Graphite Stern Layer. *ACS Nano* **9,** 7608–7620 (2015).

18. Endres, F., Borisenko, N., El Abedin, S. Z., Hayes, R. & Atkin, R. The interface ionic liquid(s)/electrode(s): In situ STM and AFM measurements. *Faraday Discussions* **154,** 221 (2012).

19. Fajardo, O. Y., Bresme, F., Kornyshev, A. A. & Urbakh, M. Electrotunable Lubricity with Ionic Liquid Nanoscale Films. *Scientific Reports* **5,** 7698 (2015).

20. Fajardo, O. Y., Bresme, F., Kornyshev, A. A. & Urbakh, M. Electrotunable Friction with Ionic Liquid Lubricants: How Important Is the Molecular Structure of the Ions? *Journal of Physical Chemistry Letters* **6,** 3998–4004 (2015).

21. Fedorov, M. V. & Kornyshev, A. A. Ionic liquids at electrified interfaces. *Chemical Reviews* **114,** 2978–3036 (2014).

22. Galiński, M., Lewandowski, A. & Stepniak, I. Ionic liquids as electrolytes. *Electrochimica Acta* **51,** 5567–5580 (2006).

23. Gebbie, M. A. *et al.* Ionic liquids behave as dilute electrolyte solutions. *Proceedings of the National Academy of Sciences* **110,** 9674–9679 (2013).

24. Gebbie, M. a., Dobbs, H. a., Valtiner, M. & Israelachvili, J. N. Long-range electrostatic screening in ionic liquids. *Proceedings of the National Academy of Sciences* **112,** 201508366 (2015).

25. Gebbie, M. A. *et al.* Long range electrostatic forces in ionic liquids. *Chem. Commun.* **53,** 1214–1224 (2017).

26. Hayes, R., Warr, G. G. & Atkin, R. At the interface: solvation and designing ionic liquids. *Physical Chemistry Chemical Physics* **12,** 1709 (2010).

27. Hayes, R., Warr, G. G. & Atkin, R. Structure and Nanostructure in Ionic Liquids. *Chemical Reviews* **115,** 6357–6426 (2015).

28. Horn, R. G., Evans, D. F. & Ninham, B. W. Double-layer and solvation forces measured in a molten salt and its mixtures with water. *Journal of Physical Chemistry* **92,** 3531–3537 (1988).

29. Hoth, J., Hausen, F., Müser, M. H. & Bennewitz, R. Force microscopy of layering and friction in an ionic liquid. *Journal of physics. Condensed matter : an Institute of Physics journal* **26,** 284110 (2014).

30. Jurado, L. A. *et al.* Irreversible structural change of a dry ionic liquid under nanoconfinement. *Phys. Chem. Chem. Phys.* **17,** 13613–13624 (2015).

31. Jurado, L. A. *et al.* Effect of the environmental humidity on the bulk, interfacial and nanoconfined properties of an ionic liquid. *Physical Chemistry Chemical Physics* **18,** 22719–22730 (2016).

32. Lee, A. A. & Perkin, S. Ion-Image Interactions and Phase Transition at Electrolyte-Metal Interfaces. *Journal of Physical Chemistry Letters* **7,** 2753–2757 (2016).

33. Leroy, S. & Charlaix, E. Hydrodynamic interactions for the measurement of thin film elastic properties. *Journal of Fluid Mechanics* **674,** 389–407 (2011).

34. Lhermerout, R., Diederichs, C. & Perkin, S. Are Ionic Liquids Good Boundary Lubricants? A Molecular Perspective. *Lubricants* **6,** 9 (2018).

35. Li, H., Wood, R. J., Rutland, M. W. & Atkin, R. An ionic liquid lubricant enables superlubricity to be "switched on" in situ using an electrical potential. *Chemical Communications* **50,** 4368 (2014).

36. MacFarlane, D. R. *et al.* Energy applications of ionic liquids. *Energy Environ. Sci.* **7,** 232–250 (2014).

37. Mahan, G. D. in (Springer Science & Business Media, 2013).

38. Merlet, C., Rotenberg, B., Madden, P. a. & Salanne, M. Computer simulations of ionic liquids at electrochemical interfaces. *Physical chemistry chemical physics : PCCP* **15,** 15781–92 (2013).

39. Merlet, C. *et al.* On the molecular origin of supercapacitance in nanoporous carbon electrodes. *Nature materials* **11,** 306–310 (2012).

40. Morita, M., Ohmi, T., Hasegawa, E., Kawakami, M. & Ohwada, M. Growth of native oxide on a silicon surface. *Journal of Applied Physics* **68,** 1272–1281 (1990).

41. O'Mahony, A. M., Silvester, D. S., Aldous, L., Hardacre, C. & Compton, R. G. Effect of water on the electrochemical window and potential limits of room-temperature ionic liquids. *Journal of Chemical and Engineering Data* **53,** 2884–2891 (2008).

42. Palacio, M. & Bhushan, B. A review of ionic liquids for green molecular lubrication in nanotechnology. *Tribology Letters* **40,** 247–268 (2010).

43. Perkin, S. Ionic liquids in confined geometries. *Physical Chemistry Chemical Physics* **14,** 5052 (2012).

44. Perkin, S., Albrecht, T. & Klein, J. Layering and shear properties of an ionic liquid, 1-ethyl-3-methylimidazolium ethylsulfate, confined to nano-films between mica surfaces. *Physical Chemistry Chemical Physics* **12,** 1243–1247 (2010).

45. Pierson, H. O. Graphite Structure and Properties. *Handbook of Carbon, Graphite, Diamonds and Fullerenes,* 43–69 (1993).

46. Pivnic, K., Fajardo, O. Y., Bresme, F., Kornyshev, A. A. & Urbakh, M. Mechanisms of Electrotunable Friction in Friction Force Microscopy Experiments with Ionic Liquids. *Journal of Physical Chemistry C* **122,** 5004–5012 (2018).

47. Rotenberg, B. & Salanne, M. Structural Transitions at Ionic Liquids Interfaces. *The Journal of Physical Chemistry Letters* **6,** 4978–4985 (2016).

48. Singh, M. P., Singh, R. K. & Chandra, S. Ionic liquids confined in porous matrices: Physicochemical properties and applications. *Progress in Materials Science* **64,** 73–120 (2014).

49. Smith, A. M., Lee, A. A. & Perkin, S. The Electrostatic Screening Length in Concentrated Electrolytes Increases with Concentration. *Journal of Physical Chemistry Letters* **7,** 2157–2163 (2016).

50. Smith, A. M., Lovelock, K. R. J., Gosvami, N. N., Welton, T. & Perkin, S. Quantized friction across ionic liquid thin films. *Physical Chemistry Chemical Physics* **15,** 15317 (2013).

51. Smith, A. M. *et al.* Monolayer to Bilayer Structural Transition in Confined Pyrrolidinium-Based Ionic Liquids. *The Journal of Physical Chemistry Letters* **4,** 378–382 (2013).

52. Su, Y. Z., Fu, Y. C., Yon, J. W., Chen, Z. B. & Mao, B. W. Double layer of Au(100)/ionic liquid interface and its stability in imidazolium-based ionic liquids. *Angewandte Chemie - International Edition* **48,** 5148–5151 (2009).

53. Sweeney, J. *et al.* Control of Nanoscale Friction on Gold in an Ionic Liquid by a Potential-Dependent Ionic Lubricant Layer. *Physical Review Letters* **109,** 155502 (2012).

54. Sze, S. M. *Semiconductor devices: physics and technology* ISBN: 812651681X (2008).

55. Troncoso, J., Cerdeiriña, C. A., Sanmamed, Y. A., Romaní, L. & Rebelo, L. P. N. Thermodynamic Properties of Imidazolium-Based Ionic Liquids: Densities, Heat Capacities, and Enthalpies of Fusion of [bmim][PF6] and [bmim][NTf2]. *Journal of Chemical & Engineering Data* **51,** 1856–1859 (2006).

56. Ueno, K., Kasuya, M., Watanabe, M., Mizukami, M. & Kurihara, K. Resonance shear measurement of nanoconfined ionic liquids. *Physical Chemistry Chemical Physics* **12,** 4066 (2010).

57. Uesugi, E., Goto, H., Eguchi, R., Fujiwara, A. & Kubozono, Y. Electric double-layer capacitance between an ionic liquid and few-layer graphene. *Scientific reports* **3,** 1595 (2013).

58. Ye, C., Liu, W., Chen, Y. & Yu, L. Room-temperature ionic liquids: a novel versatile lubricant. *Chemical communications (Cambridge, England),* 2244–2245 (2001).

59. Yokota, Y., Harada, T. & Fukui, K.-i. Direct observation of layered structures at ionic liquid/solid interfaces by using frequency-modulation atomic force microscopy. *Chemical communications (Cambridge, England)* **46,** 8627–8629 (2010).

60. Zhou, F., Liang, Y. & Liu, W. Ionic liquid lubricants: designed chemistry for engineering applications. *Chemical Society Reviews* **38,** 2590 (2009).

Chapter 3

Molecular Rheology of Atomic Gold Junctions

Contents

Despite extensive documentation of plastic deformation processes in micro and nano sized metallic samples, very little is known on the plastic mechanisms at play in systems of molecular size. In this Chapter, we probe plasticity at the individual atomic level by measuring the viscoelastic rheological response of gold junctions of few atoms radius, submitted to picometric oscillations. Shearing the bridge with increasing amplitude, we uncover a dramatic transition from a purely elastic regime to a plastic flow regime, up to the complete shear-induced melting of the bridge. Varying the lateral junction size through the conductance of the system, we study the dependence of those distinct rheological regimes on junction geometry. In those molecular objects, plastic flow seems to be limited by the sliding of atomic planes under shear, as predicted for dislocation free systems, while the dissipative plastic regime is well-described by a viscous-like frictional force, distinct from traditional models of plastic flow.

3.1 General Context

Solid metallic materials in the micron range and below have been show to exhibit drastically different mechanical behaviors than their macroscopic counterparts. Such size-effects [17, 20] take their origin in the decreasing density of defect-mediated plastic events, such as ocuring during dislocation gliding [26, 31, 36] or twinning [7, 22, 38], and the increasing surface to volume ratio [41]. Extending those measurements to the 100-10 nm scale and below has been a difficult and challenging task, leading to apparently contradicting measurement reporting both very large yield stress [6, 32, 36] and liquid-like apparent behaviors [21, 34]. The understanding of plastic flow in systems of molecular or atomic sizes, has thus so far remained incomplete, despite its fundamental interest and broad applications ranging from the understanding of shape stability in nanoelectronics [23, 34], fundamental dissipation channels in nanomechanical resonators [18], as well as understanding the role played by nanocontacts in macroscopic friction and adhesion [25, 28, 30].

In this Chapter, we probe plasticity at the individual atom level, in junctions of few gold atoms. Such systems have been extensively studied for their electronic properties in the past two decades [2, 27, 29, 37], their molecular dimensions leading to quantized electrical conductance, and allowing a direct readout of transverse dimension of the junction at the single atom level. Several mechanical measurements on metallic junctions have reported that nanowire elongation is caused by successive elastic and yielding events, concomitant with changes in the electrical conductance [1, 3, 24, 32, 33, 35]. We employ here a distinct strategy by submitting the gold junction to increasing shear to probe it viscoelastic flow properties.

3.2 Experimental set-up

3.2.1 Experimental set-up

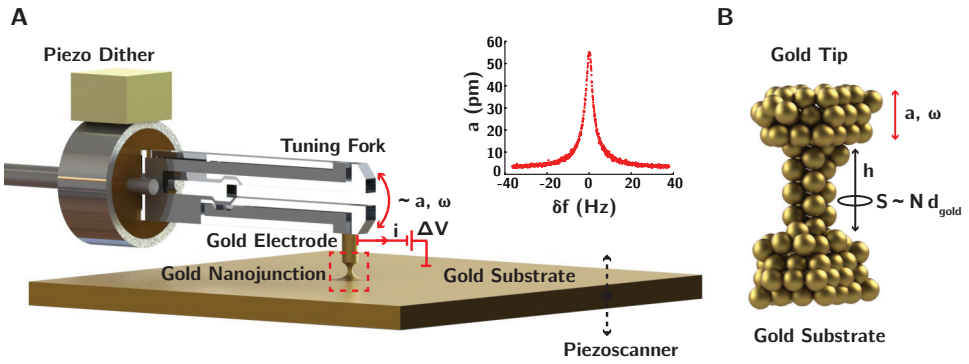

Figure 3.1: **Experimental Set-Up** (**A**) Schematic of the experimental set-up. A gold junction (red dashed box) is formed between a gold electrode, attached to the tuning fork and the gold substrate. Inset: resonance curve of the free tuning fork in air, with ≈ 60 pm maximal amplitude. (**B**) Schematic representation of the idealized junction geometry. The junction is assumed to have a rod-like shape with height h and surface area $S \sim N d_{\text{gold}}^2/4$. The junction is sheared vertically with oscillation amplitude a and frequency ω.

Figure 3.1A shows a schematic of the set-up. A gold tip is glued on one prong of the quartz-tuning fork Atomic Force Microscope.

During a typical experiment, we first gently indent the gold tip on a gold-coated surface, creating a metallic junction of gold atoms between the tuning fork and the substrate. Increasing the separation between the electrode and the substrate leads to thinning and necking of the junction, which can be tuned to reach molecular size of a few atoms width, as schematically represented in Fig. 3.1B.

The gold tip is obtained by cutting a wire of 200 µm diameter (Goodfellow 99.99 % purity) with a wire cutter. Gold substrates were obtained by evaporating a layer of 5 nm Cromium and 150 nm gold on Si/SiO_2 substrates. Most experiments presented in this Chapter were performed at room temperature, in a box initially filled with nitrogen and desiccants, to keep humidity level below 5 % RH. Note that some impedance spectroscopy measurements, presented in Section 3.6.3 were performed in a vacuum chamber at 10^{-6} mbar of pressure.

In all experiments, the gold substrate is biased with respect to the gold tip, with a 13 mV bias. The corresponding current flowing through the junction (of the order of several µA) and junction conductance G [S] is measured with a current/voltage amplifier.

3.2.2 Static mechanical properties of the junction

Quantized electrical transport

Increasing the distance between the electrode and the substrate, the junction thins down and we observe, as shown in Fig. 3.2A, a step-wise variation in the conductance G of the junction, which varies approximately in multiples of $G_0 = 2e^2/h \approx 77$ μS. Quantization of the conductance occurs because the lateral size of the junction is smaller than the mean free path for electrons in gold ($\lambda_{\text{mfp}}^{\text{gold}} \approx 40$ nm), leading to ballistic electronic transport [3].

In a good approximation, the conductance G is simply proportional to the number $\mathcal{N}$ of conductance channels, i.e. to the number of atoms in the cross-section, with:

$$G \approx \mathcal{N} \cdot G_0 \tag{3.1}$$

Fig. 3.2A shows the conductance trace of the junction upon elongation. The junction thins down from $\mathcal{N} = 9$, down to $\mathcal{N} = 1$ atom.

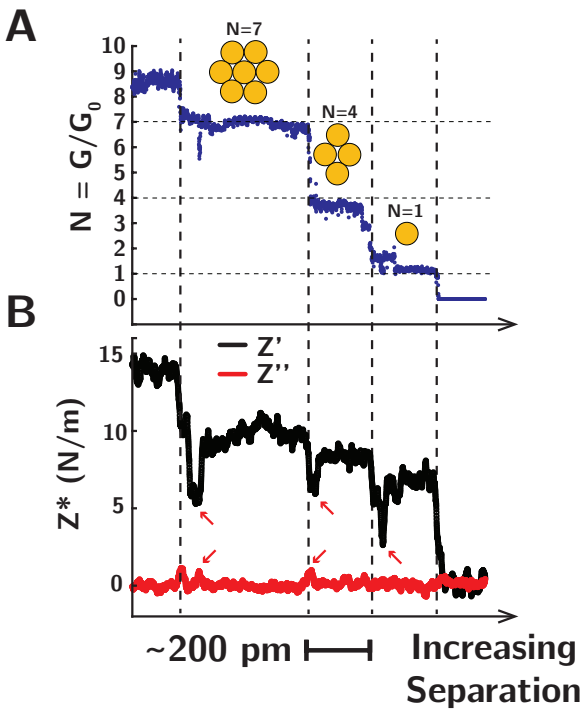

Figure 3.2: **Static mechanical properties of the junction** (**A**) Typical dimensionless conductance trace for increasing separation between the two surfaces. Conductance varies stepwise, in multiples of G_0. (**B**) Simultaneous measurement of the conservative (Z', black) and dissipative (Z", red) part of the mechanical impedance Z^* of the gold junction.

Mechanical properties of the gold junction upon elongation

To probe the mechanical response of the gold junction, we further excite the tuning fork via the piezodither. We show in Fig. 3.2B, the variations of Z' and Z'' measured with an oscillation amplitude $a_0 = 70$ pm, along with the variation of junction conductance (Fig. 3.2A). On each plateau in conductance, the stiffness Z' is approximately constant, indicating a constant organization of the junction and the dissipative modulus Z'' is null, indicating the absence of intrinsic dissipation in the structure. Those results are in agreement with previous experiments on platinum chains [33] and show a clear correlation between the mechanical properties of the junction, and the current trace.

At each change in conductance, we observe a transient loss of stiffness Z' and a slight transient increase in dissipation Z'' (red arrows, Fig. 3.2B), which may indicate plastic reorganization of the junction upon each change in atomic configuration.

3.3 Rheology of a gold nanojunction

3.3.1 Viscoelastic junction properties

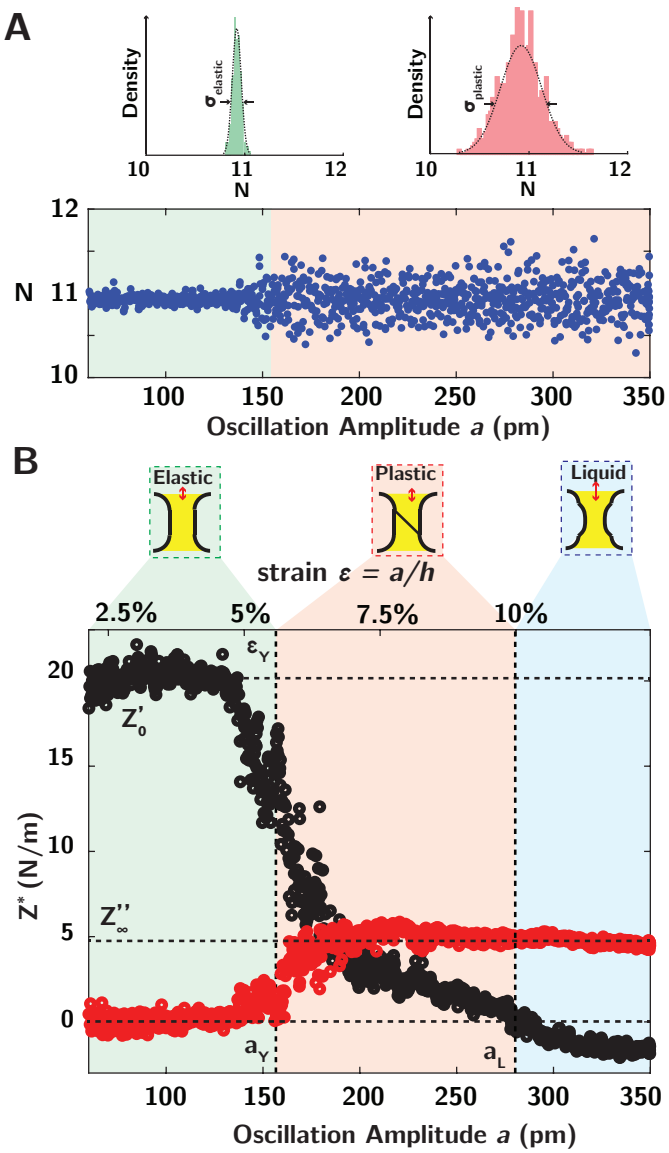

Figure 3.3: **Rheology of the gold nanojunction (A)** Dimensionless conductance trace $N = G/G_0$ as a function of the oscillation amplitude of the tuning fork for sampling rate of 50 Hz. At the transition between the elastic and plastic regime of deformation, the current noise increases, while retaining a fixed mean value. Histograms show conductance distribution for the elastic (green) and plastic (red) regimes. **(B)** Measurement of the viscoelastic properties of the junction with a fixed cross-sectional area. Variation of storage (Z', black) and loss (Z'', red) impedance of the junction as a function of oscillation amplitude a of the tuning fork. With increasing oscillation amplitude, we observe a successive transition from elastic (green, constant Z', $Z'' = 0$) to plastic (red, decrease in Z', increase in Z'') up to a liquid-like regime showing capillary adhesion (blue, $Z' < 0$).

Characterization for a fixed cross-sectional area

To go further in the characterization of the static and dynamic properties of the junction, we probe the viscoelastic flow properties of the junction under shear. We maintain a fixed cross-sectional area by imposing a constant junction conductance G (corresponding to a fixed number $<\mathcal{N}>$ of atoms) and submit the junction to increasing solicitation amplitude a, which can range from 20 pm up to 1 nm. The cross-sectional area is imposed by adjusting the distance between the gold electrode attached to the tuning fork and the gold surface in order to compensate for thermal drift and maintain a fixed mean current through the junction (see Fig. 3.3A for current trace).

We show in Fig. 3.3B the simultaneous measurement of the elastic ($Z' = \mathrm{Re}(Z^*)$, black) and dissipative ($Z'' = \mathrm{Im}(Z^*)$, red) part of the mechanical impedance Z^* [N.m^{-1}] of the junction, as a function of the oscillation amplitude a of the tuning fork (lower axis) and the strain of deformation $\epsilon = a/h$ (upper axis, see below for estimation of height), for a mean contact number $\mathcal{N} = 11$.

Elastic regime

At low oscillation amplitude, corresponding to weak solicitation of the junction, we observe a purely elastic response of the gold junction, characterized by the absence of dissipation in the junction ($Z'' = 0$) and a finite constant positive stiffness $Z'_0 > 0$ (Fig. 3.3A, green). This regime corresponds to the one of Fig. 3.2B, where the oscillation amplitude is small enough to keep the gold junction unperturbed. In this regime, current fluctuations are small (Fig. 3.3B, green histogram with spectral power density $S_{\mathcal{N}} = 0.01$ Hz$^{-1/2}$).

The constant positive elastic stiffness Z'_0 in this elastic regime allows for a coarse characterization of junction geometry. Following [3], we model the junction as a short cylinder of area $\mathcal{A} = \mathcal{N}\pi d_{\mathrm{gold}}^2/4$ with $\mathcal{N}$ the atomic contact number, $d_0 = 0.288$ pm the gold atomic diameter and h [m] an equivalent cylinder height (see Fig. 3.1B). The relation between the equivalent junction height h and the junction stiffness Z'_0 at low oscillation amplitude can be simply expressed as:

$$Z'_0 = \frac{E_{\mathrm{gold}}\mathcal{A}}{h} \tag{3.2}$$

where we take $E_{\mathrm{gold}} = 79$ GPa the bulk gold young modulus. One should highlight that the estimate of junction height then depends on the choice of the value of this young modulus.

Estimating the junction height h from the elastic impedance Z'_0 at low oscillation amplitude, we can characterize the plastic behavior of the junction as a function of the dimensionless strain $\epsilon = a/h$ (Fig. 3.3B, upper axis).

Plastic regime

Increasing the oscillation amplitude a or strain $\epsilon = a/h$, we evidence in Fig. 3.3B a decrease in stiffness Z' and an increase in dissipation Z'' (red zone). We characterize the entry into this plastic regime of deformation by a critical oscillation amplitude a_{Y} corresponding to the decrease of Z' and increase of Z'' to half of their asymptotic values ($Z'(a_Y) \approx Z'_0/2$ and $Z''(a_Y) \approx Z''_\infty/2$).

The entry into this plastic regime is well characterized by a yield force F_{Y} measured as:

$$F_{\mathrm{Y}} = Z'_0 \cdot a_Y \tag{3.3}$$

This yield force only depends on raw experimentally measured quantities. Additionally, entry in this plastic regime can be characterized by the critical yield strain $\epsilon_{\mathrm{Y}} = a_{\mathrm{Y}}/h$ (Fig. 3.3B, upper axis).

In this second plastic regime, irreversible changes occur due to the shearing action of the tuning fork, leading to plastic flow in the junction, and an increase in dissipation. Reorganization in the junction is further evidenced by the increase in current fluctuations (Fig. 3.3A, red histogram with spectral power density $S_{\mathcal{N}} = 0.04$ Hz$^{-1/2}$).

At large oscillation amplitude, in the plastic regime, the dissipative modulus plateaus, pointing to a regime of hydrodynamic-like friction, with $F_{\mathrm{D}} \sim a$, corresponding to $Z''_{\infty} \sim F_{\mathrm{D}}/a \sim$ cst, while the junction stiffness decreases steadily.

Liquid-like regime

Finally, increasing the oscillation amplitude even further, we observe a third regime characterized by the appearance of a negative stiffness at a critical oscillation amplitude a_{L} (Fig. 3.3A, $Z' < 0$ for $a > a_{\mathrm{L}} = 280$ pm) corresponding to an attractive adhesive response of the junction. Such adhesive effects are reminiscent of capillary adhesion [9], and may express the liquid-like behavior of the junction at large oscillation amplitudes, whose mechanical response becomes dominated by surface tension effects (See Section 3.5.2)

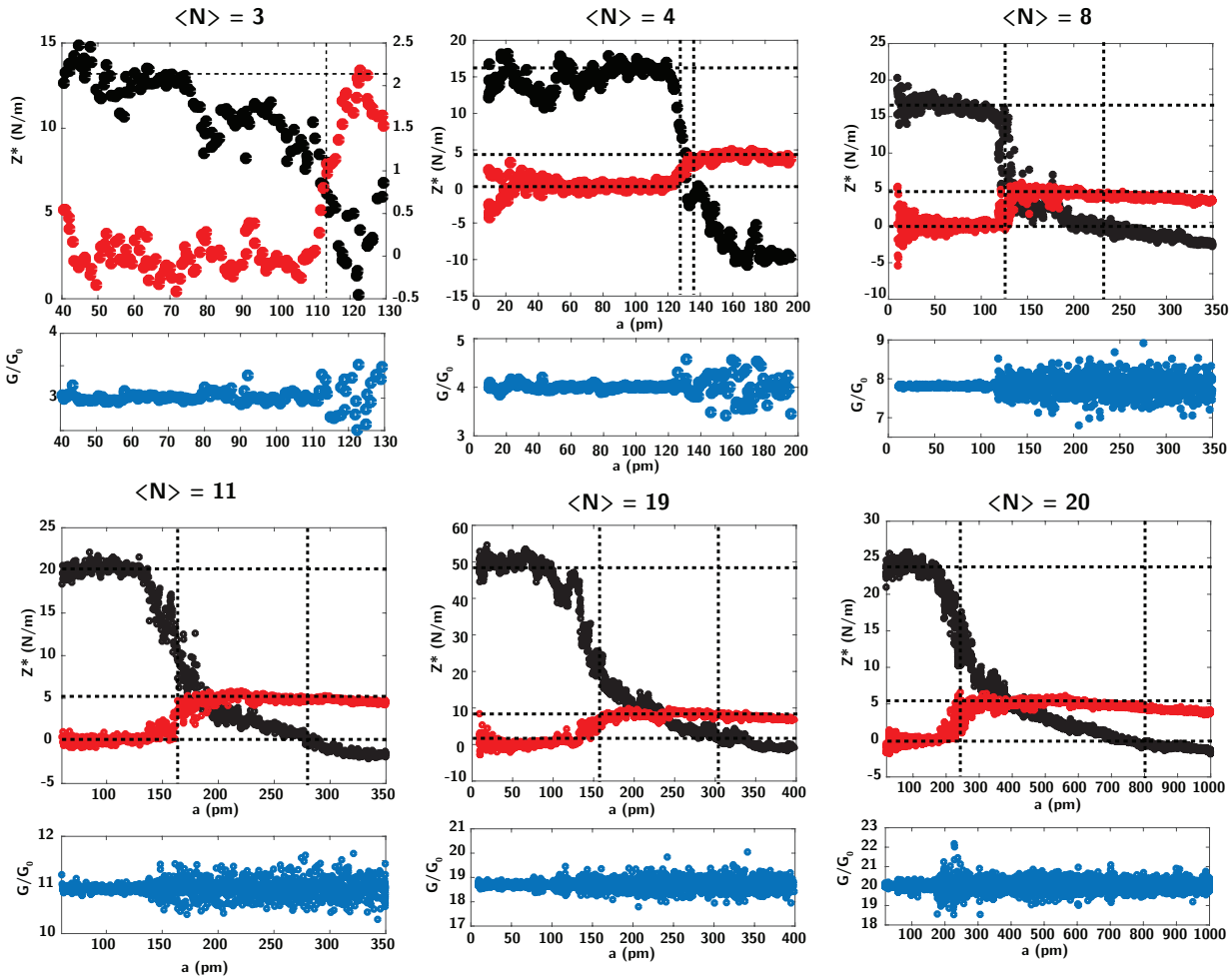

Figure 3.4: **Typical Rheological Curves.** Typical rheological curves for various contact conductance, showing conservative modulus Z' (black), dissipative modulus Z'' (red) and mean current $N = G/G_0$ (blue).

3.3.2 Typical rheological curves and reversibility

We show in Fig. 3.4 additional examples of rheological curves for various contact conductance. The general trends of the rheological curves are maintained, with (1) a plastic transition at a critical oscillation amplitude a_{Y}, corresponding to a decrease in Z' and an increase in Z'', and an increase in current fluctuations, (2) a plateau in the dissipative impedance at large oscillation amplitude, (3) a decrease of the conservative impedance to negative values $Z' < 0$, corresponding to a capillary-like attraction at a critical oscillation amplitude a_{L}.

Additionally, we show in Fig. 3.5 an example of a rheological curve obtained for increasing and decreasing oscillation amplitude. The plastic transition is found to be reversible, with here no visible hysteresis.

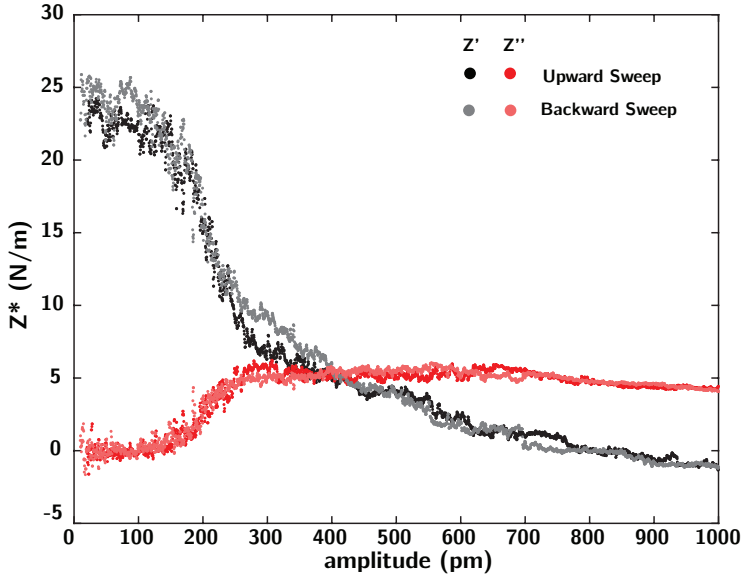

Figure 3.5: Rheological curve obtained for increasing (dots) and decreasing (cross) amplitude of oscillation. The plastic transition is found to be completely reversible, with here no visible hysteresis.

3.4 Yield stress and yield force for plastic flow

In the following sections, we probe the dependence of the rheological signature on lateral junction size. Using the quantized variation of the junction conductance with lateral number of atoms, we vary the lateral junction size atom by atom, from as low as $\mathcal{N} \approx 3$ atoms, corresponding to an equivalent cross-sectionnal area $\mathcal{A} \approx \mathcal{N}\pi d_{\text{gold}}^2/4 \approx 0.2$ nm^2, and up to $\mathcal{N} = 30$ atoms. We report the behavior of the junction as a function of the mean junction size $<\mathcal{N}>$, taken as the closest integer value of the mean dimensionless conductance number $\mathcal{N} = G/G_0$.

3.4.1 Yield force, yield stress and yield strain

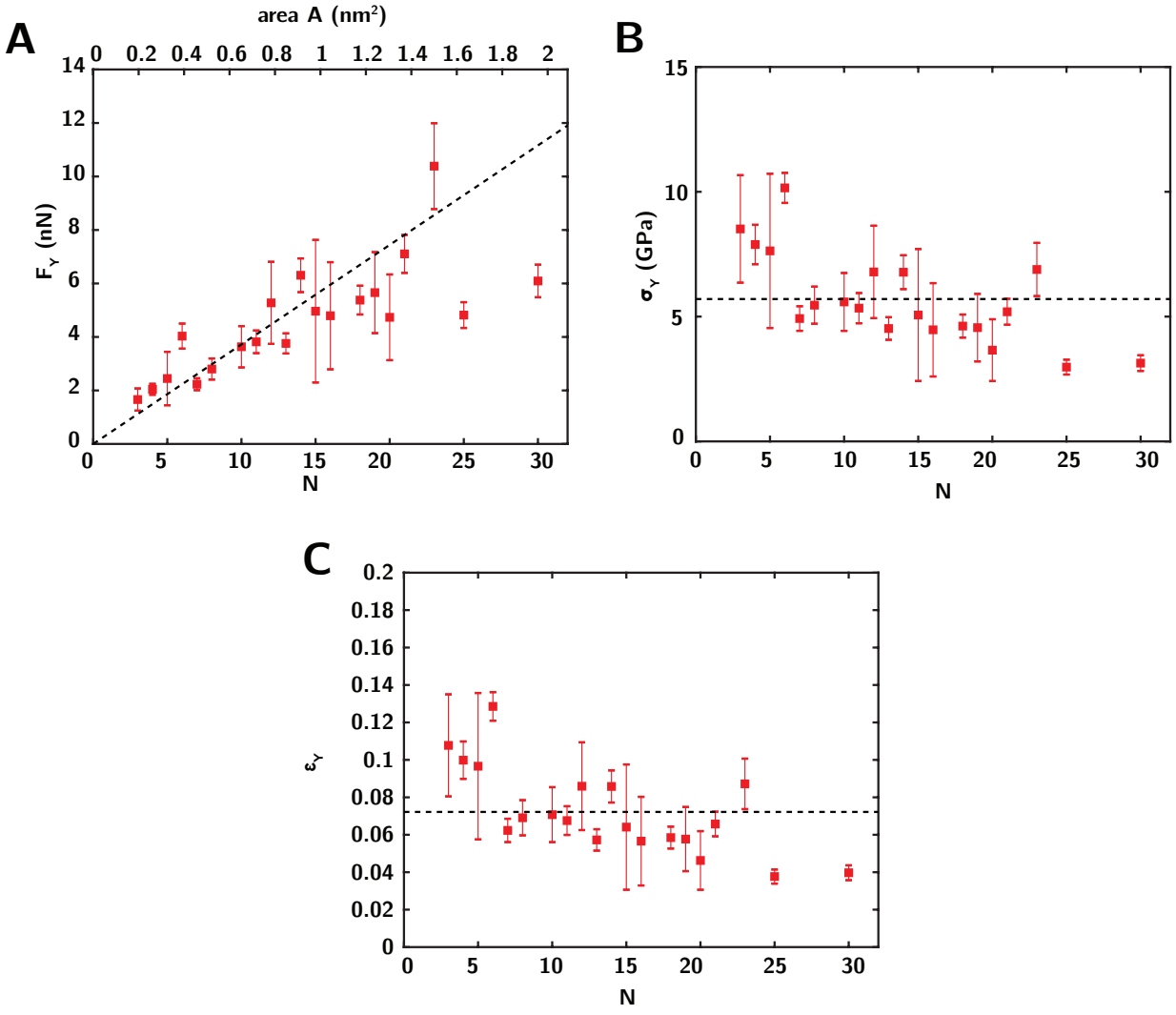

Figure 3.6: **(A)**Yield Force F_{Y}, **(B)** Yield Stress σ_{Y} and **(C)** Yield strain ϵ_{Y} as a function of mean contact number $\mathcal{N}$. Error bars are standard deviation and we take a 10% relative error for single valued point.

Yield force

We report in Fig. 3.6A the yield force $F_Y = Z_0' \cdot a_{\text{Y}}$ corresponding to the force necessary

to drive the junction in the plastic state as a function of the number of atoms in a cross-section (lower axis), or equivalently to the cross-sectional area (upper axis). The yield force F_Y has a fair linear variation with the mean number $\mathcal{N}$ of atoms in a cross-section.

Yield stress

Additionally, we report in Fig. 3.6B the yield stress $\sigma_Y = F_Y/\mathcal{A}$ with $\mathcal{A}$ computed from the contact number $\mathcal{N}$ as $\mathcal{A} = \mathcal{N}\pi d_0^2/4$. The yield stress σ_Y is found to be roughly independent of contact area and of the order of 5 GPa. Importantly, this value is much larger than the yield stress in macroscopic gold samples, which ranges from 55 to 200 MPa [15].

Yield strain

Additionally, we plot in Fig. 3.6C the critical yield strain $\epsilon_Y = a_Y/h$ as a function of the mean number of atoms in the junction. The yield stain ϵ_Y is of the order of 4-12%, a value much larger than the experimental yield strain in macroscopic gold samples (smaller than 1 %), and is found to be roughly independent of the mean number of atoms in a cross-section.

Note that the value of the yield strain is dependent on the value of the bulk gold young modulus $E_{\text{gold}} = 79$ GPa, which we used to estimate junction height h. This critical yield strain follows the same trend as the yield stress σ_Y, as we simply have $\sigma_Y = E_{\text{gold}}\epsilon_Y$.

3.4.2 Interpretation of the deformation mechanism

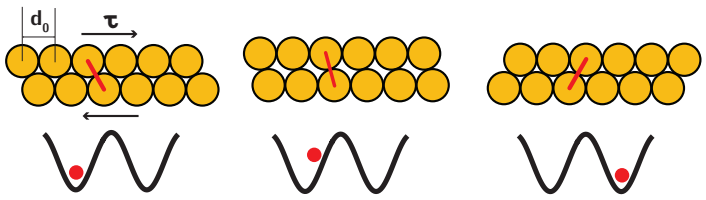

Figure 3.7: Schematic representation of a perfect slip event in the junction, leading to change of equilibrium configuration.

Perfect slip in a crystal

The linear variation of yield force with cross-sectional area $\mathcal{A}$ and number $\mathcal{N}$ of atoms in the chain (Fig. 3.6A) suggests a peculiar deformation mechanisms in the junction, similar to slip in a perfect crystal, for which all the atoms implied in the plastic event would contribute to the yield force (Fig. 3.7). Such defect-free deformation mechanism is reminiscent of T1 events occurring in foams [8].

Importantly, this perfect slip mechanism is distinct from classical plastic deformation mechanism, based on defects such as dislocations, which can move in the crystalline structure at a much lower energy cost, and lead to a decrease of the yield stress compared to its maximal value. Here, such dislocation based mechanisms are probably forbidden due to the molecular size of the sample.

Typical sample size for defect expulsion

We can estimate the typical size below which the sample should be dislocation-free by comparing the stress field $\sigma(r) \sim Gb_0/r$ created by a single dislocation of burger vector b_0 [m] in a material of shear modulus G [Pa] with the yield stress σ_Y [Pa]. As an order of magnitude estimate, we take $G = 27$ GPa and $b_0 = 288$ pm of order of the gold atomic diameter, to find a typical size $r_0 \sim Gb_0/(\sigma_Y) \sim 1.5$ nm, corresponding to a mean contact number $N \approx 25$.

Maximal yield stress

In the case of slip in a perfect crystal, as pictured in Fig. 3.7, one can evaluate the relation between the yield stress σ_Y and the shear modulus G by following Frenkel [3, 16]. We consider two neighboring planes in a crystal with a repeat distance b in the shear direction and spacing h. As a shear stress is applied, if these planes remain undistorted, the shear stress τ will vary with displacement as:

$$\tau = \frac{Gb}{2\pi h} \sin(2\pi x/b) \tag{3.4}$$

with G the shear modulus. The maximal value of τ is then $\tau_{\max} = Gb/(2\pi h)$. For the (111) plane of a fcc metal, we have $b = a/\sqrt{6}$ and $h = a/\sqrt{3}$ with a the lattice parameter. This gives $\tau_{\max} \approx G/9$. Taking the shear modulus $G = 27$ GPa for gold, we find a maximal yield stress ≈ 3 GPa, in good agreement with our measurements.

3.5 Dissipative response in the plastic regime

We now come back to the dissipative behavior of the junction following the yielding transition. Surprisingly, this dissipative response is consistently characterized by a plateau in the dissipative mechanical impedance Z''_∞, indicative of a linear relation between the dissipative force F_D and oscillation amplitude a (see Fig. 3.3 and Fig. 3.4).

3.5.1 Friction coefficient

The proportionality between the friction force F_D and the oscillation amplitude a of the tuning fork (corresponding to a constant mechanical impedance Z''_∞) suggests to express the dissipative response of the junction in terms of a friction coefficient λ [kg.m^{-2}.s^{-1}], relating the dissipative force F_D with the oscillation speed $v = a\omega$ as:

$$F_D = \lambda \cdot A \cdot v \tag{3.5}$$

We show in Fig. 3.8A the variation of $F_D/a = Z''_\infty$ in the dissipative regime with the mean number $\mathcal{N}$ of atoms in a cross-section. We find a fair linear variation of F_D/a with the cross sectional area.

We express the mean friction coefficient $\lambda = F_D/(aA\omega) = Z''_\infty/(A\omega)$ with the cross-sectional number of atoms. This equivalent friction coefficient λ is roughly independent of the cross-sectional area with an increase at low $\mathcal{N}$ and is of order of $5 \cdot 10^{12}$ kg.m^{-2}.s^{-1} (Fig. 3.8B).

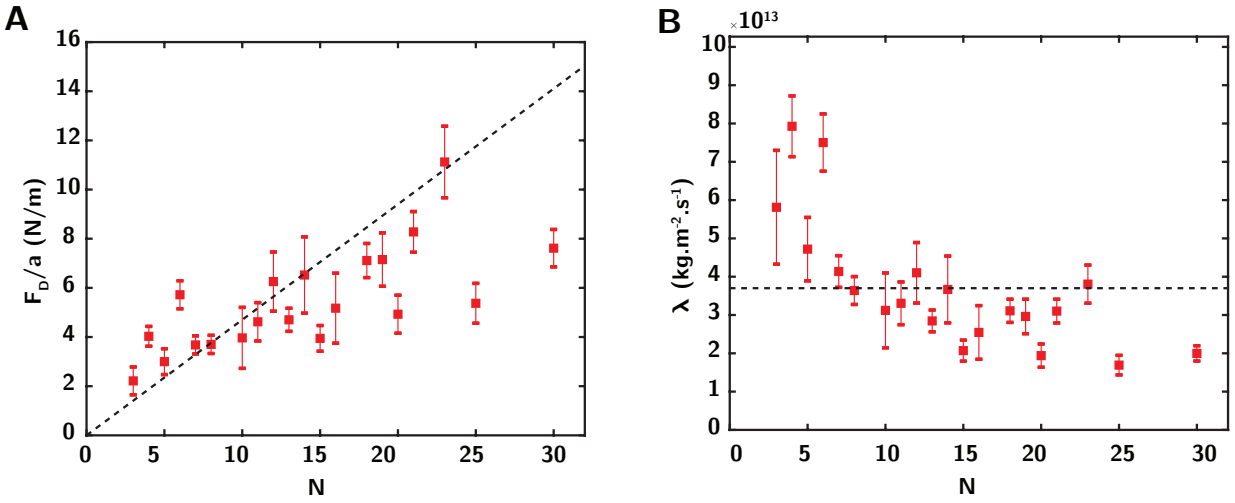

Figure 3.8: (**A**) Hydrodynamic dissipation $F_{\mathrm{D}}/a = Z''_{\infty}$ and (**B**) Friction coefficient λ as a function of the cross-sectional number of atoms $\mathcal{N}$. Error bars are standard deviation and we take a 10% relative error for single valued point.

3.5.2 Liquid-like dissipative response

Actually, the linear variation of dissipation with the oscillation amplitude a could suggest a complete liquid-like behavior of the junction at large oscillation amplitude, with a linear variation of dissipation with the shear rate $\dot{\gamma} = a\omega/h$, and a hydrodynamic force scaling as:

$$F_{\mathrm{D}} = \frac{\eta a \omega \mathcal{A}}{h} = \eta \dot{\gamma} \mathcal{A} \tag{3.6}$$

with $\mathcal{A}$ the contact area and η the viscosity.

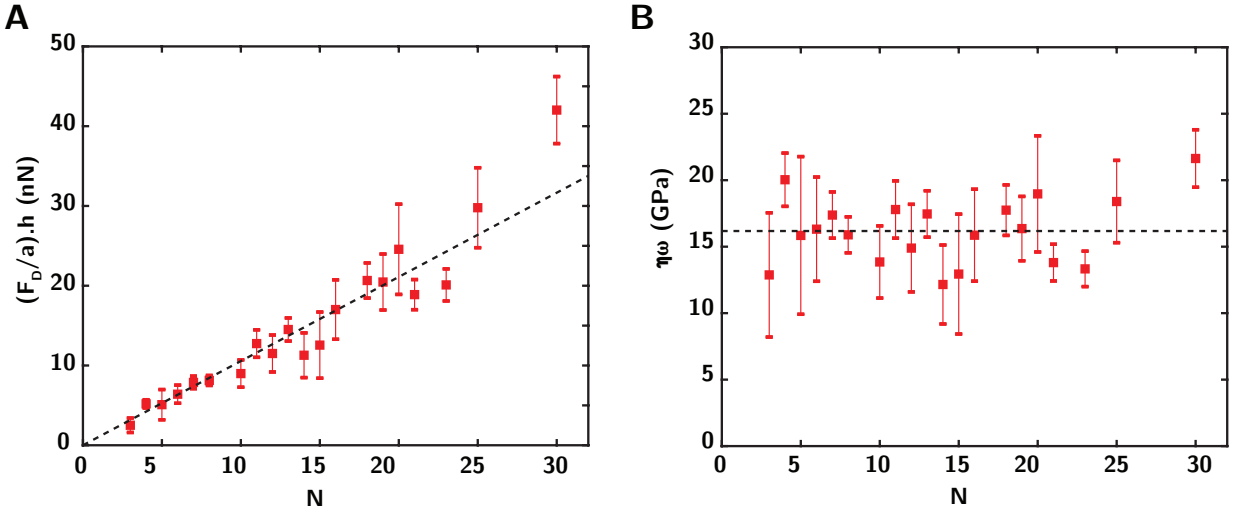

Figure 3.9: (**A**) Hydrodynamic dissipation F_{D}/γ and (**B**) Hydrodynamic stress $\sigma_{\mathrm{H}} = \eta\omega$ as a function of cross-sectional atom number $\mathcal{N}$. Error bars are standard deviation and we take a 10% relative error for single valued point.

To verify this correlation, we plot in Fig. 3.9A the quantity $F_{\mathrm{D}}/\gamma = Z''_{\infty} \cdot h =$ as a

function of the number $\mathcal{N}$ of atoms in a cross-section. F_D/γ is found to vary proportionally to the cross-sectional atom number $\mathcal{N}$.

We thus plot in Fig. 3.9B, the viscous stress $\eta\omega$, characterizing viscous flow in the junction. We find a mean viscous stress $\eta\omega \approx 16$ GPa, leading to a viscosity $\eta \sim 7 \cdot 10^4$ Pa.s. Importantly, the viscous stress $\eta\omega \approx 16$ GPa appears to be of the same order of magnitude as the yield stress $\sigma_Y \sim 5$ GPa. This suggests that the solicitation frequency of the junction might play a key role in the viscous behavior at high shear rates, similar to a fluidizing action as occurring in granular or soft materials. This therefore suggests that the excitation does fix the relaxation time-scale of the junction under strong deformation, in direct line with the behavior of yielding materials - emulsions, foams or granular materials - where the fluidity (inverse viscosity) is fixed by the excitation time-scale itself [4, 12–14].

3.5.3 Frequency dependence of the plastic transition

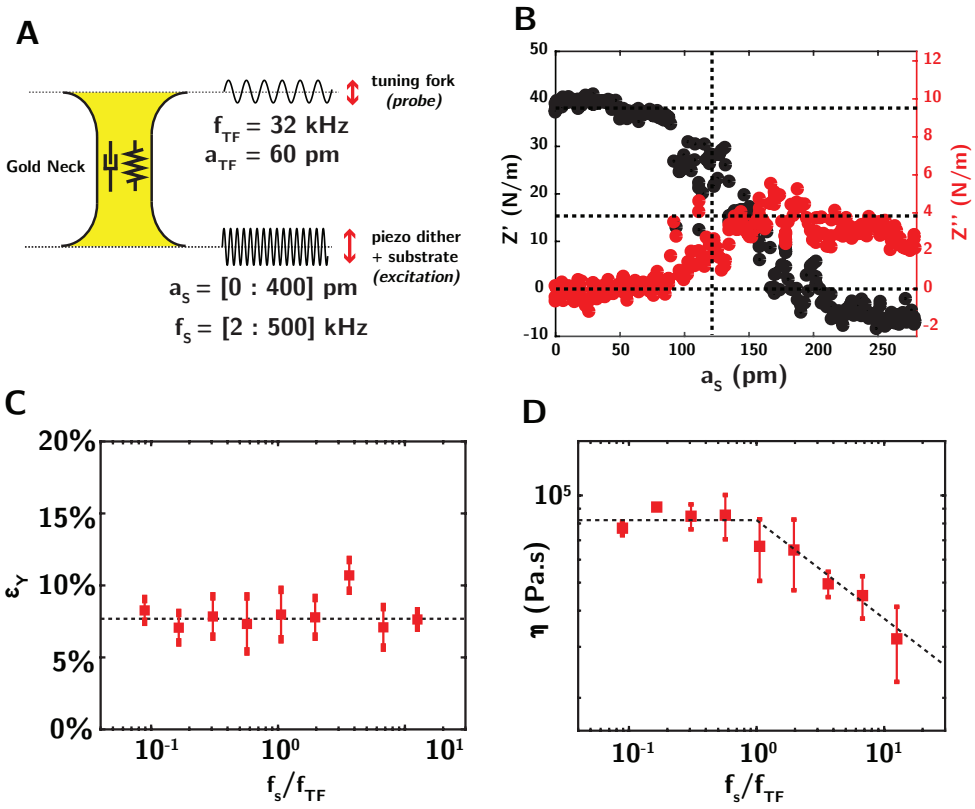

Figure 3.10: **Effect of solicitation frequency on the plastic transition.** **(A)** Schematic of the set-up. An additional piezo dither is placed below the substrate, allowing to shear the junction at an additional frequency $f_s/2\pi$. **(B)** Mechanical impedance Z' and Z'' of the gold junction, as a function of oscillation amplitude a_s of the substrate, with $f_s = 200$ kHz. **(C)** Variation of ϵ_Y as a function of f_s/f_{TF}. Error bars are standard deviation. **(D)** Variation of the viscosity η as a function of f_s/f_{TF}. Dashed black lines are guide to the eyes. Error bars are standard deviation.

To further probe the influence of the frequency on the plastic transition, we use an additional piezo dither to add an additional shearing motion to the substrate (Fig. 3.10). In this configuration, the tuning fork probes the mechanical properties of the junction, with a fixed oscillation amplitude $a_{TF} = 60$ pm (smaller than the critical oscillation amplitude to

induce plastic flow), and the piezo dither is excited at various frequencies from 1 to 500 kHz. Experiments presented in this section are performed for a mean junction conductance $\mathcal{N} = 15$.

We show in Fig. 3.10B, the mechanical impedance of the junction as a function of the oscillation amplitude of the piezo-dither. We recover a similar trace in the mechanical impedance as in Fig. 3.3A, showing that the plastic transition can indeed be *induced* by the oscillation of the piezo dither. Due to the absence of correlation between the tuning fork oscillation a_{TF} and the substrate oscillation a_{s}, we define here the critical oscillation amplitude as $a_{\mathrm{Y}} = a_{\mathrm{TF}} + a_{\mathrm{s}}^{\mathrm{crit.}}$ and critical yield strain $\epsilon_{\mathrm{Y}} = a_{\mathrm{Y}}/h$.

We plot in Fig. 3.10C the critical yield strain ϵ_{Y} as a function of the ratio of substrate excitation frequency over the tuning fork frequency $f_{\mathrm{s}}/f_{\mathrm{TF}}$. The yield strain is found to be independent of the excitation frequency, of order $\epsilon_{\mathrm{Y}} \approx 8$ %, similar to the critical yield strain measured with the tuning fork (see Fig. 3.6). The independence of the yield strain with the oscillation frequency validates our interpretation of the rheological curves as that of a plastic transition set by a critical strain and not by a critical strain rate, as expected for a "granular" system with a characteristic size (here the atomic size of a gold) but no intrinsic timescales.

Additionally, we plot in Fig. 3.10D the viscosity $\eta = Z''_{\infty} \cdot h/(\mathcal{A} \cdot \omega_{\mathrm{s}})$ as a function of the ratio of substrate excitation frequency over tuning fork frequency $f_{\mathrm{s}}/f_{\mathrm{TF}}$. The viscosity η is found to be roughly independent of the excitation frequency for $f_{\mathrm{s}} < f_{\mathrm{TF}}$ and shows a weakening for $f_{\mathrm{s}} > f_{\mathrm{TF}}$ as $\eta = \eta_0 \cdot (f_{\mathrm{s}}/f_{\mathrm{TF}})^{-\alpha}$ with $\alpha \sim 0.28$. The decrease of the viscosity for excitation frequency larger than the tuning fork frequency ($f_{\mathrm{s}} > f_{\mathrm{TF}}$) highlights the dominant role of the tuning fork excitation in the hydrodynamic behavior of the gold junction.

3.5.4 Solid-like dissipation regime at large oscillation amplitude

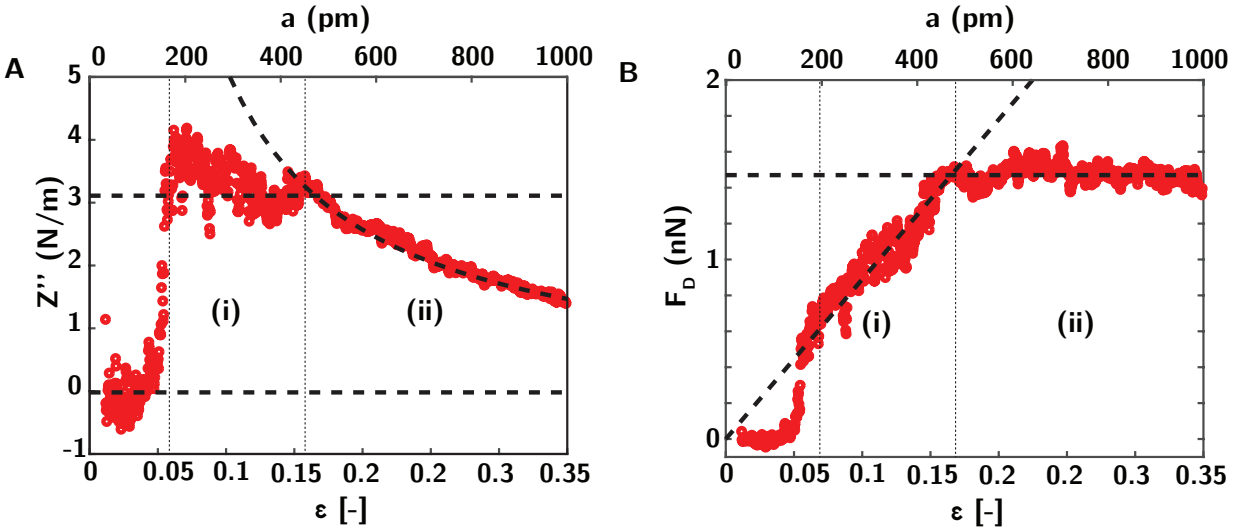

Figure 3.11: Analysis of successive dissipative regimes. **(A)** Dissipative mechanical impedance Z''. **(B)** Dissipative force $F_{\mathrm{D}} = Z'' \cdot a$, as a function of strain $\epsilon = a/h$ and oscillation amplitude a (upper axis).

In all our experiments, the dissipative regime right after the plastic transition exhibit viscous-like behavior, with a constant mechanical impedance Z''_{∞}. However, in few cases,

we can observe a deviation from this behavior for even larger oscillation amplitude or strains. We show in Fig. 3.11 a sample corresponding to a junction of equivalent height $h \approx 2.8$ nm and contact conductance $N = 10$. The variation of mechanical impedance Z'' (Fig. 3.11A) and dissipative force F_{D} (Fig. 3.11B) are plotted with respect to oscillation amplitude a or strain ϵ. For strains between 5 % and 15 %, we observe a linear increase of the dissipative force F_{D} with oscillation amplitude a or strain ϵ as in all of our experiments (regime (i)). A deviation from this behavior is observed for even larger strains $\epsilon > 20$ %, where we evidence a second dissipative regime characterized by a constant (solid-like) dissipative force F_{D} (regime (i) in Fig. 3.11B) and a dissipative impedance Z'' decreasing with oscillation amplitude as $Z'' \sim 1/a \sim 1/\epsilon$. Interestingly, this dissipative solid-like regime observed at very large oscillation amplitude corresponds to the predictions of our analytical Prantl-Tomlinson model, and standard plasticity models, for which plastic flow occurs at a constant stress (section 3.7).

The observation of such behavior in the rare cases where we attain such large strains might express a change in the dissipative plastic behavior at large strains, from a shear-induced viscous-like regime (where dissipation occurs along various distributed slip planes in the junction), to a sliding friction regime (where dissipation is reduced to slip along one shear plane), possibly due to conformational change of the sheared junction.

3.6 Conservative force response and capillary attraction

3.6.1 Capillary attraction

Interestingly, the hydrodynamic/liquid-like behavior associated with the dissipative response of the junction in the plastic regime and uncovered in Section 3.5.2 is also recovered in the conservative response Z' at large oscillation amplitude. As shown in Fig. 3.3B, we measure at large oscillation amplitude an adhesive attractive capillary force, corresponding to a negative measured stiffness $Z' < 0$ (blue zone).

Such adhesive effects are reminiscent of capillary adhesion [5, 9–11], and may express the complete shear-induced melting of the junction, whose mechanical response becomes dominated by surface tension effects. Similarly as in the configuration of a liquid meniscus of surface tension γ perfectly wetting a spherical probe of radius R [9], we can express the associated stiffness as:

$$Z' = -2\pi\gamma\,(R/h) \tag{3.7}$$

Identifying the radius R with the cross-sectional area of the bridge, we find for Fig. 3.3B, $R/h \sim 0.4$ and $Z' \approx -2$ N/m, leading to $\gamma \approx 0.8$ N/m, in very good agreement with the expected value of 1 N/m for gold [19].

3.6.2 Shear induced melting of the junction

A first naive explanation for this liquid-like adhesive behavior of the junction at large oscillation amplitude would be local frictional heating, leading to melting of the gold.

To estimate this local heating of the junction, we write the increase in temperature in the junction as $\mathcal{A} \cdot \lambda \cdot (\Delta T/h) \sim \mathcal{P}_{\mathrm{d}}$, with $\mathcal{P}_d = Z''a^2\omega$ the power dissipated in the junction. We take a conservative estimate, with $\lambda_{\mathrm{gold}} = 314$ W/(mK) corresponding to bulk gold conductivity, dissipated power $\mathcal{P}_{\mathrm{d}} \approx 100$ eV/cycle $\approx 3.2 \cdot 10^{-13}$ W (Fig. 3.12), height $h \approx 6$ nm and area $A \approx 0.3$ nm^2 (Fig. 3.3).

This leads to a local temperature increase ΔT of the order of $2 \cdot 10^{-5}$ K, discarding any frictional heating effects in the melting of the gold nano junction.

Shear induced melting

The liquid behavior of the junction at large oscillation amplitude might thus take its origin in the shear induced melting of the junction. We evaluate this possibility by balancing the work necessary to deform the junction *in volume* as $E_v = \mathcal{A}h\sigma_{\mathrm{Y}}$ with the energy $2\pi Z''_\infty a^2$ injected in the junction over one oscillation cycle due to the shearing motion of the tuning fork.

Using our rheology measurement, we characterize the critical amplitude a_{L} at which a negative stiffness, characterizing the liquid character of the junction is observed (Fig. 3.3).The energy dissipated in the junction per oscillation cycles for the oscillation amplitude a_{L} can then be estimated as:

$$E_{\mathrm{d}} = Z''_\infty \cdot a_{\mathrm{L}}^2 \cdot 2\pi \tag{3.8}$$

Simultaneously, we can estimate the total volume V of the junction based on the measurement of the cross-sectional area A (measured from the contact number $\mathcal{N}$) and height h (estimated from the stiffness at low amplitude Z'_0), such that:

$$V = A \cdot h \tag{3.9}$$

Figure 3.12 shows that those two quantities are well correlated, with

$$Z'' a_{\mathrm{L}}^2 \sim [h\mathcal{A}] \cdot \sigma_{\mathrm{Y}}^{\mathrm{L}} \tag{3.10}$$

Using this energy balance, we find another estimate of the yield modulus as $\sigma_{\mathrm{Y}}^{\mathrm{L}} \approx 1.6$ GPa. We can thus attribute the observed adhesive liquid-like regime to the complete shear induced melting of the junction, due to the increase of density of plastic events in the junction.

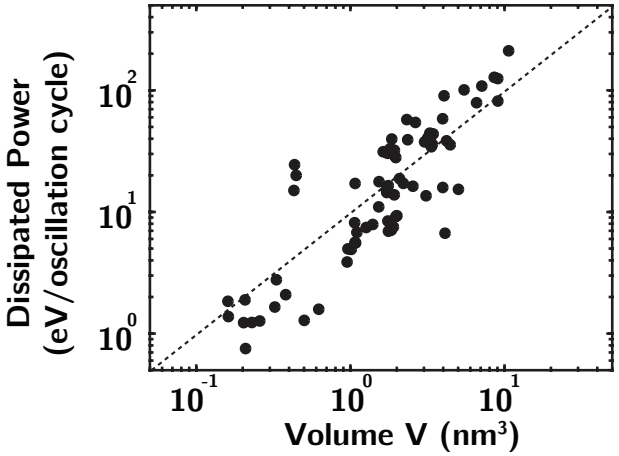

Figure 3.12: Dissipated energy in the junction over one oscillation cycle, as a function of melted volume (see text above for details). The dashed line has a slope 1.

3.6.3 Jump to contact at large oscillation amplitude

Importantly, we observe similar capillary-like signature for the behavior of gold junctions when performing force spectroscopy measurements at large oscillation amplitude $a = 1$ nm in a high vacuum environment (10^{-6} mbar).

Fig. 3.13 shows the approach of an oscillating gold tip on a gold substrate. We observe upon approach a sudden jump to contact, characterized by a negative stiffness $Z' = -4$ N/m (Fig. 3.13A), concomitant with the apparition of a conductance of several G_0 in magnitude (Fig. 3.13B). Upon retraction, an hysteresis of ≈ 1 nm is observed.

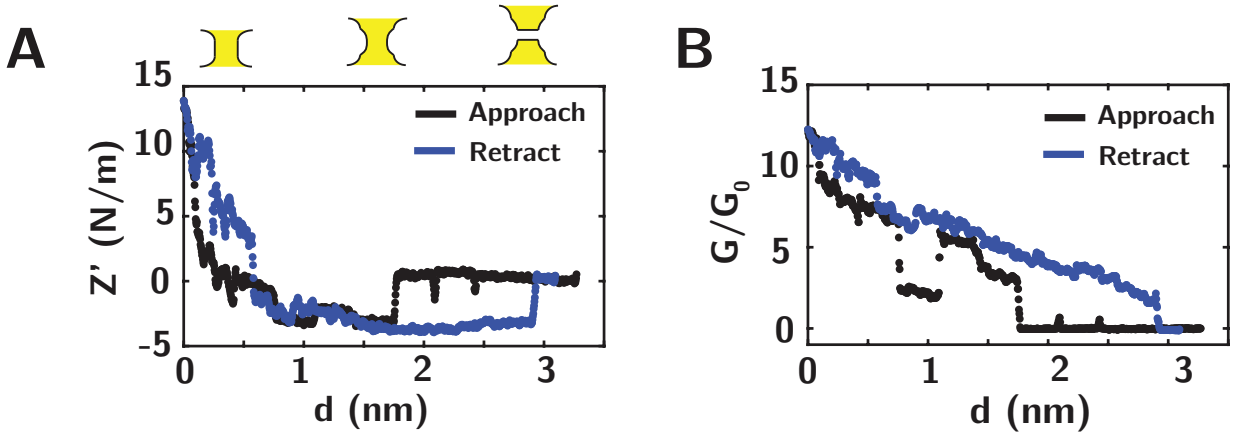

Figure 3.13: Force spectroscopy showing approach (black) and retract (blue) at large oscillation amplitude (1 nm) on the gold substrate for **(A)** the normal stiffness Z' and **(B)** the dimensionless conductance G/G_0.

This "jump to contact", concomitant with the apparition of a metallic conductance of several atomic contact number in value is another signature for the liquid-like nature of gold at large shear rates.

3.7 Prandtl-Tomlinson model

To get more insights into the plastic deformation mechanism at play in the junction and try to rationalize the observed dependence of mechanical impedance on oscillation amplitude, we follow [39, 40] and propose a simple model based on a harmonically driven Thomlinson model, pictured in Fig. 3.14. We model slip between two atomic gold plane as the relative motion of two corrugated surfaces of corrugation amplitude $U_0 \sim 0.4$ eV, periodicity $b \sim 280$ pm and number $\mathcal{N}$ of potential well, leading to an effective interaction potential $U(x) = \mathcal{N}U_0 \sin(2\pi x/b)$.

3.7.1 Equations and non-dimensionalization

Dimensional equations

We follow [39, 40] and describe the motion of a harmonically driven oscillator interacting with a periodic potential as pictured in Fig. 3.14A as:

$$M\ddot{x} + \gamma\dot{x} + Kx + \frac{U_0}{2\pi b}\sin(2\pi x) \quad = \quad F_{\text{ext}}\sin(\omega t) \tag{3.11}$$

where M [kg], γ [kg.s^{-1}] and K [N.m^{-1}] are the effective mass, damping and spring constant of the oscillator, U_0 [J] is the barrier height of the Prandtl-Tomlinson model, b [m] the corrugation period, and F_{ext} [N] is the external forcing due to oscillations. The free oscillator is characterized by its quality factor $Q = M\omega_0/\gamma$ [-] and resonant frequency $\omega_0 = \sqrt{K/M}$ [s^{-1}].

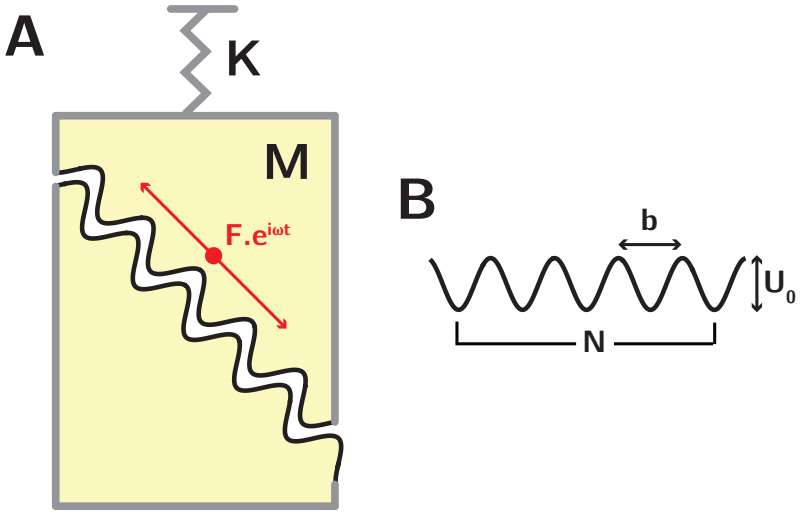

Figure 3.14: **Prandtl-Tomlinson model** (**A**) Schematic of the simulation system, composed of a mass-spring oscillator, with mass M and stiffness K interacting with a corrugated potential, characterizing the slip between two adjacent gold planes (**B**) Corrugated potential of corrugation energy U_0 and corrugation period b, and number $\mathcal{N}$ of potential wells.

Non-dimensionalization

After non-dimensionalization of Eq. 3.11, we obtain :

$$\tilde{\omega}^2\ddot{X} + \frac{\tilde{\omega}}{Q}\dot{X} + X + \alpha\sin(2\pi X) \;=\; \tilde{F}\sin(2\pi t) \tag{3.12}$$

where we defined the dimensionless displacement $X = x/b$, force $\tilde{F} = F_{\text{ext}}/M\omega_0^2$, the dimensionless driving frequency $\tilde{\omega} = \omega/\omega_0$ and $\alpha = U_0/b^2K$, characterizing the relative importance of the corrugation stiffness U_0/b^2 over the probe stiffness K.

Following the same nondimensionalization, we define the dimensionless mechanical impedance as $\tilde{Z} = Z/[NU_0/b^2]$ and the dimensionless dissipative frictional force as $\tilde{F}_{\text{D}} = F_{\text{D}}/[NU_0/b]$.

3.7.2 Simulation procedure

To obtain the variation in Z' and Z'', we numerically solve for the resonance of the tuning fork under a periodic forcing, with a perturbative periodic potential $\alpha = 0.5$.

We can extract the quality factor Q at resonance, and the center frequency of the resonance ω_{r} from the variation of the phase ϕ of the oscillator close to resonance, using:

$$\frac{1}{\tan(\phi)} = \frac{Q(\omega_r^2 - \omega^2)}{\omega\omega_r} \approx -\frac{2Q(\omega - \omega_r)}{\omega_r} \tag{3.13}$$

Measurement of Z'

From the measurements of the shift in resonance frequency ω_{r}, we extract the dimensionless storage modulus $\tilde{Z}'$ as:

$$\tilde{Z}' \;=\; \frac{2}{\alpha}(\tilde{\omega}_r - \tilde{\omega}_0) \tag{3.14}$$

Measurement of Z''

We can express the dimensionless loss modulus $\tilde{Z}''$ as a function of the change in quality factor as:

$$\tilde{Z}'' = \frac{1}{\alpha}\left(\frac{1}{Q} - \frac{1}{Q_0}\right) \tag{3.15}$$

3.7.3 Simulation results and limiting cases

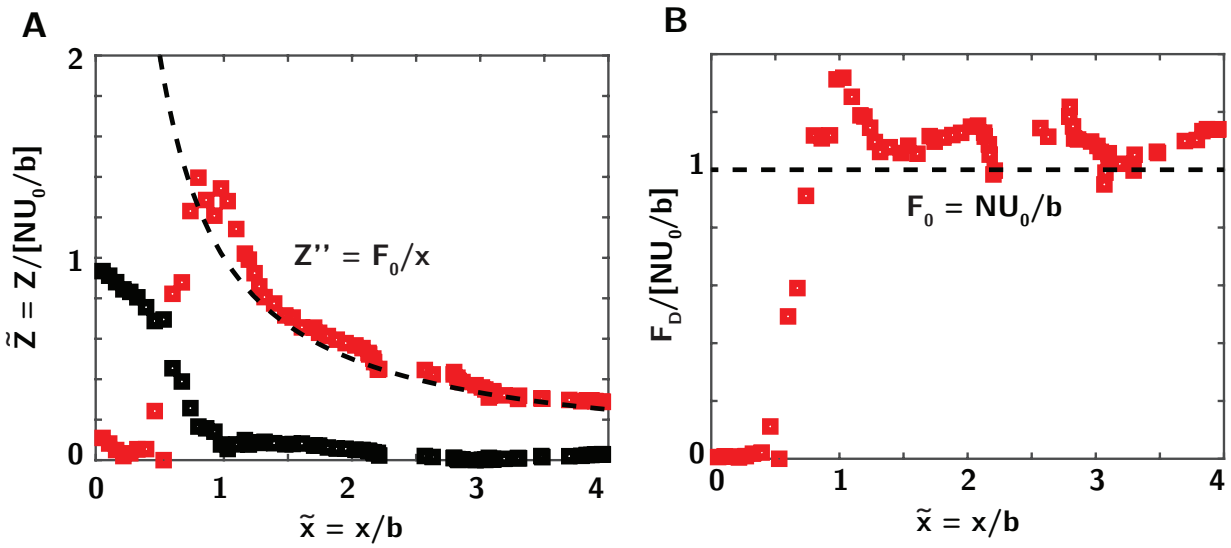

Figure 3.15: **Simulation Results (A)** Dimensionless dissipative and conservative impedance $\tilde{Z}$, as a function of dimensionless oscillation amplitude x/b. **(B)** Dimensionless dissipative force $\tilde{F}_D$ as a function of dimensionless oscillation amplitude x/b.

We show in Fig. 3.15A the effective dimensionless mechanical impedance $\tilde{Z}$ associated with the Tomlinson model and in Fig. 3.15B the associated dimensionless dissipative force $\tilde{F}_{\mathrm{D}}$, as a function of oscillation amplitude $\tilde{x} = x/b$.

Linear response at small oscillation amplitude

For low oscillation amplitudes $x \ll b$, we recover a purely elastic regime associated with $Z' \approx \mathcal{N}U_0/b^2$ and $Z'' \approx 0$, corresponding to the linear response of the system. In this purely elastic regime, we recover a simple relation between the shear modulus G and the barrier height U_0 with $G \sim Z'/(\mathcal{N}b) \sim U_0/b^3$ (see Section 3.4.2).

Solid friction at large oscillation amplitude

As the oscillation amplitude x increases above the potential wavelength b, we recover a plastic regime where adjacent atomic planes slip with respect to each other, characterized by an increase of the dissipative impedance Z'' and a concomitant loss in mechanical impedance $Z' \approx 0$. This regime is associated with a constant solid-like friction force $F_0 \sim \mathcal{N}U_0/b$ corresponding to the force necessary to unpin the row of atoms from its potential, which varies linearly with the number $\mathcal{N}$ of interacting atoms (Fig. 3.15B). This constant friction force leads to an impedance decreasing with oscillation amplitude as $Z'' \sim F_0/x$ (Fig. 3.15A).

3.7.4 Discussion

Using this harmonically driven Prandtl-Tomlinson model, we could recover qualitatively the transition from an elastic regime to a plastic regime, associated with a loss of stiffness and an increase in dissipation as a function of driving amplitude (Fig. 3.15). We recover with this model a yield force varying linearly with the number N of cross-sectional atoms, leading a shear stress σ_Y approximately independent of the cross-sectional area, in agreement with a mechanism involving defect free deformation.

However, this simple model leads to a velocity-independent static frictional force $F_0 = \mathcal{N}U_0/b$ associated with unpinning of the corrugated potential, and a decrease of the mechanical impedance for increasing oscillation amplitude x as F_0/x.

In the range of deformations typically investigated in our experiments (Fig. 3.4), the plastic regime can instead be described by a hydrodynamic regime of dissipation associated with a constant mechanical impedance Z''_∞ at large oscillation amplitude, and a liquid-like viscous friction proportional to the shear rate $\dot{\gamma}$ [s^{-1}] of the junction (Section 3.5.2). Interestingly, this solid-like friction regime uncovered in our Tomlinson model can be recovered in some of our experiments, but only for large deformations ϵ (Section 3.5.4).

3.8 Conclusion

In this Chapter, we investigated the viscoelastic rheological behavior of atomic gold junctions of a few atoms width. Due to ballistic electronic transport in the junction, the conductance varies discretely with the number of atoms in a cross-section, allowing to measure and control the cross-sectional area of the junction atom by atom.

1. **Submitting the junction to increasing shear, we evidenced a transition from (i) an *elastic regime*, characterized by constant stiffness and the absence of intrinsic dissipation in the junction, to (ii) a *plastic regime*, characterized by a decrease in stiffness, an increase in dissipation and an increase in current fluctuations, up to (iii) a *liquid-like regime* characterized by an adhesive force.**

2. **We investigate the dependence of the yield force on junction size, by varying the cross-sectional number of atoms from a contact as low as 3 atoms and up to 30 atoms. The yield force is found to vary approximately linearly with the number of atoms in a cross-section, leading to a yield stress approximately independent of the cross-sectional number of atoms. This linear variation suggests a dislocation-free plastic mechanism for the junction, with plastic flow limited by the direct slip of atomic planes under shear.**

3. **Dissipation in the plastic regime is found to follow a well-defined hydrodynamic friction law with a viscous-like dissipation proportional to the shear rate in the junction. Interestingly, the associated viscous stress $\eta\omega$ is found to be of the order of the yield stress σ_Y, suggesting that the hydrodynamic viscous behavior is induced by the oscillatory shearing action.**

4. **We show that the adhesive behavior of the gold junction at large shear rates is due to the shear-induced liquefaction of the junction, and extract a characteristic surface tension for the liquid gold.**

5. **We attempt to rationalize our results through a harmonically-driven Prantl-Tomlinson model. Our model can recover the transition from the elastic to the plastic regime, but leads to a static constant depinning force at large oscillation amplitude, which does not describe the observed hydrodynamic dissipation regime during plastic flow in our experiments.**

Bibliography

1. Agraït, N., Rubio, G. & Vieira, S. Plastic deformation of nanometer-scale gold connective necks. *Physical Review Letters* **74,** 3995–3998 (1995).
2. Agraït, N., Yeyati, A. L. & van Ruitenbeek, J. M. Quantum properties of atomic-sized conductors. *Physics Reports* **377,** 81–279 (2003).
3. Agraït, N., Yeyati, A. L. & van Ruitenbeek, J. M. Quantum properties of atomic-sized conductors. *Physics Reports* **377,** 81–279 (2003).
4. Bocquet, L., Colin, A. & Ajdari, A. Kinetic theory of plastic flow in soft glassy materials. *Physical Review Letters* **103,** 1–4 (2009).
5. Charlaix, E. & Crassous, J. Adhesion forces between wetted solid surfaces. *Journal of Chemical Physics* **122** (2005).
6. Chen, C. Q., Shi, Y., Zhang, Y. S., Zhu, J. & Yan, Y. J. Size dependence of Young's modulus in ZnO nanowires. *Physical Review Letters* **96,** 1–4 (2006).
7. Chen, M. *et al.* Deformation twinning in nanocrystalline aluminum. *Science* **300,** 1275–1277 (2003).
8. Cohen-Addad, S., Höhler, R. & Pitois, O. Flow in Foams and Flowing Foams. *Annual Review of Fluid Mechanics* **45,** 241–267 (2013).
9. Crassous, J., Charlaix, E., Gayvallet, H. & Loubet, J. Experimental study of a nanometric liquid bridge with a surface force apparatus. *Langmuir* **9,** 1995–1998 (1993).
10. Crassous, J., Charlaix, E. & Loubet, J.-L. Nanoscale Investigation of Wetting Dynamics with a Surface Force Apparatus. *Physical Review Letters* **78,** 2425–2428 (1997).
11. Crassous, J., Ciccotti, M. & Charlaix, E. Capillary force between wetted nanometric contacts and its application to atomic force microscopy. *Langmuir* **27,** 3468–3473 (2011).
12. Dijksman, J. A., Wortel, G. & Van Hecke, M. Rheology of weakly vibrated granular materials. *AIP Conference Proceedings* **1145,** 343–346 (2009).
13. Dijksman, J. A., Wortel, G. H., Van Dellen, L. T., Dauchot, O. & Van Hecke, M. Jamming, yielding, and rheology of weakly vibrated granular media. *Physical Review Letters* **107,** 1–4 (2011).
14. Eisenmann, C., Kim, C., Mattsson, J. & Weitz, D. A. Shear melting of a colloidal glass. *Physical Review Letters* **104,** 8–11 (2010).
15. Espinosa, H. D., Prorok, B. C. & Peng, B. Plasticity size effects in free-standing submicron polycrystalline FCC films subjected to pure tension. *Journal of the Mechanics and Physics of Solids* **52,** 667–689 (2004).
16. Frenkel, J. Zur Theorie der Elastizitatsgrenze und der Festigkeit kristallinischer Korper. *Zeitschrift fur Physik* **37,** 572–609 (1926).
17. Greer, J. R. & De Hosson, J. T. M. Plasticity in small-sized metallic systems: Intrinsic versus extrinsic size effect. *Progress in Materials Science* **56,** 654–724 (2011).
18. Güttinger, J. *et al.* Energy-dependent path of dissipation in nanomechanical resonators. *Nature Nanotechnology* **12,** 631–636 (2017).

19. Kaufman, S. M. & Whalen, T. J. The surface tension of liquid gold, liquid tin, and liquid gold-tin binary solutions. *Acta Metallurgica* **13,** 797–805 (1965).

20. Kraft, O., Gruber, P. A., Mönig, R. & Weygand, D. Plasticity in Confined Dimensions. *Annual Review of Materials Research* **40,** 293–317 (2010).

21. Kuipers, L. & Frenken, J. W. Jump to contact, neck formation, and surface melting in the scanning tunneling microscope. *Physical Review Letters* **70,** 3907–3910 (1993).

22. Lee, S. *et al.* Reversible cyclic deformation mechanism of gold nanowires by twinningâdetwinning transition evidenced from in situ TEM. *Nature Communications* **5,** 1–10 (2014).

23. Lu, W. & Lieber, C. M. Nanoelectronics from the bottom up. *Nature Materials* **6,** 841–850 (2007).

24. Marszalek, P. E., Greenleaf, W. J., Li, H., Oberhauser, A. F. & Fernandez, J. M. Atomic force microscopy captures quantized plastic deformation in gold nanowires. *Proceedings of the National Academy of Sciences of the United States of America* **97,** 6282–6286 (2000).

25. Mate, C. M. *Tribology on the Small Scale: A Bottom Up Approach to Friction, Lubrication, and Wear* 1–354. ISBN: 9780191712098 (2008).

26. Mordehai, D. *et al.* Size effect in compression of single-crystal gold microparticles. *Acta Materialia* **59,** 5202–5215 (2011).

27. Muller, C. & Krans, J. Quantization effects in the conductance of metallic contacts at room temperature. *Physical Review B - Condensed Matter and Materials Physics* **53,** 1022–1025 (1996).

28. Müser, M. H. *et al.* Meeting the Contact-Mechanics Challenge. *Tribology Letters* **65** (2017).

29. Ohnishi, H., Kondo, Y. & Takayanagi, K. Quantized conductance through individual rows of suspended gold atoms. *Nature* **395,** 780–783 (1998).

30. Persson, B. N., Albohr, O., Tartaglino, U., Volokitin, A. I. & Tosatti, E. On the nature of surface roughness with application to contact mechanics, sealing, rubber friction and adhesion. *Journal of Physics Condensed Matter* **17,** 1–62 (2005).

31. Richter, G. *et al.* Ultrahigh strength single crystalline nanowhiskers grown by physical vapor deposition. *Nano Letters* **9,** 3048–3052 (2009).

32. Rubio, G., Agraït, N. & Vieira, S. Atomic-Sized Metallic Contacts: Mechanical Properties and Electronic Transport. *Physical Review Letters* **76,** 2302–2305 (1996).

33. Shiota, T., Mares, A. I., Valkering, A. M. C., Oosterkamp, T. H. & Van Ruitenbeek, J. M. Mechanical properties of Pt monatomic chains. *Physical Review B - Condensed Matter and Materials Physics* **77,** 1–5 (2008).

34. Sun, J. *et al.* Liquid-like pseudoelasticity of sub-10-nm crystalline silver particles. *Nature materials* **13,** 1007–12 (2014).

35. Untiedt, C., Rubio Bollinger, G., Vieira, S., Vieira, S. & Agraït, N. Fabrication and characterization of metallic nanowires. *Physical Review B* **56,** 2154–2160 (1997).

36. Wu, B., Heidelberg, A. & Boland, J. J. Mechanical properties of ultrahigh-strength gold nanowires. *Nature Materials* **4,** 525–529 (2005).

37. Yanson, A. I., Rubio Bollinger, G., Van Den Brom, H. E., Agraït, N. & Van Ruitenbeek, J. M. Formation and manipulation of a metallic wire of single gold atoms. *Nature* **395,** 783–785 (1998).

38. Yu, Q. *et al.* Strong crystal size effect on deformation twinning. *Nature* **463,** 335–338 (2010).

39. Zaloj, V., Urbakh, M. & Klafter, J. Atomic Scale Friction: What can be Deduced from the Response to a Harmonic Drive? *Physical Review Letters* **81,** 1227–1230 (1998).

40. Zaloj, V., Urbakh, M. & Klafter, J. Deducing energy dissipation from rheological response. *The Journal of Chemical Physics* **110,** 1263 (1999).

41. Zhu, Y. *et al.* Size effects on elasticity, yielding, and fracture of silver nanowires: In situ experiments. *Physical Review B - Condensed Matter and Materials Physics* **85,** 1–7 (2012).

Chapter 4

Pairwise Frictional Profile between Particles and the Non-Newtonian Rheology of Suspensions

Contents

Suspensions consist of solid particles in a suspending fluid. They can show a range of non-newtonian behaviors, such as shear-thinning and shear-thickening. In this Chapter, we measure the frictional profile between pairs of particles from PVC and Cornstarch suspensions, and correlate those measurements back to the macroscale rheological behavior of the suspension. We report a clear transition at the nanoscale from a low-friction regime, where pairs of particles support a finite normal load while interacting purely hydrodynamically, to a high-friction regime characterized by hard repulsive contact between particles and sliding solid friction. Critically, we show that the nanoscale pressure needed to enter the frictional regime matches the macroscale critical stress at which shear thickening occurs in suspensions. We further rationalize the two shear-thinning regimes observed before and after the discontinuous shear thickening transition. Our experiments bridge nano and macroscales and provide long needed demonstration of the role of local contact forces between particles in the rheology of non-brownian suspensions.

This Chapter is based on the following papers:

- Comtet, J., Chatté, G., Niguès, A., Bocquet, L., Siria, A., & Colin, A. Pairwise frictional profile between particles determines discontinuous shear thickening transition in non-colloidal suspensions. *Nature communications*, 8, 15633. (2017).
- Chatté, G., Comtet, J., Niguès, A., Bocquet, L., Siria, A., Ducouret, G., Lequeux, F., Lenoir, N., Ovarlez, G. & Colin, A. Shear thinning in non-Brownian suspensions. *Soft matter*. (2018).

4.1 General context

4.1.1 Rheology of non-brownian suspensions

Suspensions are made of solid particles immersed in a liquid. Their flows are ubiquitous in nature and industry: water or oil saturated sediments, muds, crystal-bearing magma, concrete, silica suspensions, cornflour mixtures, latex suspensions and clays are example of dispersions we meet in our everyday life. Despite the numerous studies performed since the pioneering work of Einstein in 1905 [13, 14], their rheological properties remain poorly understood.

In the simplest approximation, we can consider an assembly of non-brownian hard spheres suspended in a fluid of viscosity η_f sheared with shear rate $\dot{\gamma}$, under a constant particle pressure P^p. Dimensionally, in the absence of force scales or time scales coming from inertia, forces associated with contact or thermal (brownian) forces, these systems are

controlled by a single parameter, the viscous number $I_V = \frac{\eta_f \dot{\gamma}}{P^p}$ and have to be newtonian, leading to a proportionality between shear stress σ and shear rate $\dot{\gamma}$.

Strikingly, this analysis does not describe the reality, as suspensions exhibit a wide range of non-newtonian rheological behaviors including shear thinning and shear thickening (Fig. 4.1). Those non-newtonian behaviors suggests the presence of additional force scales related to contact between particles.

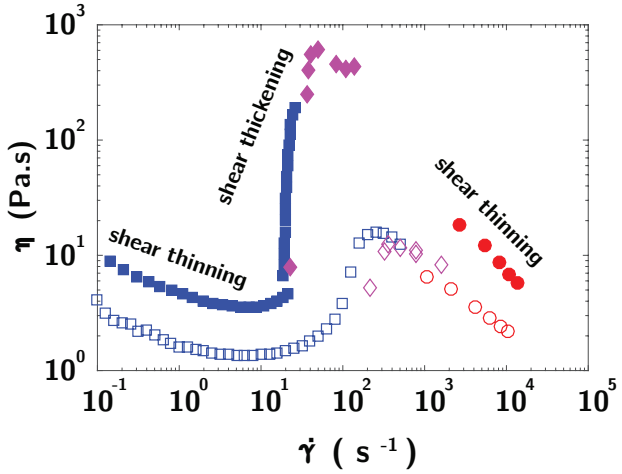

Figure 4.1: Flow curve for PVC suspensions in plasticizer, at 55 % and 60 % volume fraction (See Fig. 4.6 and text for details), showing suspension viscosity η as a function of shear rate $\dot{\gamma}$. One can evidence successive shear thinning, shear thickening and shear thinning regimes.

4.1.2 Shear thickening

Figure 4.2: Snapshot of a person running on top of a pool filled with a dense suspension of cornstarch and water. The fluid can temporarily hold up the person's weight like a solid, sustaining stresses orders of magnitude beyond the capabilities of the suspending Newtonian liquid (here water) (From [6]).

The most striking non-newtonian behavior is shear thickening, which corresponds to an increase of viscosity as a function of the shear rate [20, 42] (Fig. 4.1). In the extreme situation of discontinuous shear thickening, shear viscosity increases by orders of magnitude at a given shear rate, and in cornflour suspensions, the formation of a dynamic jamming

front under impact makes the fluid so resistant that a person can run on it [21, 51]. Industrially, shear thickening can have disastrous effects by enhancing the amount of energy required to pump suspensions at high shear rate, damaging mixer blades or clogging pipes [2]. Discontinuous shear thickening may also be harnessed and desirable when engineering composite materials, for shock-absorbing materials or soft body armor [32]. Despite an extensive characterization of discontinuous shear thickening transitions at the macroscale, there is still no clear understanding of the microscopic mechanisms at play in this transition, principally owing to the challenges associated with quantitative frictional measurements at the nanoscale [17], especially for pairs of particle [18].

A long standing view is that thickening is driven by hydrodynamic and Brownian forces [54]. At large shear rate, these forces create highly dissipative transient clusters of particles, due to the singular lubrication flows between the particles. When normal elastohydrodynamic contact forces are taken into account (without solid friction), these simulations capture continuous shear thickening and large increase in suspension viscosity [24]. However, this model predicts shear rate independent rheology for non-Brownian systems and broader transition that observed experimentally.

In order to get around this issue, recent works [49, 58] proposed a new picture that neglects thermal fluctuations and put forward the role of (nanoscale) repulsive and frictional forces. At low pressure, neighboring particles are separated by a gap filled with solvent and interact via hydrodynamic forces. At high pressures, repulsive forces are overcome, leading to frictional contacts and shear thickening.

At this stage, this picture and the role played by frictional forces have been validated through numerical simulations but only indirectly through experiments at the level of the suspension [9, 20, 35, 46].

4.1.3 Shear thinning

The second recurring non-newtonian behavior occurring in suspensions is shear thinning, which corresponds to a decrease of the viscosity as a function of the shear rate (see Fig. 4.1). Many studies report shear thinning for various suspensions: PMMA particles in PolyEthylene Glycol (PEG) [25], fumed silica particles in PolyPropylene Glycol (PPG) [34], cornstarch particles in water [15], glass spheres in mineral oil [7], cementitious pastes [36], PolyStyrene particles dispersed in PEG [43] and also PVC particles dispersed in a plasticizer [1, 3, 22, 40].

For brownian suspensions, shear thinning can occur due to a competition between diffusion and convection. At low shear rate, particle diffusion is significant and particles occupy a larger effective volume than at high shear rate, leading to a larger viscosity. Explanations concerning shear thinning in non-Brownian suspensions are more vague. At low shear rates, in non-Brownian suspension, shear thinning may occur due to the presence of short-ranged stabilizing repulsive forces between particles. Such thinning has been already observed in charge stabilized suspensions [30, 37] and predicted numerically [38].

Few other mechanisms have been proposed to rationalize the shear thinning behaviors occurring at high shear rates. Using cornflour suspensions, Ovarlez and coworkers [15] showed that the flow at high shear rate after discontinuous shear thickening is inhomogeneous. The system separates into two phases: a dilute one and a concentrated one. This separation is concomitant with a shear thinning behavior. The shear thinning behavior can then be explained as being due to the particular rheological properties of the two shear induced phases and to the evolution of their respective size under shear. However,

this explanation may not be universal, as some dispersions display shear thinning by flowing homogeneously. Inspired from the old order-disorder theory of Hoffman et. al. [22], Nakajima et. al. [41] explained the shear thinning at high shear rate by the breakdown of spanning clusters to smaller size, releasing the trapped plasticizer and increasing the maximum packing density; thus causing a decrease of viscosity at high shear rate. More recently, elastohydrodynamic interactions have been proposed to explain the shear thinning behavior [25, 26]. Under high normal load and shear rates, the particles may deform via a lubricating liquid film opposing contact between particles. Last but not least, Vazquez-Queseda [52] and coworkers have proposed recently that shear thinning might be related to the non-Newtonian properties of the solvent at ultra high shear rates, assuming that the shear rate in the film between particles might be much greater than the applied one.

4.2 Experimental Set-up

4.2.1 Measuring normal and tangential force profiles between two approaching beads with the AFM

We present in Fig. 4.3a the schematic of the experimental set-up used to measure the force profile between pairs of particles. First, we glue an electrochemically etched tungsten tip of approximately 50 nm end radius to the quartz tuning fork. Using an in-house-built nano-manipulator in a scanning electron microscope (SEM), we then glue one individual particle to the end of the tungsten tip (Fig. 4.3b), using SEMGLU from *kleindiek*, and a nanomanipulation station in-situ a SEM (*FEI Nova NanoSEM 450*).

During a typical experiment, the attached particle is immersed in solvent and brought into contact to another bead fixed on the substrate, while monitoring the force profile (Fig. 4.3a).

As detailed in Chapter 1, to measure simultaneously normal and tangential force profiles between the two approaching particles, we simultaneously excite the tuning fork via the piezo-dither at two distinct resonance frequencies $f_{\mathrm{N}} \approx 31$ kHz and $f_{\mathrm{T}} \approx 17$ kHz, corresponding to the excitation of both normal (N, blue arrows) and shear modes (T, red arrows) of the tuning fork, as shown in Fig. 4.3c. Both modes correspond to symmetric excitation of the prongs, leading to negligible motion of the center of mass and high quality factor of the oscillator [31]. Monitoring changes in the resonance of each modes (Fig. 4.3d) allows us to measure respectively the normal and tangential force profile between the two objects, characterized by the normal and tangential force gradient ∇F_i [N.m^{-1}], and normal and tangential dissipative frictional forces F_{D}^i with $i \in \{N, T\}$.

4.2.2 Particles, substrate and solvent

To compare local AFM measurements and macroscopic rheology, we used two distinct systems, consisting of PVC particles suspended in various solvents [55, 56] and cornstarch particles suspended in water [16, 39].

PVC dispersions

We used two dispersions D1 and D2 of PVC particles. All AFM experiments were performed with suspension D1.

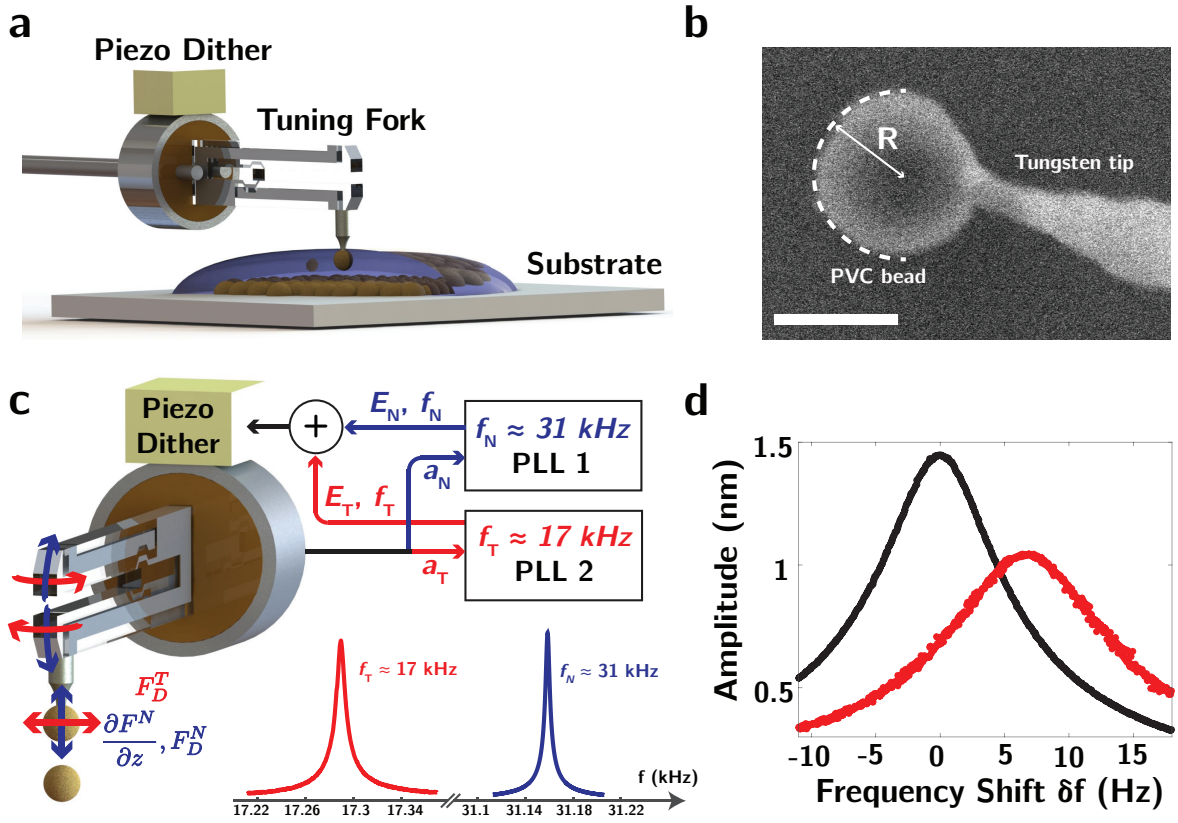

Figure 4.3: **Experimental set-up**. **(a)** Schematic of the set-up. A particle is glued to the quartz-tuning fork based AFM, immersed in the liquid and approached to the substrate, made of casted particles. **(b)** SEM image of a 0.6 µm radius PVC bead glued to the tungsten tip. Scale bar is 1 µm. **(c)** During the experiment, the tuning fork is excited at two distinct frequencies, corresponding to mechanical oscillation of both normal (N, blue) and tangential/shear (T, red) modes. Two Phase Locked Loops (PLL) track the frequency of the resonance peaks, allowing characterization of normal and tangential force gradients $\nabla \mathbf{F}$ and dissipative frictional forces F_{D}. **(d)** Typical resonance curve of the normal mode, for a bead in liquid (black) and in contact to another bead on the substrate (red).

In the first dispersion (D1), the mean particle radius, defined as $R_{32} = \langle R^3 \rangle / \langle R^2 \rangle$ is 1 µm. The size distribution is lognormal and the standard deviation estimated using the volume distribution is 45%. In the second dispersion (D2), the particle size histogram using a volume distribution is trimodal with lognormal peaks around 350 nm (standard deviation of 25%), 3.3 µm (standard deviation of 55%) and 20 µm (standard deviation of 22%). Both dispersions will reach Peclet numbers ($Pe = \frac{6\pi\eta_s R^3 \dot{\gamma}}{k_b T} \sim 250\dot{\gamma}$ with η_f the suspending fluid viscosity, $\dot{\gamma}$ the shear rate and R the particle radius) in the range of 10-10^6 for which Brownian effects are practically negligible [11].

Plasticizer and mineral oil

As a plasticizer for PVC particles, we use 1,2-cyclohexane dicarboxylic acid di-isononyl ester (Dinch) supplied by BASF. This organic liquid Dinch enters the particles and creates a polymer brush around them. This brush enables suspension stabilization due to steric repulsion [56]. At high temperature ($T \geq 100$°C), Dinch can dissolve the PVC particles

[59]. At room temperature, this process is much slower and takes more than one year.

Degree of plasticization can be changed by using a mix of mineral oil and plasticizer [55] because mineral oil has a low affinity with PVC. Mineral oil viscosity standards were provided by *Paragon Scientific Ltd.* Same viscosity as Dinch (41.1 mPa.s at 25°C) was achieved by mixing two different viscosity standards (55.7 mPa.s and 29.0 mPa.s). Resulting viscosity was checked in a shear rate range from 1 to 100 s^{-1} for different temperatures. Same viscosity at 25°C and same temperature dependence of viscosity (range 20-25°C) were found between plasticizer and obtained mineral oil.

Concerning PVC, we report results (both AFM and rheological experiments) for three different plasticizing liquids: (1) 100 vol.% plasticizer; (2) 90 vol.% plasticizer + 10 vol.% mineral oil; (3) 67 vol.% plasticizer + 33 vol.% mineral oil.

PVC substrate

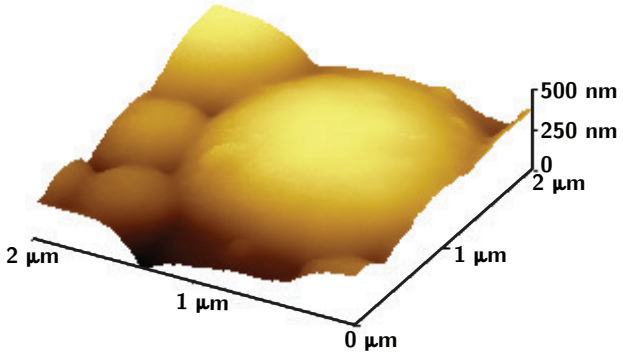

Figure 4.4: **AFM image of one casted PVC particle at the surface of the substrate.** RMS roughness is ≈ 2.2 nm on the upper part of the particle.

To make the substrate, a given amount of PVC powder is introduced into a metallic mold laying on a glass slide. A counter-mold is used on top. The mold and counter-mold are then transferred into a hot press and compressed 5 min at 150°C and 20 bars. Then, the sample is cooled down, resulting in a compact and transparent piece of PVC. Even if the pressing temperature is higher than the PVC glass transition temperature ($T_g = 80$°C), the original shape and surface topography of the particles is preserved (see Fig. 4.4). We measured a RMS roughness of 2.2 nm for PVC particles from D1.

Randow Close Packing fractions for PVC

The random close packing fractions ϕ_{RCP} of these dispersions are measured. ϕ_{RCP} corresponds to the value of the solid fraction at which the viscosity diverges at low shear rate under the hypothesis of frictionless particles [57]. We measure the value of the viscosity at $\dot{\gamma} = 10$ s^{-1} to get rid of interparticle interactions at low shear rate [8]. The data are fitted using a Krieger-Dougherty model $\eta = \eta_s(1-\frac{\phi}{\phi_{RCP}})^{-n}$, where η_s is the solvent viscosity. We get $\phi_{RCP} = 69.4\% \pm 0.25\%$ for D1 suspensions and $\phi_{RCP} = 77.2\% \pm 0.25\%$ for D2. The exponents n of the Krieger-Dougherty models are respectively $n = 2.3$ for the D1 dispersion and $n = 2.9$ for the D2 dispersion. η_s is equal to 41 mPa.s.

Cornstarch

Cornstarch was supplied by Sigma Aldrich and used without further modification. It contains approximately 73% amylopectin and 27% amylose with particle diameter around 14 µm (polydispersity 40% from static light scattering) [39]. Due to very low volume used and evaporation related problems, AFM measurements for cornstarch were done in pure water as a suspending liquid. Rheological measurements were also carried out in pure water for the cornstarch suspensions. Substrates were made by gluing cornstarch particles on a flat silicon substrate using cyanoacrylate glue (see Fig. 4.5). We measured a RMS roughness of 14 nm for the cornstarch particles.

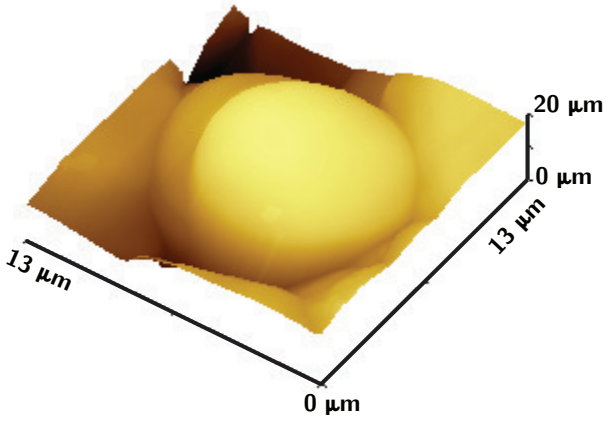

Figure 4.5: **AFM image of one cornstarch particle at the surface of the substrate.** RMS roughness is ≈ 14 nm on the upper part of the particle.

4.2.3 Rheology of macroscopic suspensions

Preparation of PVC suspensions

We prepare our dispersions by weighting a given amount of PVC particles, a given amount of Dinch and a given amount of mineral oil. The solid fractions are then calculated knowing the density of PVC $\rho_{\text{PVC}} = 1.38$ g.cm^{-3}, the density of Dinch $\rho_{\text{Dinch}} = 0.95$ g.cm^{-3} and the density of mineral oil $\rho_{\text{oil}} = 0.84$ g.cm^{-3}. Suspensions are stirred 5 min at 1000 rpm using a *Dispermat LC55* (VMA Getzmann) to ensure good dispersion state. Samples were freshly mixed for each experiment. This protocol was found to produce reproducible samples. The solid volume fraction of the suspension is defined as the volume of particles divided by the total volume: $\phi = [m_{\text{PVC}}/\rho_{\text{PVC}}]/[m_{\text{PVC}}/\rho_{\text{PVC}} + m_{\text{solvent}}/\rho_{\text{solvent}}]$.

Rheology of PVC suspensions

For normal stress differences lower than 1000 Pa, rheological measurements were performed on a stress-controlled rheometer (DHR-3 from TA instruments) or on a strain controlled rheometer (ARES from TA instruments). We used either a Couette cell (gap $e = 1$ mm, inner radius $R_1 = 14$ mm, and height $H = 42$ mm) with smooth surfaces or a cone-and-plate geometry with smooth surfaces of diameter 25 mm (diameter $D = 40$ mm, angle = 2°, truncation gap = 54 µm). The temperature was fixed at 25^{o}C. No wall slip was measured in these experiments. This was checked indirectly by measuring velocity profiles using ultrasounds in Couette cells.

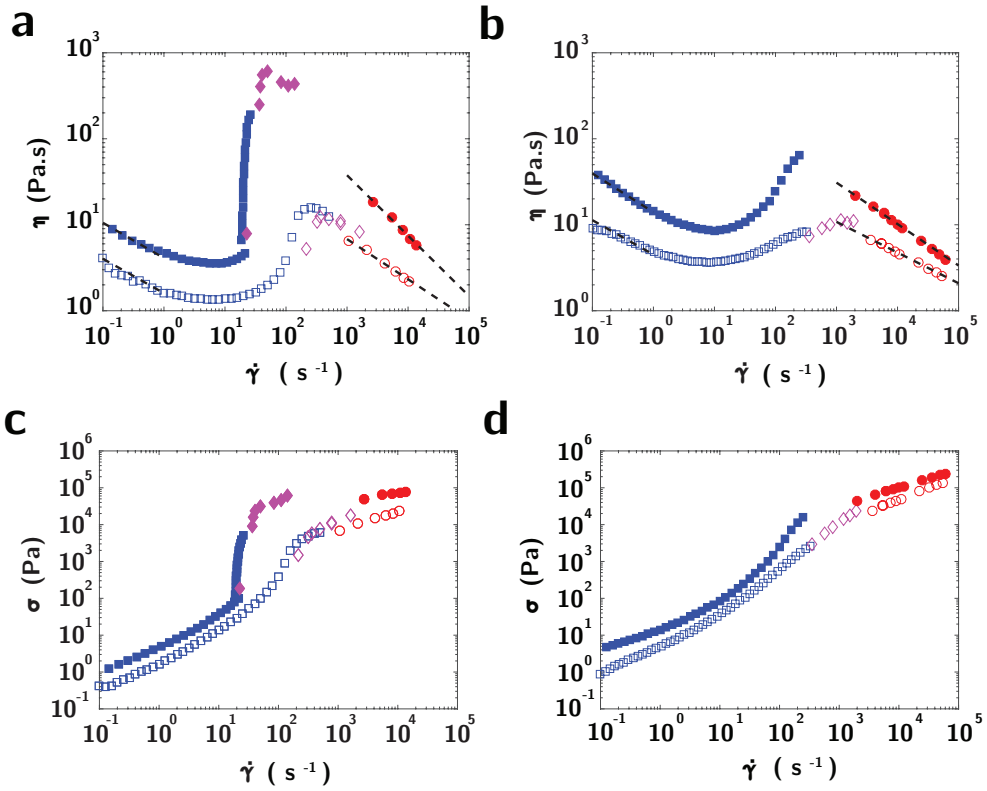

Figure 4.6: **(a)** Flow curves $\eta(\dot{\gamma})$ of D1 55 % (open symbols) and 60 % (closed symbols); **(b)** Flow curves of D2 60% (open symbols) and 64 % (closed symbols); **(c)** same as (a) but for $\sigma = \mathrm{f}(\dot{\gamma})$; **(d)** same as (a) but for $\sigma = \mathrm{f}(\dot{\gamma})$. For all curves, blue squares are obtained from rotational rheometer; purple diamonds from in house-built capillary rheometer and red circles from commercial capillary rheometer. Dotted lines are power law fits of $\eta = \mathrm{g}(\dot{\gamma})$.

The rheometer measures (or imposes depending upon the controlled mode) both the torque Γ exerted on the geometry and its angular velocity Ω in real-time. From Ω and Γ, a global shear rate $\dot{\gamma}$ and a global shear stress σ were computed as a function of time.

High shear rate rheology of PVC suspensions

To measure the rheological properties over a large range of shear rate, we combined measurements from both rotational and capillary rheometers. Home-made capillary rheometers consist in a manometer (pressure range 0-8 bars) plugged on compressed air network 0 - 7 bars), a syringe with a piston and a capillary firmly plugged to the syringe. Capillary rheometers measure or impose the drop of pressure ΔP required to get a given flow rate Q. From these data, they compute a shear rate at the wall $\dot{\gamma}_w$ and a shear stress at the wall σ_w. The viscosity is then defined as $\eta = \sigma_w/\dot{\gamma}_w$.

Preparation and rheology of Cornstarch suspensions

Dispersions were also prepared by weighting a given amount of cornstarch and a given amount of water. The solid fractions are then calculated knowing the density of cornstarch $\rho_{\mathrm{cornstarch}} = 1.63$ g/cm^3 and the density of water $\rho_{\mathrm{water}} = 1.00$ g/cm^3. The solid volume

fraction of the suspension is also defined as the volume of particles divided by the total volume. Samples were freshly mixed for each experiment.

Rheology was measured using a stress controlled DHR-3 rheometer (TA Instruments) equipped with a hatched plate (diameter D = 40 mm) like in previous works [39]. Contrary to PVC suspensions, both lower and upper plate are hatched to avoid wall slip. Flow curves were obtained with a logarithmic stress sweep from 0.1 to 100 Pa (10 points/decade). Each point was measured during 10 s which was long enough to ensure equilibrium while avoiding water evaporation and/or particles sedimentation.

Caracterisation of the DST transition

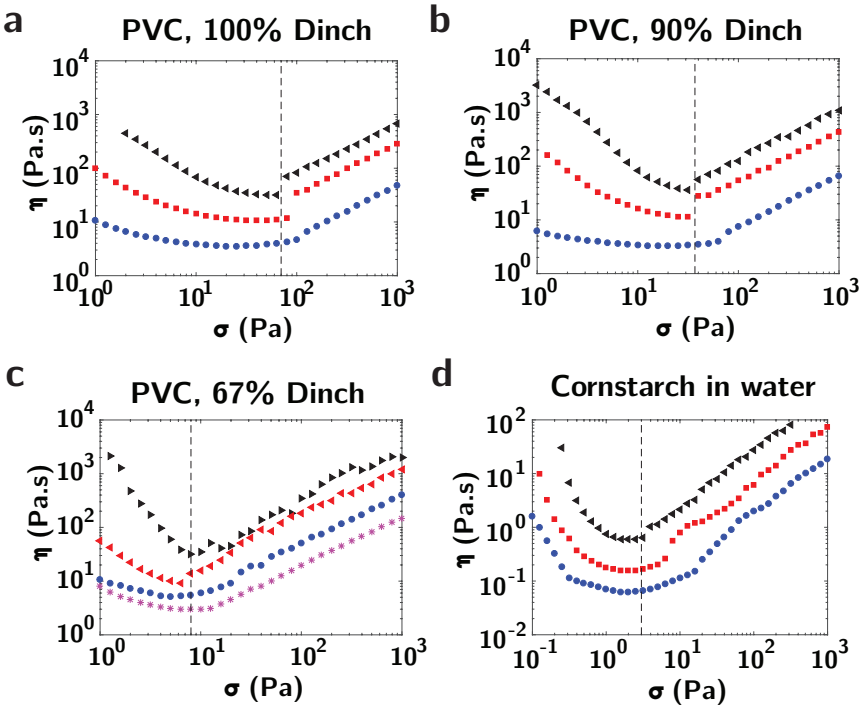

Figure 4.7: **Characterization of the Discontinuous Shear Thickening transition.** Measurements of the viscosity as a function of the shear stress for various solid volume fractions. **(a)** PVC D1, 100% Dinch, from top to bottom the solid fractions correspond to 66%, 64%, 60%. The dotted line corresponds to the shear stress σ_c above which discontinuous shear thickening occurs. **(b)** PVC D1, 90% Dinch; from top to bottom the solid fractions correspond to 66%, 64%, 60%. **(c)** 67% Dinch, from top to bottom the solid fractions correspond to 63%, 62%, 60% 58%. **(d)** Cornstarch suspension in water, from top to bottom the solid fractions correspond to 44%, 42%, 40%.

Ah high stresses (see Fig. 4.7), both PVC and cornstarch suspensions exhibit Discontinuous Shear Thickening (DST) where the gradient d(log η)/d(log σ) reaches 1 (vertical flow curve when plotting $\eta = f(\dot{\gamma})$). Within experimental uncertainty, shear thickening begins at a fixed onset stress which depends only on the studied system and not on the volume fraction ϕ [20] (see dotted lines on Fig. 4.7).

We focus here on particles from the D1 suspension. For PVC particles in a suspending liquid made of 100 vol.% plasticizer, an onset stress of 75 ± 5 Pa is found. For PVC particles in a suspending liquid made of 90 vol.% of plasticizer, an onset of 38 ± 5 Pa is measured,

and for PVC particles in a suspending liquid made of 67 vol.% of plasticizer an onset of 8 ± 2 Pa is found . For cornstarch particles suspended in pure water, an onset stress of $3 - 4$ Pa in found very close to previous works [16, 39].

4.3 Nanoscale force profile

4.3.1 Typical approach curve

We show in Fig. 4.8 the typical force profile measured between two approaching PVC beads in good solvent. Monitoring changes in the resonance for the two oscillating modes allows us to characterize pairwise interparticles interactions through the normal dissipation $F_{\mathrm{D}}^{\mathrm{N}}$ (Fig. 4.8b), the projection of the normal force gradient along the normal direction - $\partial F_{\mathrm{N}}/\partial z$ (Fig. 4.8c) and the tangential friction force $F_{\mathrm{D}}^{\mathrm{T}}$ (Fig. 4.8d).

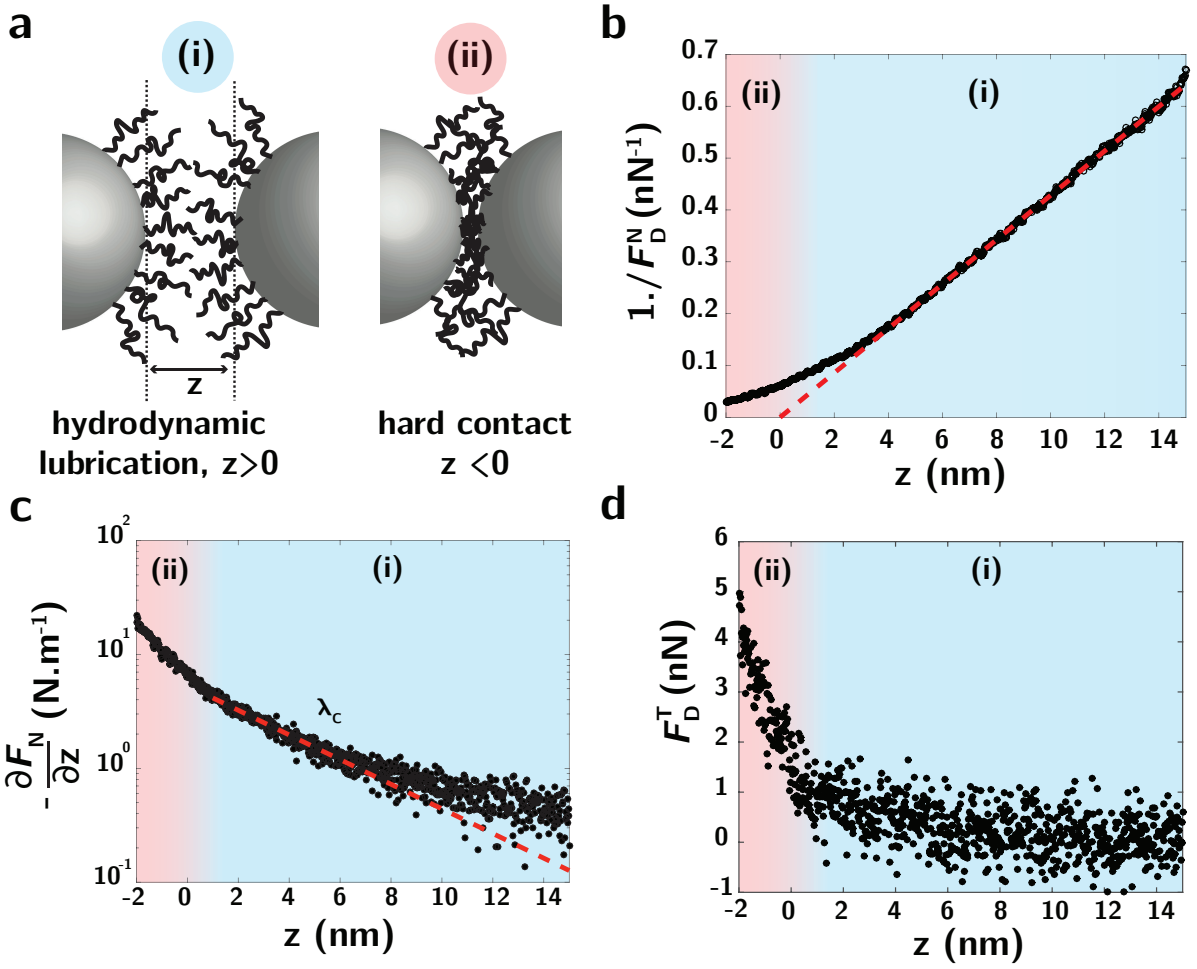

Figure 4.8: **Characterization of nanoscale force profile.** **(a)** When immersed in Dinch a good solvent, polymer brush form at the surface of PVC particles. Distance between bead's no shear plane is written z, where $z = 0$ correspond to hard contact. *(i)* $z > 0$ Entropic repulsion between polymer brushes. *(ii)* $z < 0$ hard contact. **(b)** Inverse of the normal dissipative force $1/F_{\mathrm{D}}^{\mathrm{N}}$. **(c)** Projection of the normal force gradient along the normal direction $-\partial F_{\mathrm{N}}/\partial z$. **(d)** Tangential friction force $F_{\mathrm{D}}^{\mathrm{T}}$. The radius of the attached bead is 0.6 µm and beads are immersed in pure Dinch.

4.3.2 Normal dissipative force

We first show in Fig. 4.8b the inverse of the normal dissipative force $1/F_{\mathrm{D}}^{\mathrm{N}}$. The red line is a linear fit of the inverse dissipation, showing that normal dissipation $F_{\mathrm{D}}^{\mathrm{N}}$ is characterized by hydrodynamic drainage and Stokes law as the beads are separated from each other:

$$F_{\mathrm{D}}^{\mathrm{N}} \sim \frac{\eta R^2 v}{z} \tag{4.1}$$

where $\eta \approx 40$ mPa.s is solvent viscosity, $v = a\omega$ [m.s^{-1}] is the typical speed of the oscillating particle, z [m] is the distance between the two no-shear planes and R [m] is an equivalent bead radius. The intersection of the red line with the horizontal axis defines the hydrodynamic zero ($z = 0$), which defines the absolute position of the no-shear planes between the two objects (vertical dotted lines Fig. 4.8a). This zero defines two domains, corresponding to (i) $z > 0$, hydrodynamic lubrication (light blue) and (ii) $z < 0$ hard contact (light red). Note that for confinement below ≈ 3 nm, we observe a deviation from Stokes hydrodynamics with a regularization of the hydrodynamic divergence, possibly stemming from elastohydrodynamic interactions [24, 33, 53]. The dissipative normal forces measured for $z < 0$ may be due to viscoelasticity of the PVC particles.

The effective viscosity of the PVC polymer brushes can be measured through a fit of normal dissipation (Eq. 4.1). We first calibrate normal dissipation by approaching the casted particle substrate in a mineral oil of similar viscosity as the plasticizer, but for which no polymer brushes are created. Doing approaches this time in the plasticizer, we find similar viscosities showing that the polymer brushes do not seem to impede the flow.

4.3.3 Normal force gradient

We now turn to the normal force gradient $-\partial F_{\mathrm{N}}/\partial z$ [N.m^{-1}] shown in Fig. 4.8c. For the two approaching particles, we observe an increasing repulsive normal force gradient ($-\partial F_{\mathrm{N}}/\partial z > 0$) before contact between the two particles ($z > 0$, blue zone). These repulsive forces vary steadily and smoothly with distance, while normal dissipation is dominated by hydrodynamics during the approach (Fig. 4.8b). We thus interpret these repulsive forces as a signature of the entropic repulsion between polymer brushes forming at the surface of the PVC beads, due to the effect of the plasticizing solvent [19, 56] (Fig. 4.8a). We can characterize the steepness of this repulsive profile right before contact by an exponential-like law $F \approx \exp(-z/\lambda)$ with $\lambda \approx 4$ nm (Fig. 4.3c, red dotted line) [23]. Upon contact, the steepness of the repulsive profile increases slightly.

4.3.4 Tangential dissipative force

We show in Fig. 4.8d the tangential dissipative friction force $F_{\mathrm{D}}^{\mathrm{T}}$ (tangential mode T, Fig. 4.3c). Before contact (blue zone (i)), tangential forces are below 1 nN, consistently smaller that the normal hydrodynamic dissipative forces which are of the order of 5 to 10 nN. Upon contact (red zone, (ii)), we observe a clear increase of frictional forces. We note that, depending on the respective surface states of the beads, contact can also occur before the hydrodynamic zero (for $z > 0$), due to the presence of asperities on one of the bead surface (See Fig. 4.9). Finally, we note that the fact that we recover solvent viscosity η in the dissipative normal force and that there is low tangential lubrication forces before contact are a signature of the absence of brush interpenetration in the probed experimental conditions [28].

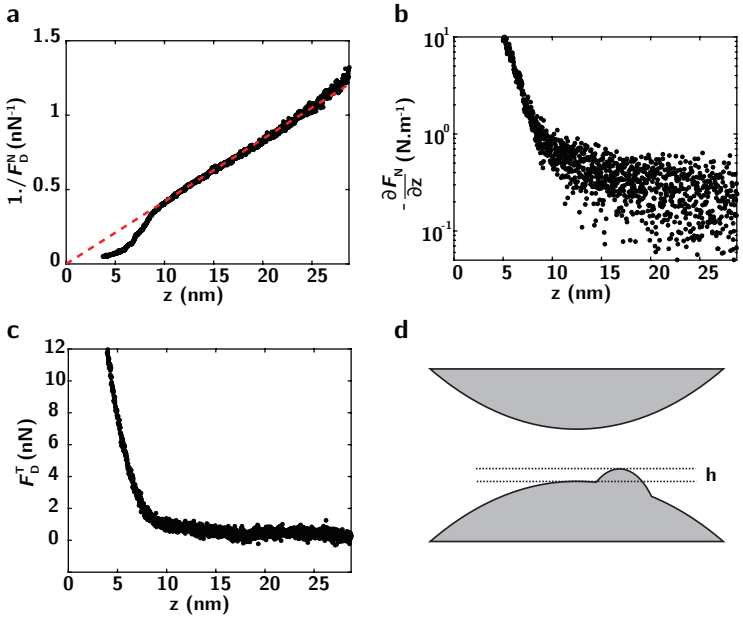

Figure 4.9: **Typical approach in plasticizer (100% Dinch) between two PVC particles in presence of a surface asperity.** The attached particle is 0.6 µm radius. **(a)** Inverse normal dissipation. **(b)** Normal force gradient **(c)** Tangential dissipative force. **(d)** Schematic of contact configuration, with an asperity of height $h \approx 8$ nm present on the bead attached to the substrate.

4.3.5 Approach in presence of a surface asperity

We show in Fig. 4.9 an approach in presence of a surface asperity on the particle attached to the substrate, for which contact occurs here at ≈ 8 nm before the hydrodynamic zero. This contact is traduced by a sudden breakdown of hydrodynamic normal dissipative drainage force at a finite distance between the two beads.

4.3.6 Approach between cornstarch particles

Force spectroscopy on cornstarch particles, as shown in Fig. 4.10 are qualitatively similar to the one on PVC during the approach.

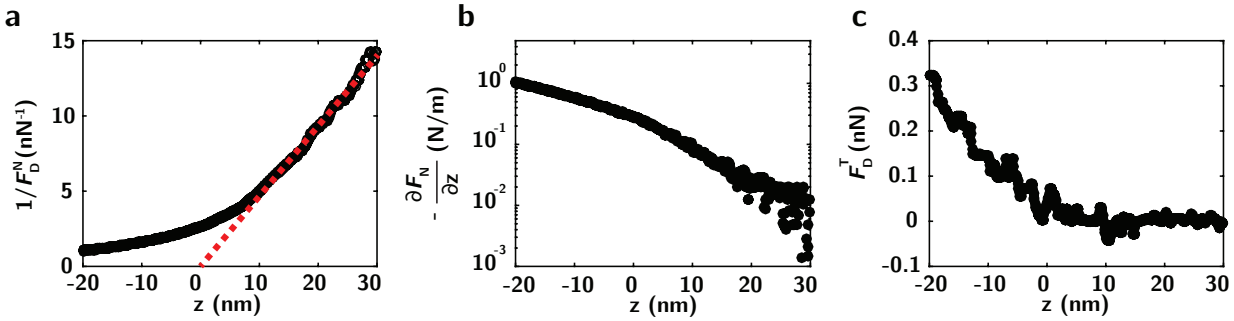

Figure 4.10: **Typical approach curve between two cornstarch particles.** The attached particle is 3.8 µm radius. **(a)** Inverse normal dissipation. **(b)** Normal force gradient **(c)** Tangential dissipative force.

4.4 Frictional force profile

4.4.1 Characterization of the frictional regime

We now turn in Fig. 4.11 to the nature of the frictional profile, as uncovered by the two regimes shown in Fig. 4.8. We plot in Fig. 4.11a the typical form of the tangential dissipative force $F_{\mathrm{D}}^{\mathrm{T}}$ as a function of the normal load F_{N}, obtained by integrating the normal force gradient [47]. In the first regime of hydrodynamic lubrication (blue zone, (i)), tangential frictional forces are small, and arise purely from hydrodynamic interactions while a normal load F_{N} can be sustained due to entropic repulsion of the brushes. This situation results in a friction coefficient as low as $\mu \approx 0.02$, as observed in previous friction studies on polymer brushes in SFA [4, 27–29, 48].

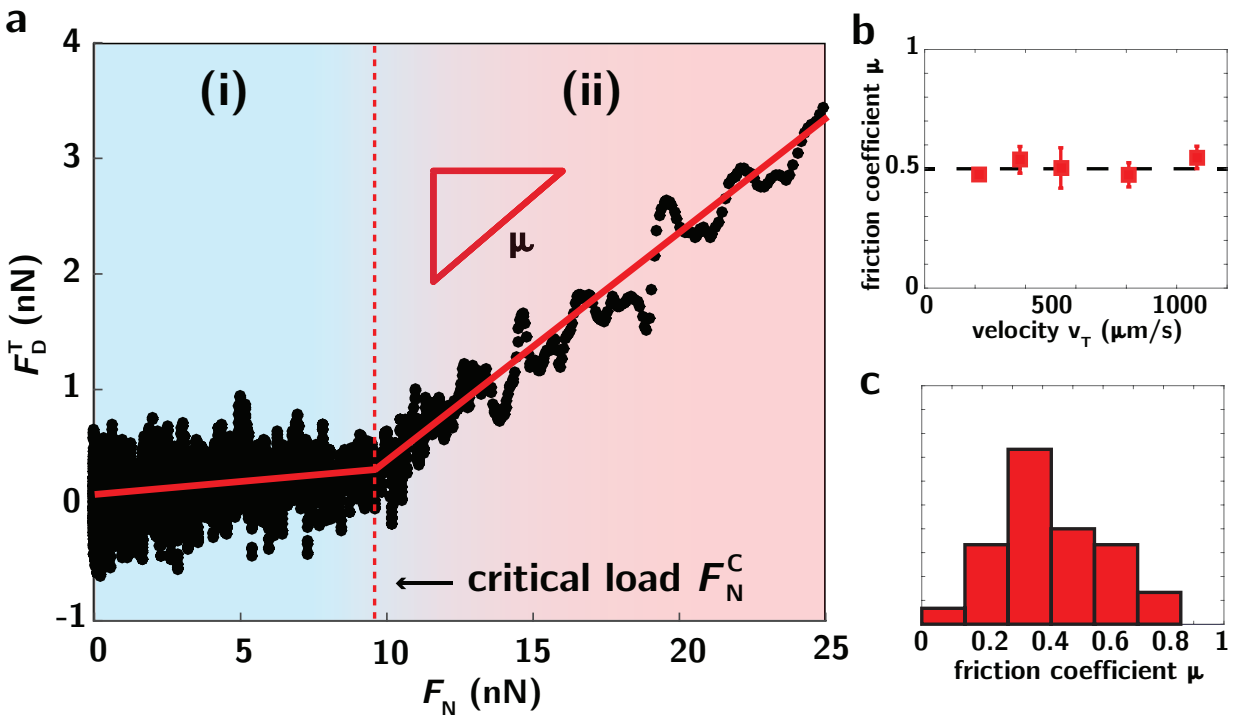

Figure 4.11: **Critical load frictional profile.** **(a)** Tangential friction forces versus normal load, showing a transition between (i) a hydrodynamically lubricated low friction regime, to (ii) a solid-like high friction regime. **(b)** Variation of the friction coefficient μ with sliding velocity v for one pair of beads. Error bars are *s.e.m.* for $N > 2$. **(c)** Distribution of the friction coefficient found on 30 different pairs of beads. The radius of the attached bead is 0.5 μm and the solvent between the two beads is pure Dinch.

Upon a critical normal load $F_{\mathrm{N}}^{\mathrm{C}}$ corresponding to the force necessary to completely compress the polymer layers and reach hard contact, the system switches to a second state characterized by a sharp increase in friction (Fig. 4.8d, red zone (ii)). This second regime is well characterized by Amontons-Coulomb laws, with a proportionality between tangential frictional forces and normal load: $F_{\mathrm{D}}^{\mathrm{T}} = \mu(F_{\mathrm{N}} - F_{\mathrm{N}}^{\mathrm{C}}) + F_{\mathrm{V}}^{\mathrm{C}}$, where $F_{\mathrm{V}}^{\mathrm{C}}$ is the tangential viscous dissipation right before contact. Moreover, as shown in Fig. 3b, the friction coefficient between two beads is independent of the sliding speed for tangential speeds above 200 $\mu\mathrm{m.s}^{-1}$, a clear characteristic of solid-like friction (relative speed is changed here through the oscillation amplitude a_0).

4.4.2 Distribution of friction coefficient and normal critical load

We show in Fig. 4.11c and Fig. 4.12 the distribution of friction coefficient and critical normal force obtained over 30 different pairs of beads. As characterized in Fig. 4.11a and Fig. 4.11b, the friction coefficient and critical normal force is a well defined properties of each particle interactions but also depends on the local physicochemical, geometrical, mechanical and roughness surface state of the two sliding beads. We find a mean interparticle friction coefficient $\mu = 0.45 \pm 0.2$, in very good agreement with the macroscopic friction coefficient of PVC on PVC [50].

We find a mean normal critical pressure $F_{\mathrm{N}}^{\mathrm{C}}/\pi R^2 \approx 12 \pm 1$ kPa.

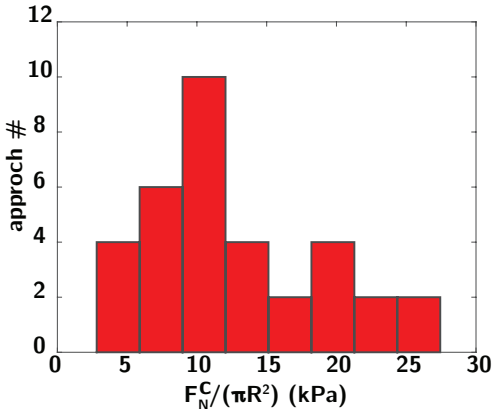

Figure 4.12: Distribution of normal critical pressure for PVC particles in pure Dinch for approaches over ≈ 30 distinct PVC particles.

4.4.3 Ring-down and characterization of non-linearity

To confirm the presence of solid friction in the frictional contact regime at large normal force, we performed additional ring-down experiments, where we monitor the relaxation of the tuning fork with the attached bead sliding on the substrate (see Chapter 1)

At $t = 0$ we switch off the external excitation and monitor the amplitude of the oscillator motion as it relaxes. In absence of solid friction, the envelope of this signal decreases as $a(t)/a_0 = \exp(-t/\tau)$ with $\tau = 2Q/\omega_0$, as shown for the PVC beads in the liquid (Fig. 4.13, blue curve). In presence of solid friction force F_{s}, the envelope of this signal decreases as

$$x(t)/a_0 \approx \exp(-\omega_0 t/2Q)\left[1 + \frac{4F_{\mathrm{s}}Q}{Ka_0\pi}\right] - \frac{4F_{\mathrm{s}}Q}{Ka_0\pi} \tag{4.2}$$

The fact that the relaxation is not purely exponential during contact between the two particles (Fig. 4.13, red curve) confirms the presence of solid friction in the frictional regime (see Fig. 4.11b).

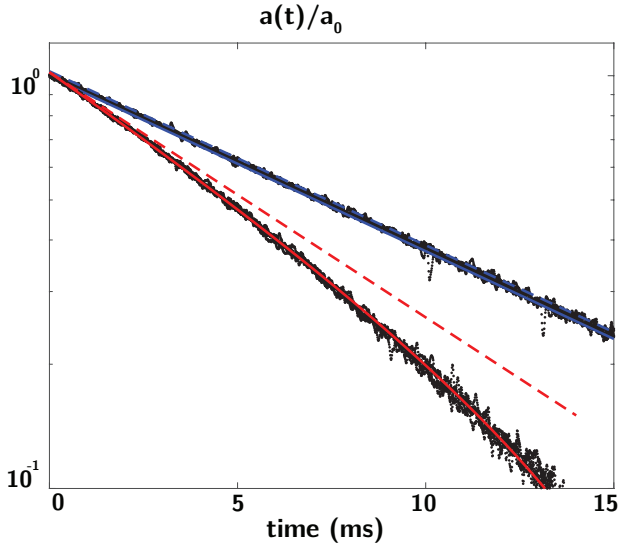

Figure 4.13: **Characterization of the relaxation of the tangential oscillations of the tuning fork ("ring-down")**. Blue lines: relaxation of the PVC bead in liquid. Red lines: relaxation in contact between two PVC beads (normal load of 30 nN and normal force gradient of 17.5 N/m, in Dinch solvent). Plain line are fit of the data through $a(t)/a_0 = \exp(-\omega_0 t/2Q)(1+4F_sQ/Ka_0\pi)-4F_sQ/Ka_0\pi$, and dashed lines represent pure exponential viscous-like relaxation $\exp(-\omega_0 t/2Q)$. Initial oscillation amplitude is $a_0 \approx 60$ nm. Non-exponential relaxation when in contact with the PVC substrate confirms the presence of solid-like sliding friction.

4.4.4 Measurements under moderate and high normal load

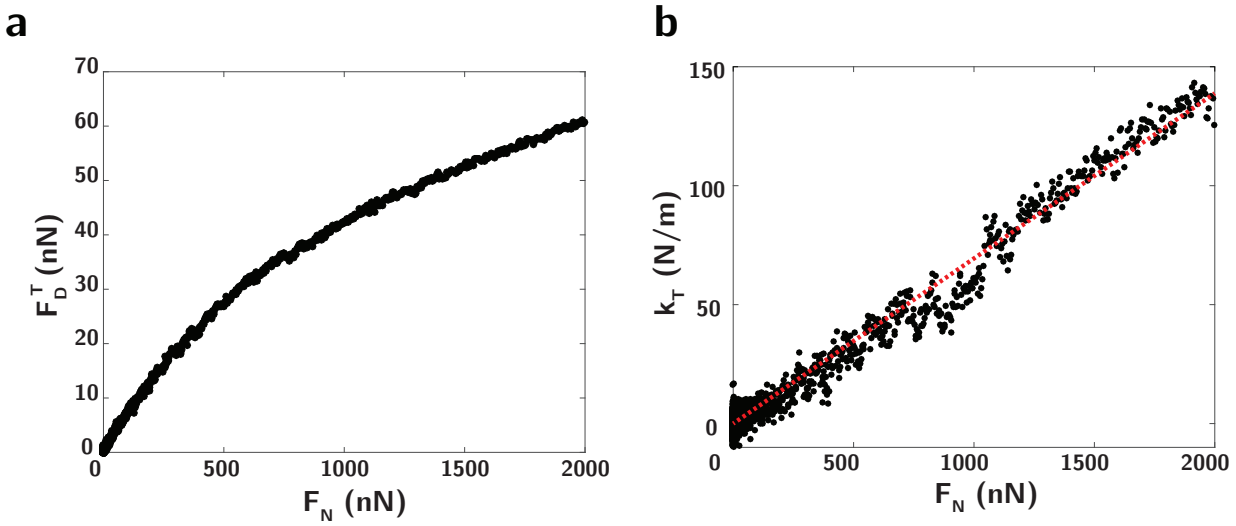

Figure 4.14: **(a)** Tangential friction forces $F_{\mathrm{D}}^{\mathrm{T}}$ versus normal load F_{N}, showing a sublinear variation of friction forces with normal load at large normal loads ($F_{\mathrm{N}} \gg F_{\mathrm{N}}^{\mathrm{C}}$). The radius of the attached bead is 0.5 µm and the solvent between the two beads is pure Dinch. **(b)** Variation of the tangential conservative forces k_{T} as a function of the normal load F_{N}. The linear relation between k_{T} and F_{N} suggests that the real area of contact varies proportionally to the normal load.

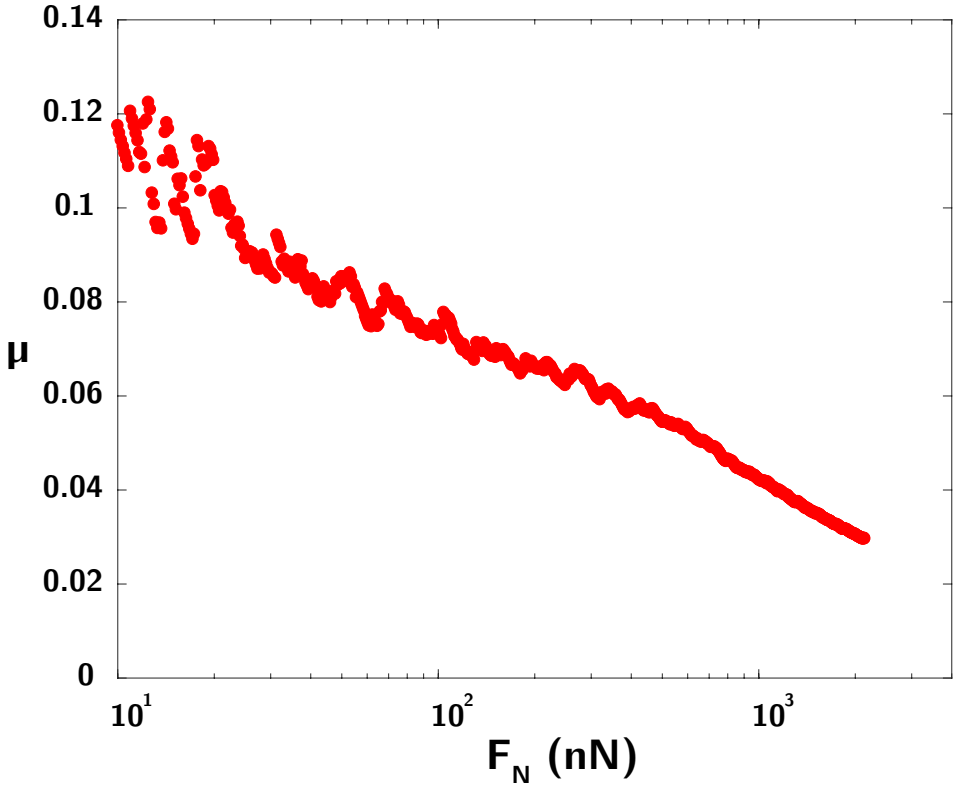

Figure 4.15: Variation of the microscopic interparticle friction coefficient $\mu = F_{\mathrm{D}}^{\mathrm{T}}/F_{\mathrm{N}}$ as a function of the normal load. μ decreases with increasing loads. Note that the particles involved in this measurement are not the same than the one used in Figure 4.11.

We focus now on the behavior at high normal load, for which the particles experience frictional interactions. We plot in Fig. 4.14a tangential dissipative friction forces $F_{\mathrm{D}}^{\mathrm{T}}$ as a function of the normal load F_{N}, for loads up to 2 µN. Whereas in the initial frictional regime uncovered in Fig. 4.11a (ii), friction was found to obey coulomb law, we clearly observe in Fig. 4.14a a sublinear variation of tangential dissipative forces with normal load at larger loads. We can extract from Fig. 4.14a a microscopic friction coefficient defined as $\mu = F_{\mathrm{D}}^{\mathrm{T}}/F_{\mathrm{N}}$, which we plot in Fig. 4.15 as a function of the normal load. μ decreases as a function of the applied load.

To understand this deviation from Coulomb laws, we express the frictional force between the two PVC surfaces as $F_{\mathrm{D}}^{\mathrm{T}} = \tau \cdot \mathcal{A}_{\mathrm{real}}$, where $\mathcal{A}_{\mathrm{real}}$ is the real area of contact, and the shear strength τ [Pa] characterizes friction per real contact area between the PVC surfaces. The deviation from the classical Amontons-Coulomb law at large load i.e.. the non-linear dependence between tangential friction and normal load (Fig. 4.14a) and the decrease in the friction coefficient μ (Fig. 4.15) could stem from (1) a geometrical origin, i.e.. a non-linear variation of the real contact area $\mathcal{A}_{\mathrm{real}}$ with normal load F_{N} (as given for a Hertz contact) or (2) a physical origin, i.e.. a decrease in the shear strength τ [Pa] with normal load. To disentangle between those two effects, we plot in Fig. 4.14b the tangential stiffness k_{T} [N/m] as a function of the normal load. k_{T} can be considered to be directly proportional to the real area of contact $\mathcal{A}_{\mathrm{real}}$ (i.e. to the numbers of contact). This tangential stiffness is found to vary proportionally to the normal load over the entire range of measurements. We thus deduce that the real area of contact increases proportionally with the normal load,

in agreement with classical multi-asperity models. The non-linear variation of tangential dissipation with normal load has thus its origins in a decrease of the shear strength τ with increasing normal loads, and stems from the physical interaction between the two PVC surfaces.

Such decrease of the friction coefficient with load has been reported in the literature for strongly compressed polymer brushes in good solvents [5, 45].

4.5 Results and Discussions: toward a global vision of the rheology of non-Brownian suspensions

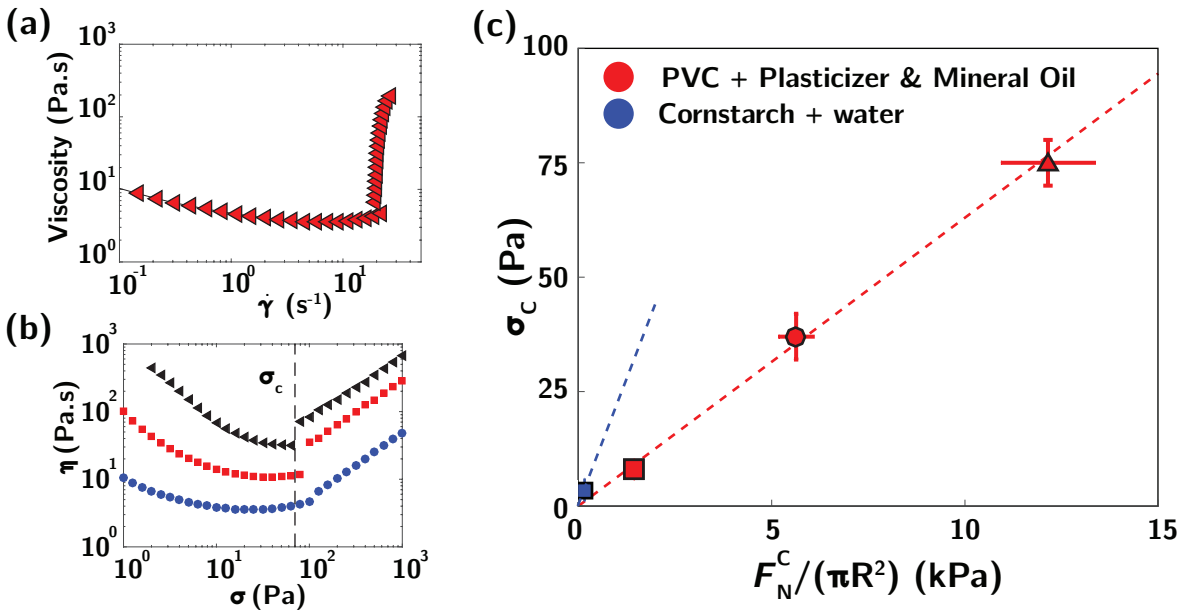

Figure 4.16: **Nanoscale critical load determines macroscale critical shear stress.** **(a)** Shear viscosity as a function of the shear stress for suspensions of PVC in pure Dinch and a volumic solid fraction equal to 60%. **(b)** Flow curves for PVC in pure Dinch, for volumic solid fractions equal to 66%, 64% and 60% (from top to bottom) allowing the characterization of the critical shear stress σ_C. The vertical dashed line corresponds to the critical shear stress $\sigma_C = 75$ Pa ± 5. **(c)** Correlation between the critical normal stress F_N^C and critical shear stress σ_C for PVC in 100% (red triangle), 90% (red circle) and 67% (red square) plasticizer and cornstarch in water (blue square). Horizontal error bars are *s.e.m.* for PVC, with $N > 15$ and standard deviation for Cornstarch ($N = 4$). Red and blue dotted lines are respectively linear fit to the PVC and cornstarch systems.

4.5.1 The shear thickening transition in PVC and Cornstarch

We now come back to the macroscale behavior of non-Brownian suspensions.

As shown in Figs. 4.16a-b and Fig. 4.7, we measured using standard rheometry the flow curves (i.e the relation between the applied shear stress σ and the measured shear rate $\dot{\gamma}$) for various solutions of PVC particles in mixtures of Dinch and mineral oil [55, 56] and cornflour particles in water [16, 39] at various solid fractions. All these suspensions exhibit

a discontinuous shear thickening transition above a critical shear stress σ_C (defined as the critical shear stress above which the viscosity starts to increase as a function of the shear rate [20]). As found previously, σ_C (contrary to the corresponding shear rate $\dot{\gamma}_C$) does not depend upon the solid fraction of particles ϕ [20] for high solid fractions (Fig. 4.16b).

Following recent models, σ_C corresponds to the shear stress required to obtain a particule normal stress high enough to overcome the repulsive forces and to transit from lubricated to frictional contacts [38, 49]. If the shear thickened state is characterized by frictional interactions between the particles, there should be a correlation between the macroscale critical shear stress σ_C and the critical load F_N^C uncovered in Fig. 4.11. To verify this correlation, we measured the microscopic critical load F_N^C for each of the systems of Fig. 4.16a.

We report in Fig. 4.16b the macroscale shear stress σ_C, versus the nanoscale critical force F_N^C for each discontinuous shear thickening systems. For both PVC and cornstarch systems, we see a clear correlation between those two nanometric and macroscopic quantities, with the critical stress at the macroscale varying proportionally to the critical force needed to enter into frictional contact at the nanoscale:

$$\sigma_C = \beta \cdot \frac{F_N^C}{\pi R^2} \tag{4.3}$$

We find here a proportionality coefficient $\beta_{PVC} \approx 0.006$ and $\beta_{Cornstarch} \approx 0.02$, in fair agreement with predictions from simulations performed on smooth particles ($\beta_{simu} \approx 0.05$ for a friction coefficient $\mu = 1$ [38]). Those coefficients characterize stress transmission from the suspension to the particle level and depend on the microscopic friction coefficient [38] for both static and sliding friction, as well as particle shape and roughness. Note that in the simulations, the values of the static and dynamic friction are assumed to be the same, which may not be the case in our situation. Macroscopic roughness may also block the particles and affect the value of β found by numerical simulations.

The good correlation between the macroscopic shear stress σ_C and the nanoscale critical pressure $F_N^C/\pi R^2$ for PVC suspensions shows unambiguously that discontinuous shear thickening transition corresponds to a stress-induced transition from lubricated to frictional contacts between particles.

Let us underline that F_N^C does not depend upon the relative tangential velocities between particles in the range of experimental data. Moreover both F_N^C and σ_C are measured for approximatively the same range of relative velocities between the two particles. In the macroscopic experiments, the relative velocity between two particles can be approximated as $v \approx \dot{\gamma}_C R$ at the onset of the shear thickening transition and varies between 4 μm.s^{-1} and 200 μm.s^{-1}. In the AFM experiments, the normal RMS speed is approximately $30 - 200$ μm.s^{-1} and the tangential RMS speed $150 - 800$ μm.s^{-1}.

4.5.2 Shear thinning at low shear rate in PVC suspensions

We now attempt to describe the first shear-thinning regime occurring in PVC suspensions at low shear rates (Fig. 4.6). In PVC, we checked that this regime cannot be attributed to a competition between diffusion and convection, neither to the non-Newtonian properties of the solvent, neither to migration of particles. Forces measurements between particles prove that the contact between particles are lubricated at low normal load i.e. at low shear rate (Fig. 4.11a).

In this situation, shear thinning may come from the fact that the suspension behaves essentially as soft lubricated particles at low shear stresses, with an apparent size that

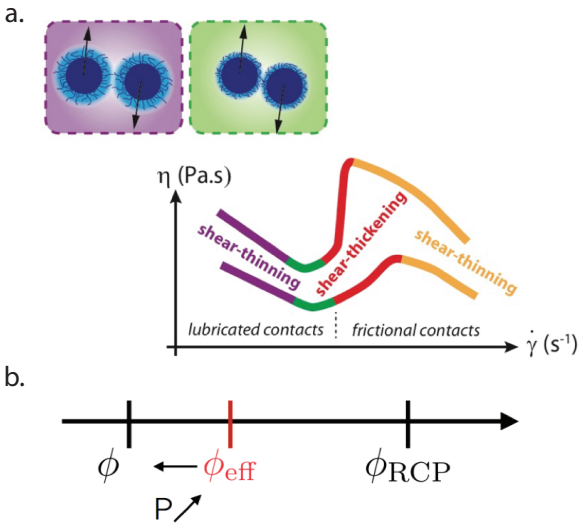

Figure 4.17: **(a)** Scheme of the process involved in the first shear thinning regime: increasing the pressure decreases the effective size of the particles, leading to a decrease of the effective solid fraction ϕ_{eff}. **(b)** The decrease of the effective volume fraction ϕ_{eff} towards the solid fraction for hard spheres ϕ leads to an increase in the distance from the random close packing fraction ϕ_{RCP} at which viscosity diverges for frictionless particles, and thus a decrease of the suspension viscosity.

includes the hard sphere (radius R) and a part of the surrounding soft repulsive potential, which varies as a function of shear rate. If a particle is subjected to a particle pressure P, the minimum gap $2h(P)$ between this particle and its neighbors will be such that $F_{\text{N}}(h) = P\pi R^2$, where F_{N} is the conservative normal repulsive force between the particles. Under this pressure, the apparent radius of the particle will be given by $R + h(P)$. In this regime, the particles have an apparent radius larger than the one of their hard core and this effective radius decreases as a function of the applied pressure i.e. applied shear rate and shear stress. As shown in Fig. 4.17b, the decrease of the effective radius leads to a decrease of the effective solid fraction ϕ_{eff} towards the hard sphere packing fraction ϕ. This decrease in ϕ_{eff} comes with an increase of the distance between ϕ_{eff} and ϕ_{RCP}, the random close packing fraction at which viscosity diverges for frictionless spheres, and thus to a decrease of the suspension viscosity and a shear thinning behavior. Such thinning has been already observed in charge stabilized suspension [30, 37] and predict numerically [38].

To go further and quantitatively analyze our results, we extract the repulsive force profiles from the rheological measurements and we compare them to the data obtained using our Atomic Force Microscope. We start by building upon the analysis of Wyart and Cates for dense suspensions [58]. For the sake of simplicity, we assume as in [58] that the pressure P and the shear stress σ are proportional, and can be expressed as

$$\sigma/\dot{\gamma} = BP/\dot{\gamma} = \eta \tag{4.4}$$

$$\eta = \eta_{\text{s}} \left(\frac{\phi_{\text{RCP}}}{\phi_{\text{RCP}} - \phi_{\text{eff}}} \right)^n \tag{4.5}$$

where n is a fitting parameter, η_{s} is the shear viscosity of the Dinch solvent, ϕ_{eff} is the effective volume fraction and ϕ_{RCP} is the random close packing fraction at which viscosity diverges for frictionless particles (see Fig. 4.17b). B is a constant and does not depend

upon the nature of contact between particles. The effective solid fraction can be related to the apparent minimum possible gap $h(P)$ between particles and to the hard sphere volume fraction ϕ and will be given by:

$$\phi_{\text{eff}} = \phi \left(1 + \frac{h(P)}{R}\right)^3 \tag{4.6}$$

By combining the last two equations, we get the evolution of the interaction potential between the particules $W(h) = PR$ as a function of h [12].

$$h = \left(\left(\frac{\phi_{\text{eff}}}{\phi}\right)^{1/3} - 1\right) \cdot R \tag{4.7}$$

$$\phi_{\text{eff}} = \phi_{\text{RCP}} - \left(\frac{\eta(\dot{\gamma})}{\eta(\dot{\gamma}^*)}\right)^{1/n} (\phi_{\text{RCP}} - \phi) \tag{4.8}$$

$$W(h) = PR = \sigma R/B = W_0(\sigma/\sigma^*) \tag{4.9}$$

In those expressions, $\dot{\gamma}^*$ is the shear rate at the entry of the shear thickening zone, and σ^* is the shear stress associated with the shear thickening transition. At the entry of the shear thickening zone, the particles are close to contact. This leads to $h \approx 0$ and $\phi_{\text{eff}} = \phi$. The pressure at the entry of the shear thickening zone P^* is linked to the potential of interaction at the contact onset W_0 through $P^* = F_{\text{N}}^{\text{C}}/(\pi R^2) = W_0/R$. The knowledge of P^* allows us also to estimate B through $B = \sigma^*/P^*$. The mean value of P^* averaged over 30 measurements is equal $P^* = 6300$ Pa, $\sigma^* = 100$ Pa and $B = 0.016$ for the D1 suspensions and to $P^* = 4200$ Pa, $\sigma^* = 100$ Pa and $B = 0.025$ for the D2 suspension.

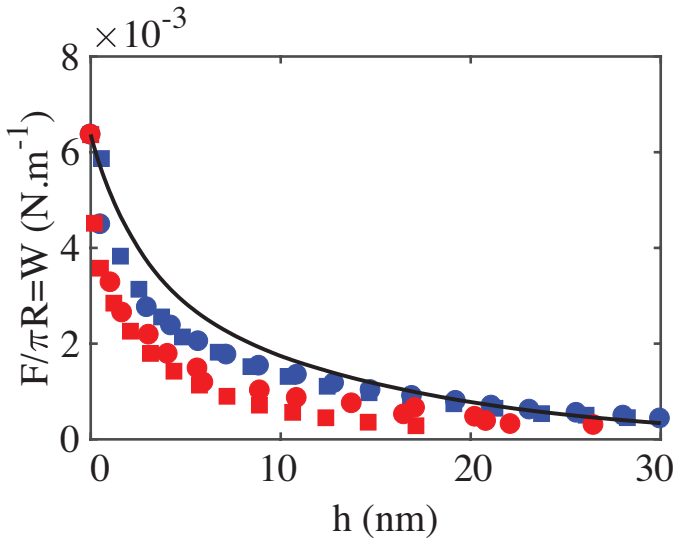

Figure 4.18: Variation of the interaction potential W as a function of h. The black curve corresponds to the value of W for D1 extracted from the AFM experiments (Fig. 4.8). The blue squares correspond to the dispersion D2 ($\phi = 0.64$), the blue circles to the dispersion D2 ($\phi = 0.6$), the red squares to the dispersion D1 ($\phi = 0.6$) and the red circles to the dispersion D1 ($\phi = 0.55$). To compute this curve we use R equal 1 µm for D1 and R equal 1.5 µm for D2.

To find n and ϕ_{RCP}, we measure the value of the viscosity η^* at $\dot{\gamma}^*$ where the viscosity vs shear rate curve goes through a minimum as a function of the solid fraction and fit the

curve using a Krieger-Dougherty model. We get $\phi_{\mathrm{RCP}} = 69.4\% \pm 0.25\%$ for D1 suspensions and $\phi_{\mathrm{RCP}} = 77.2\% \pm 0.25\%$ for D2. The exponents n of the Krieger-Dougherty models are respectively $n = 2.3$ for the D1 dispersion and $n = 2.9$ for the D2 dispersion.

Figure 4.18 displays the values $W(h)$ from equation 4.9 which would lead to the four rheological curves displayed in Fig. 4.6. All the data collapse on a single curve, and is very close to the repulsive profile measured by the AFM, shown as the black line in Fig. 4.18. To compute this curve we use R equal 1 µm for D1 and R equal 1.5 µm for D2. The slight differences between the measurements and the theoretical model may be related to the polydispersity of the samples.

This quantitative analysis shows that the existence of short-ranged repulsive forces along with lubricated contacts at low particular pressure are responsible of the shear thinning behavior observed at low shear rate.

4.5.3 Shear thinning at high shear rate in PVC suspensions

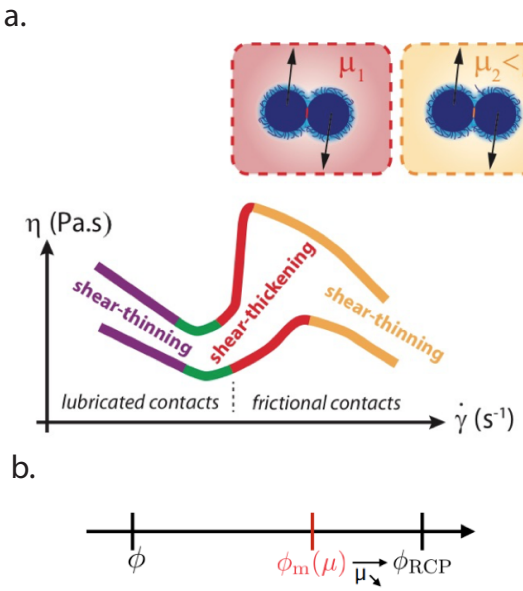

Figure 4.19: **(a)** Scheme of the process involved in the second shear thinning regime: increasing the pressure decreases the value of the microscopic frictional coefficient μ. **(b)** The decrease of the microscopic friction coefficient μ leads to an increase in the critical volume fraction $\phi_{\mathrm{m}}(\mu)$ at which viscosity diverges for frictional sphere towards the random close packing fraction ϕ_{RCP}. The increasing distance between the suspension volume fraction ϕ and $\phi_{\mathrm{m}}(\mu)$ for increasing pressure leads to a decrease in suspension viscosity.

The second shear thinning behavior at large shear rates occurs after the shear thickening transition and thus happens in the context of a frictional rheology (see Fig. 4.19a). To explain this shear thinning behavior we thus turn to our experimental measurements of the friction coefficient between two beads, shown in Figs. 4.14 and 4.15. We pointed out that μ decreases as a function of the normal load, going down from 0.12 to as low as 0.03 for normal forces up to 1 µN. In our experiments the shear stress varies between 10^4 Pa and 10^5 Pa in the shear thinning region. Normal forces are of the order of $10^5 - 5 \cdot 10^5$ Pa with $B = 0.016$ or $B = 0.025$ (Eq. 4.5). Even though local heterogeneities might be

present at the level of the stress field [44], we use a simple argument to estimate the normal load. Assuming that the stress is homogeneous in the sample, the normal force applied on a single bead of radius 1 µm is comprised between 0.3 and 1.5 µN, which corresponds to the range of normal loads for which μ decreases.

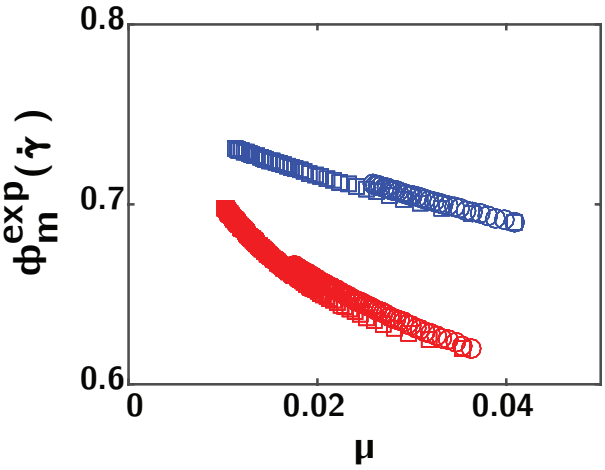

Figure 4.20: Variation of $\phi_{\rm m}^{\rm exp}(\dot{\gamma})$ as a function of μ. The blue squares correspond to the dispersion D2 ($\phi = 0.64$), the blue circles to the dispersion D2 ($\phi = 0.6$), the red squares to the dispersion D1 ($\phi = 0.6$) and the red circles to the dispersion D1 ($\phi = 0.55$).

To go further in our analysis, we follow the model of Wyart and Cates [58]. As shown in Fig. 4.19b, a decrease of μ will increase the value of the friction-dependent jamming density $\phi_{\rm m}$ and thus will increase the distance between the volume fraction ϕ and the critical volume fraction $\phi_{\rm m}$. It is worth noting that $\phi_{\rm m}(\mu)$ is very sensitive to μ in the range $0 - 0.2$ which correspond to the our microscopic friction coefficient variations. At the scale of the suspension, an increase in the shear rate $\dot{\gamma}$ will lead to an increase in the particular pressure and thus a decrease of the value of the interparticle friction coefficient μ. To validate this picture, we correlate the critical volume fraction $\phi_{\rm m}$ with the microscopic friction coefficient μ in the following.

For a frictional rheology, the viscosity of the suspension can be expressed as:

$$\eta = \eta_{\rm s} \left(\frac{\phi_{\rm m}(\dot{\gamma})}{\phi_{\rm m}(\dot{\gamma}) - \phi} \right)^n \tag{4.10}$$

with $\eta_{\rm s}$ the solvent viscosity. Here, we assume that the exponent n of the Krieger-Dougherty model does not depend upon the nature of the contact, and can thus be taken equal to the exponent found for the lubricated rheology at low shear rates (Eq. 4.5). This leads to $\phi_{\rm m}(\dot{\gamma}) = \phi / \left(1 - (\frac{\eta_s}{\eta(\dot{\gamma})})^{1/n}\right)$. The shear rate is given by $\dot{\gamma} = BF_{\rm n}/(\pi R^2 \eta)$. Knowing experimentally the link between μ and $F_{\rm N}$, we display in Fig. 4.20 the evolution of $\phi_{\rm m}(\dot{\gamma})$ as a function of μ. The data obtained by using the rheological measurements displayed on Fig. 4.20 collapse on a single curve for each dispersions revealing the validity of our analysis. The variations of $\phi_{\rm m}(\dot{\gamma})$ required to explain the shear thinning behavior are of the order of 10% when μ varies between 0.08 (close to the entry of the shear thickening zone) and $0.04 - 0.01$ in the shear thinning zone. Such behavior is in agreement with simulations [10].

4.6 Conclusion

In this Chapter, we measured the frictional interaction (normal and tangential force profile) between pairs of particles from non-newtonian PVC and Cornstarch suspensions.

1. **We evidenced a pressure-induced transition from a lubricated regime where pairs of particles can sustain a normal load due to repulsive entropic effects while interacting purely hydrodynamically, to a frictional regime characterized by frictional contacts and sliding (solid-like) friction. Extending our friction measurement to larger load we further evidenced a decrease of the interparticle friction coefficient at large normal pressure.**

2. **We first focus on the discontinuous shear thickening transition occurring in concentrated suspensions of particles. Tuning the physico-chemical properties of the solvent, we vary both the critical load at which this frictional transition takes place, and the macroscopic onset stress at which discontinuous shear thickening occurs. We find a clear correlation between these two stress scales, explaining unambiguously the discontinuous shear thickening transition as stemming from the onset of hard frictional contacts between particles, leading to a transition from a lubricated to a frictional rheology.**

3. **We then extend our analysis to the two shear thinning regimes occurring in non-brownian PVC suspensions. At low shear rate, we show that shear thinning occurs for a lubricated rheology, due to compressibility of the short-range repulsive force profile. The second shear thinning regime at high shear rate occurs after the shear thickening transition, for a frictional rheology. We show that this regime can be rationalized by the decrease of the interparticle friction coefficient at large normal loads.**

References

1. Abdesselam, Y. *et al.* Rheology of plastisol formulations for coating applications. *Polymer Engineering and Science* **57,** 982–988 (2017).

2. Barnes, H. A. Shear-thickening ("Dilatancy") in Suspensions of Nonaggregating Solid Particles Dispersed in Newtonian Liquids. *Journal of Rheology* **33,** 329–366 (Feb. 1989).

3. Barroso, E. G., Duarte, F. M., Couto, M. & Maia, J. M. High strain rate rheological characterization of low viscosity fluids. *Polymer Testing* **29,** 419–424 (June 2010).

4. Bouchet, A.-S., Cazeneuve, C., Baghdadli, N., Luengo, G. S. & Drummond, C. Experimental Study and Modeling of Boundary Lubricant Polyelectrolyte Films. *Macromolecules* **48,** 2244–2253 (2015).
5. Briscoe, B. & Tabor, D. The effect of pressure on the frictional properties of polymers. *Wear* **34,** 29–38 (1975).
6. Brown, E. & Jaeger, H. M. Shear thickening in concentrated suspensions: phenomenology, mechanisms and relations to jamming. *Reports on progress in physics. Physical Society (Great Britain)* **77,** 046602 (2014).
7. Brown, E. & Jaeger, H. M. Dynamic Jamming Point for Shear Thickening Suspensions. *Physical Review Letters* **103,** 086001 (Aug. 2009).
8. Brown, E. & Jaeger, H. M. The role of dilation and confining stresses in shear thickening of dense suspensions. *Journal of Rheology (1978-present)* **56,** 875–923 (July 2012).
9. Clavaud, C., Bérut, A., Metzger, B. & Forterre, Y. Revealing the frictional transition in shear-thickening suspensions. *Proceedings of the National Academy of Sciences* **114,** 5147–5152 (2017).
10. Da Cruz, F., Emam, S., Prochnow, M., Roux, J.-N. & Chevoir, F. Rheophysics of dense granular materials: Discrete simulation of plane shear flows. *Physical Review E* **72,** 021309 (2005).
11. Dai, S.-C., Bertevas, E., Qi, F. & Tanner, R. I. Viscometric functions for noncolloidal sphere suspensions with Newtonian matrices. *Journal of Rheology* **57,** 493–510 (2013).
12. Derjaguin, B. V. Untersuchungen über die Reibung und Adhäsion, IV. *Colloid & Polymer Science* **69,** 155–164 (1934).
13. Einstein, A. On the motion of small particles suspended in liquids at rest required by the molecular-kinetic theory of heat. *Annalen der Physik* **17,** 549–560 (1905).
14. Einstein, A. Berichtigung zu meiner Arbeit:Eine neue Bestimmung der Moleküldimensionen. *Annalen der Physik* **339,** 591–592 (1911).
15. Fall, A. *et al.* Macroscopic Discontinuous Shear Thickening versus Local Shear Jamming in Cornstarch. *Physical Review Letters* **114,** 098301 (Mar. 2015).
16. Fall, A. *et al.* Macroscopic discontinuous shear thickening versus local shear jamming in cornstarch. *Phys. Rev. Lett.* **114,** 098301 (2015).
17. Feiler, A., Larson, I., Jenkins, P. & Attard, P. A quantitative study of interaction forces and friction in aqueous colloidal systems. *Langmuir* **16,** 10269–10277 (2000).
18. Fernandez, N., Cayer-Barrioz, J., Isa, L. & Spencer, N. D. Direct, Robust Technique for the Measurement of Friction between Microspheres. *Langmuir* **31,** 8809–8817 (2015).
19. Goernitz, E. & Zecha, H. Interactions in PVC-plasticizer dispersions. *Langmuir* **3,** 738–741 (1987).
20. Guy, B., Hermes, M. & Poon, W. Towards a unified description of the rheology of hard-particle suspensions. *Phys. Rev. Lett.* **115,** 088304 (2015).
21. Han, E., Peters, I. R. & Jaeger, H. M. High-speed ultrasound imaging in dense suspensions reveals impact-activated solidification due to dynamic shear jamming. en. *Nature Communications* **7,** 12243 (July 2016).

22. Hoffman, R. L. Discontinuous and Dilatant Viscosity Behavior in Concentrated Suspensions. I. Observation of a Flow Instability. *Transactions of The Society of Rheology (1957-1977)* **16,** 155–173 (Mar. 1972).

23. Israelachvili, J. N. *Intermolecular and surface forces: revised third edition* (Academic press, 2011).

24. Jamali, S., Boromand, A., Wagner, N. & Maia, J. Microstructure and rheology of soft to rigid shear-thickening colloidal suspensions. *Journal of Rheology* **59,** 1377–1395 (2015).

25. Kalman, D. P. *Microstructure and rheology of concentrated suspensions of near hard-sphere colloids* PhD thesis (Delaware, 2010).

26. Kalman, D. P., Rosen, B. A. & Wagner, N. J. Effects of Particle Hardness on Shear Thickening Colloidal Suspension Rheology. *AIP Conference Proceedings* **1027,** 1408–1410 (July 2008).

27. Klein, J. Shear, Friction, and Lubrication Forces Between Polymer-Bearing Surfaces. *Annual Review of Materials Science* **26,** 581–612 (1996).

28. Klein, J. Shear of polymer brushes. *Colloids and Surfaces A: Physicochemical and Engineering Aspects* **86,** 63–76 (1994).

29. Klein, J., Kumacheva, E., Perahia, D., Mahalu, D. & Warburg, S. Interfacial sliding of polymer-bearing surfaces. *Faraday Discussions* **98,** 173–188 (1994).

30. Krieger, I. M. Rheology of monodisperse latices. *Advances in Colloid and Interface Science* **3,** 111–136 (1972).

31. Labardi, M. & Allegrini, M. Noncontact friction force microscopy based on quartz tuning fork sensors. *Applied Physics Letters* **89,** 11–14 (2006).

32. Lee, Y., Wetzel, E. & Wagner, N. J. The ballistic impact characteristics of Kevlar® woven fabrics impregnated with a colloidal shear thickening fluid. *J. Mater. Sci.* **38,** 2825–2833 (2003).

33. Leroy, S. *et al.* Hydrodynamic interaction between a spherical particle and an elastic surface: A gentle probe for soft thin films. *Physical Review Letters* **108,** 1–5 (2012).

34. Lim, A. S., Lopatnikov, S. L., Wagner, N. J. & Gillespie, J. W. An experimental investigation into the kinematics of a concentrated hard-sphere colloidal suspension during Hopkinson bar evaluation at high stresses. *Journal of Non-Newtonian Fluid Mechanics* **165,** 1342–1350 (Oct. 2010).

35. Lin, N. *et al.* Hydrodynamic and contact contributions to shear thickening in colloidal suspensions. *Phys. Rev. Lett.* **115,** 228304 (2015).

36. Lombois-Burger, H., Colombet, P., Halary, J. L. & Van Damme, H. On the frictional contribution to the viscosity of cement and silica pastes in the presence of adsorbing and non adsorbing polymers. *Cement and Concrete Research* **38,** 1306–1314 (Nov. 2008).

37. Maranzano, B. J. & Wagner, N. J. The effects of interparticle interactions and particle size on reversible shear thickening: Hard-sphere colloidal dispersions. *Journal of Rheology* **45,** 1205–1222 (2001).

38. Mari, R., Seto, R., Morris, J. F. & Denn, M. M. Shear thickening, frictionless and frictional rheologies in non-Brownian suspensions. *Journal of Rheology* **58,** 1693–1724 (2014).

39. Michiel, H. *et al.* Unsteady flow and particle migration in dense, non-Brownian suspensions. *J. o. R.* **60,** 905–916 (2016).

40. Nakajima, N. & Harrell, E. R. Rheology of poly(vinyl chloride) plastisol for superhigh shear-rate processing. I. en. *Journal of Applied Polymer Science* **115,** 3605–3609 (Mar. 2010).

41. Nakajima, N. & Harrell, E. Rheology of PVC Plastisol at Instability Region and Beyond (Proposal for Super-High Shear-Rate Coating). en. *Journal of Elastomers and Plastics* **41,** 277–285 (May 2009).

42. Peters, I., Majumdar, S. & Jaeger, H. Direct observation of dynamic shear jamming in dense suspensions. *Nature* **532,** 214–217 (2016).

43. Qin, J., Zhang, G. & Shi, X. Study of a shear thickening fluid: the suspensions of monodisperse polystyrene microspheres in polyethylene glycol. *Journal of Dispersion Science and Technology* **38,** 935–942 (2017).

44. Rathee, V., Blair, D. L. & Urbach, J. S. Localized Stress Fluctuations Drive Shear Thickening in Dense Suspensions. *PNAS* **114,** 8740–8745 (2017).

45. Raviv, U., Tadmor, R. & Klein, J. Shear and Frictional Interactions between Adsorbed Polymer Layers in a Good Solvent. *The Journal of Physical Chemistry B* **105,** 8125–8134 (Aug. 2001).

46. Royer, J., Blair, D. & Hudson, S. Rheological Signature of Frictional Interactions in Shear Thickening Suspensions. *Phys. Rev. Lett.* **116,** 188301 (2016).

47. Sader, J. E. & Jarvis, S. P. Accurate formulas for interaction force and energy in frequency modulation force spectroscopy. *Applied Physics Letters* **84,** 1801 (2004).

48. Schorr, P. A., Kwan, T. C., Kilbey, S. M., Shaqfeh, E. S. & Tirrell, M. Shear forces between tethered polymer chains as a function of compression, sliding velocity, and solvent quality. *Macromolecules* **36,** 389–398 (2003).

49. Seto, R., Mari, R., Morris, J. & Denn, M. Discontinuous shear thickening of frictional hard-sphere suspensions. *Phys. Rev. Lett.* **111,** 218301 (2013).

50. Shooter, K. & Tabor, D. The frictional properties of plastics. *Proc. Phys. Soc. Sect. B* **65,** 661 (1952).

51. Van Hecke, M. Soft matter: Running on cornflour. en. *Nature* **487,** 174–175 (July 2012).

52. Vázquez-Quesada, A., Tanner, R. I. & Ellero, M. Shear Thinning of Noncolloidal Suspensions. *Physical review letters* **117,** 108001 (2016).

53. Villey, R. *et al.* Effect of Surface Elasticity on the Rheology of Nanometric Liquids. *Physical Review Letters* **111,** 215701 (2013).

54. Wagner, N. & Brady, J. F. Shear thickening in colloidal dispersions. *Phys. Today* **62,** 27–32 (2009).

55. Willey, S. J., Physics, P. & Branch, E. Solvation Effects on Dilatancy in Concentrated PVC Plastisols. **564,** 557–564 (1982).

56. Willey, S. J. & Macosko, C. Steady shear rheological behavior of PVC plastisols. *J. o. R.* **22,** 525–545 (1978).

57. Wyart, M. & Cates, M. E. Discontinuous shear thickening without inertia in dense non-brownian suspensions. en. *Physical Review Letters* **112** (Mar. 2014).

58. Wyart, M. & Cates, M. Discontinuous shear thickening without inertia in dense non-Brownian suspensions. *Physical review letters* **112,** 098302 (2014).

59. Y.Georget. Mise en oeuvre des plastisols. *Techniques de l'ingénieur* (1994).

Chapter 5

Conclusion and Perspectives

Contents

We evidenced throughout this thesis that the mechanical properties of materials at the nanoscale can be dramatically affected by external drivings such as confinement, shear or pressure.

The investigation of those questions has been allowed by the development of a quartz-tuning fork based Atomic Force Microscope, which we introduced in the first Chapter. This instrument has been traditionally used in hard condensed matter for exquisite imaging and force sensing at the atomic scale. We have shown throughout this thesis that it can be successfully applied to probe the mechanical response of soft matter systems.

In particular, via the use of frequency-modulation AFM techniques, the quartz-tuning fork based AFM can be fruitfully used as a nanorheometer, allowing quantitative measurement of conservative and dissipative mechanical impedance of nanoscale soft matter systems, and unprecedented characterization of friction and dissipation at those scales. Interestingly, those quantitative measurements allow for a complete characterization of the viscoelastic properties (solid-like and liquid-like) of confined nanoscale materials.

We present in this last chapter the conclusions and perspectives associated with the investigations presented in this thesis. We then present on-going work and perspectives on two questions related to reactive lubrications, which have been addressed in the last year of this PhD, along with two other PhD students, Luca Canale and Antoine Lainé.

5.1 General Conclusion and Perspectives

5.1.1 Nanoscale Capillary Freezing in Ionic Liquids

In the second Chapter of this thesis, we focused on the rheological behavior of ionic liquids confined at the nanoscale. Confining ionic liquids between micron-size AFM tungsten tips and substrates of various nature, we evidenced a dramatic change in the mechanical properties of the ionic liquid, with the appearance of a solid-like response for confinements of tens of nanometer. This abrupt change in the rheology was interpreted as a signature of a bulk confinement induced freezing transition for the ionic liquid, with an elevation of the melting temperature due to the predominance of surface energies in nano confinement (Gibbs-Thompson effect). This response was found to be strongly dependent on the electronic properties of the confining materials, with more conductive materials facilitating the freezing transition. This experimental observation was rationalized by considering the influence of metallic boundaries on the relative wetting properties of ionic liquid and solid phases. Additionally, using AFM tips with small radii of curvature, we could also evidence the presence of pre-wetting solid-like structures preexisting on the substrates independently of any confinements, but with smaller heights than the observed confinement lengths. Finally, the freezing transition could be reversibly tuned through the application of an additional bias voltage between the confining interfaces, giving strong support to the interpretation of the observed change in mechanical impedance as of a bulk freezing transition.

Similar investigation on the behavior of ionic liquids confined at dielectric and metallic interfaces were recently carried out in the group of Elisabeth Charlaix using a dynamic Surface Force Apparatus [8]. They obtained qualitatively similar results, with a strong dependence of the rheological properties of the ionic liquid on the metallic character of the confining interfaces (comparing metallic platinum coated surfaces with dielectric insulating glass surfaces). Interestingly, they interpreted there rheological measurements on metallic platinum surfaces as evidencing a soft solid-like phase of complex frequency response preexisting to any confinement, and not with a bulk confinement induced freezing transition.

Those independent observations, along with their similarities (strong effect of substrate metallicity on the ionic liquid rheology) and distinctions (bulk confinement induced freezing transition versus surface effects), open broad perspectives by showing that the electronic properties (condensed matter properties) of materials can have a profound effect on the mechanical behavior of soft materials, through subtle electrostatic effects. More specifically, the question of the effect of probe size on the kinetics and metastability of the freezing transition (colloidal micrometric scale in our case, millimetric scale in the experiments of Garcia et al. [8]), as well as the role of solicitation frequency on the mechanical properties of the ionic liquid and solid phases should be addressed in future studies.

Our results have broader implications related to the dynamics of dense electrolytes in porous matrices [27, 31], which are crucial in the context of supercapacitors dynamics [21]. Other exotic behaviors might emerge for confinements of the order of the ion size [7] while the presence of disordered and rough surfaces, as typically present in supercapacitors might prevent the freezing transition reported here [13, 14]. Further experimental and theoretical investigations of these regimes seem now to be necessary in light of our study.

In the context of lubrication, our results also suggest to take advantage of the dramatic and abrupt ionic liquid phase change to tune nanoscale friction via modifications of the

substrate, from insulating to metallic, and possibly with dedicated patterning via metallic coating. The relatively weak solid phase would indeed prevent undesired direct substrate-substrate contact by generating normal forces. The solid phase could be regenerated in situ, as it takes its origin in the ionic liquid confinement. Furthermore, the modification of the confinement-induced transition under a voltage drop could finely modify the lubricating state by active polarization. While such perspectives require further exploration, they open new and exciting perspectives for phase-changing lubricants, and are developed further in the second part of this perspective Chapter.

5.1.2 Molecular Rheology of Gold Nanojunctions

Shear is another driving which can be used to actively tune the mechanical properties of nanoscale objects. In the third Chapter of this thesis, we focused on the mechanical response of necks of few gold atoms. The molecular size of those systems leads to quantized electronic transport, allowing to measure and control their lateral dimension with atomic-scale precision. By submitting the junction to increasing subnanometric deformations, we uncovered a transition from a purely elastic regime to a plastic flow regime, up to the complete shear-induced melting or fluidization of the junction. Our measurements allowed us to measure the critical yield force governing the onset of plastic flow in the junction, as a function of lateral size. The yield stress, characterizing the onset of plasticity, is found to be approximately independent of lateral junction size, suggesting that in those molecular systems, plastic flow is limited by the sliding of atomic planes under shear, as expected for dislocation starved systems. We then analyzed the dissipative behavior of the junction, which is found to be well characterized by a hydrodynamic friction law, with dissipation directly proportional to the shear rate and the junction cross-sectional area. We thus extracted a characteristic viscosity and hydrodynamic stress for the junction under shear. We found a hydrodynamic stress of the same order as the plastic yield stress, suggesting that the observed hydrodynamic behavior is intrinsically related to the shearing motion of the tuning fork. Interestingly, a liquid-like behavior was also recovered in the conservative force response at large strain, in the form of an attractive adhesive force. This adhesive behavior at large oscillation amplitude is interpreted as the complete shear-induced melting of the gold junction, leading to the appearance of adhesive capillary effects. We rationalized part of our results by considering the dynamics of a harmonically driven Prandtl-Tomlinson model.

Our study extends viscoelastic rheological measurements, traditionally used to characterize the response of macroscopic soft matter systems such as foams [29] and emulsions [19] to a metallic system of molecular size. Those results could find useful applications in the context of ultrasonic [4] and cold welding [3, 18], where one might expect injection of ultrasounds and mechanical energy to locally liquefy the interfaces and participate in the welding process. Reversibly, the question of shape stability of nanoscale components is critical, for example in the context of nano electronics [17, 28], where liquid-like behavior or surface tension driven reorganization should instead be prevented.

On a more fundamental perspective, we evidenced a viscous-like dissipative behavior for the gold neck under shear, distinct from static frictional forces given by standard plasticity models. Further theoretical work and simulations could help to identify the fundamental dissipation channels in such nanoscale assemblies. The study of the origin and rate dependence of dissipative processes in nanoscale systems is critical in the context of nanomechanical resonators [6, 11].

The correlation between the lateral system size and the yield force should also break down above a characteristic sample size, above which one should recover defect-mediated plastic behavior. A proper investigation of this limit, and of the associated dissipative regimes would be very interesting to probe experimentally.

Finally, an important perspective lies in the context of macroscopic sliding friction, in which interfaces are composed of a number of micro and nano metric contacts, which can flow and deform plastically under shear. The plastic behavior of those nanocontacts under shear and their role in macroscopic static and dynamic friction and adhesion [1, 20, 22, 23, 33] could be disentangled through joint studies of macroscopic interfacial friction and single contact rheology.

5.1.3 Non Newtonian Rheology of Suspensions

In the fourth Chapter, we measured the local frictional profile between pairs of particles from a macroscopic suspension (pairs of PVC and cornstarch particles in various solvents), and related those measurements to the macroscopic behavior of the suspension. We evidenced a pressure-induced transition at the nanoscale between a lubricated regime, where pairs of particles support a finite normal load, while interacting purely hydrodynamically, and a frictional regime characterized by hard repulsive contacts between particles and sliding friction. Tuning the physicochemical properties of the suspending fluid, we showed that the normal pressure needed to enter the frictional regime at nanoscale matches the critical stress at which shear thickening occurs for macroscopic suspensions. This demonstrates that the shear thickening transition observed at the scale of the suspension takes its origin in this nanoscale frictional transition, and corresponds to a stress-induced transition between a low viscosity and high viscosity branch. Further measurements allowed us to rationalize the two shear thinning regimes observed in PVC suspensions before and after the shear thickening transition. We interpreted the first shear thinning regime observed at low shear rates as occurring for a lubricated rheology, due to compressibility effect of the soft repulsive potential. The second shear thinning regime observed for large shear rates after the shear-thickening transition occurs for a frictional rheology, and can be interpreted as stemming from a decrease of the interparticle friction coefficient at large normal load.

Our experiments bridge nano and macro scales and provide long needed demonstration of the role of microscopic local interactions in the rheology of suspensions. In this context, further measurements could allow to rationalize the drastically different behavior of cornstarch and PVC suspensions in the shear-thickened state. Whereas PVC suspensions seem to behave as "ideal" shear-thickening fluids, with homogeneous flow and a well-defined frictional rheology in the shear-thickened state, cornstarch suspensions show migration, phase separation and important density fluctuations in the shear thickened state, reminiscent of the behavior of a yield stress fluid. These distinct behaviors could be due to the large nanoscale adhesion measured between cornstarch grains. Similarly, additional correlations, for example between microscopic friction coefficients and macroscopic jamming packing fractions for frictional suspensions could be tested following similar joint nanometric and macroscopic approaches.

More generally, our measurements open broad perspectives by showing the crucial importance of detailed local interactions in the understanding of the global behavior of soft matter systems and assemblies. It could be extremely interesting to extend those joint macroscopic and nanometric measurements to other soft matter systems such as colloidal gels, granular materials, etc..

5.1.4 Instrumental Perspectives

Using frequency-modulation AFM techniques, we could measure the dissipative frictional response of various nanoscale systems as a function of shear rate via a change of the oscillation amplitude at a fixed oscillation frequency. This technique gave very satisfactory results. However, in some cases, it might be interesting to be able to probe the response of the system at various driving frequencies for a fixed oscillation amplitude (e.g. in the context of gold).

One difficulty associated with such multifrequency measurements is that one loses the large response of the oscillator close to the resonance frequency. However, such multifrequency measurements are possible for example via novel state of the art techniques such as Force Feedback Microscopy techniques [26, 32] or high-speed AFM techniques [25].

5.2 On-Going Perspectives on Reactive Lubrication

We evidenced in this thesis the occurrence of dramatic changes in the mechanical properties of materials at the nanoscale, either due to confinement induced phase transitions in ionic liquids, or due to the application of external shear in the context of nanoscale gold junctions. Moreover, as shown in the context of the non-newtonian rheology of suspensions, the properties of materials at the nanoscale can have profound impacts on their macroscale behavior.

Interestingly, this relation between nanoscale interfacial properties and the macroscale behavior is particularly exacerbated in the context of friction, for which strong confinements, and shear localization at the interface can induce changes in mechanical properties of the sliding interface, which in turn can have profound impacts on the macroscopic lubricating behavior.

I started to address those perspectives related to the context of *phase changing lubricants*, over the course of the last year of this PhD, in collaboration with two other PhD students of the team, L. Canale and A. Lainé.

5.2.1 The Tuning Fork based dynamic Surface Force Apparatus

The study of those new perspectives bridging macroscale friction and nanoscale interfacial behavior were allowed by the use of a tuning fork based dynamic Surface Force Apparatus (dSFA), recently developed in the group.

In essence, the tuning fork based dynamic Surface Force Apparatus (Fig. 5.1) is a macroscopic version of the quartz-tuning fork based AFM. Due to its centimetric size and large mass, this macroscopic tuning fork can support centimetric glass beads, as in standard SFA, while maintaining good quality factor allowing to take advantage of frequency-modulation techniques. This dynamic SFA can be used to measure macroscopic friction, while simultaneously informing on the local nanoscale mechanical properties of the sliding interfaces.

The core of the microscope is a centimeter-sized tuning fork made of aluminum. Due to the large mass of the tuning fork, macroscopic probes can be attached to the aluminum prongs while maintaining good quality factors for antisymmetric resonances (Table 5.1). In the context of rheological studies, millimetric glass spheres can be used as the confining probes. The oscillations of the tuning fork are measured using an accelerometer directly glued at the extremity of one prong. Symmetric oscillations of the macroscopic tuning fork

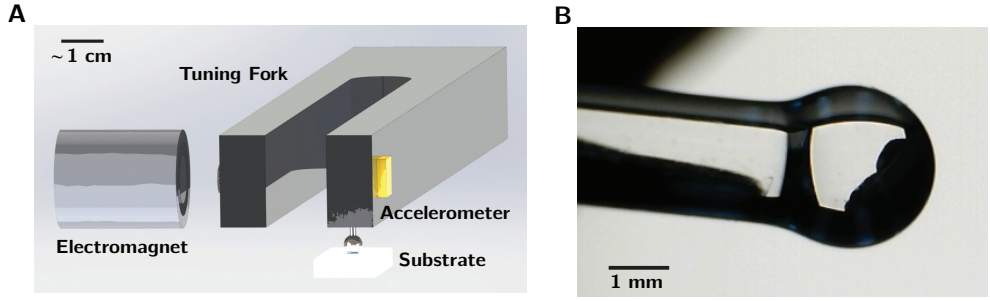

Figure 5.1: **(A)** Schematic of the tuning fork based dynamic Surface Force Apparatus. **(B)** Photograph of a spherical glass probe, melted out of a 2 mm glass rod, leading to smooth glass surfaces.

are excited mechanically, using a piezo dither glued to the tuning fork or electromagnets, and allow to tune the oscillation amplitude over orders of magnitude, from 1 nm up to 10 µm.

In this configuration, this tuning fork can be thought of as a dynamic Surface Force Apparatus [9, 24], allowing to obtain the dissipative and conservative response of confined soft matter systems using similar frequency-modulation techniques as described in Chapter 1.

Importantly, we can take advantage of the two principal resonant frequencies of the tuning fork, to measure normal and tangential dynamic impedance, as described in Chapter 4.

The sensitivity of the tuning fork based dynamic Surface Force Apparatus is reduced compared to the quartz version, mainly due to the larger stiffness K, but this loss in sensitivity is compensated by the increase of several orders of magnitude of the radius of curvature of the confining probes.

Parameter	Normal Mode	Tangential Mode
Resonnant Frequency f_0	$\approx$ 900 Hz	$\approx$ 500 Hz
Equivalent Stiffness K	890 kN.m^{-1}	300 kN.m^{-1}
Typical Quality Factor in air	300	2000
Oscillation Amplitude	1 nm – 100 nm	1 nm – 10 µm

Table 5.1: Parameters for the two oscillatory modes of the tuning fork based dynamic Surface Force Apparatus.

We now present briefly two perspectives related to reactive lubrication using the tuning fork based dynamic Surface Force Apparatus

5.2.2 Reactive Lubrication in Skiing

Friction coefficient of most materials on ice and snow are usually extremely small, with values typically as low as $\mu \sim 0.01 - 0.03$ depending on the conditions [2, 5, 12]. This is at least one order of magnitude smaller than what is observed with dry friction involving other materials (typically $\mu \sim 0.3$). The low ice friction behavior is explained by the presence of a liquid layer between the solid and the ice. It is now an accepted idea that its origin resides in frictional melting: frictional dissipation generates heat which rises the temperature at the contact region, induces melting and lubricates contact. However, no evidence for the

presence of a water film during sliding and no measurements of film thickness have been obtained so far.

In collaboration with L. Canale, we used the tuning fork based dynamic Surface Force Apparatus to evidence the presence of this interfacial water film during sliding. As shown in Fig. 5.2, we use the tangential oscillation mode of the tuning fork to *induce* frictional melting, and the normal oscillation mode as a *probe* to measure the resulting film thickness. Accordingly, we drive the tangential mode to amplitudes ranging from 1 µm to 50 µm, corresponding to velocities in the range of $0.01 - 0.1$ m.s^{-1}. Normal oscillation amplitude is kept to values of the order of 50 nm.

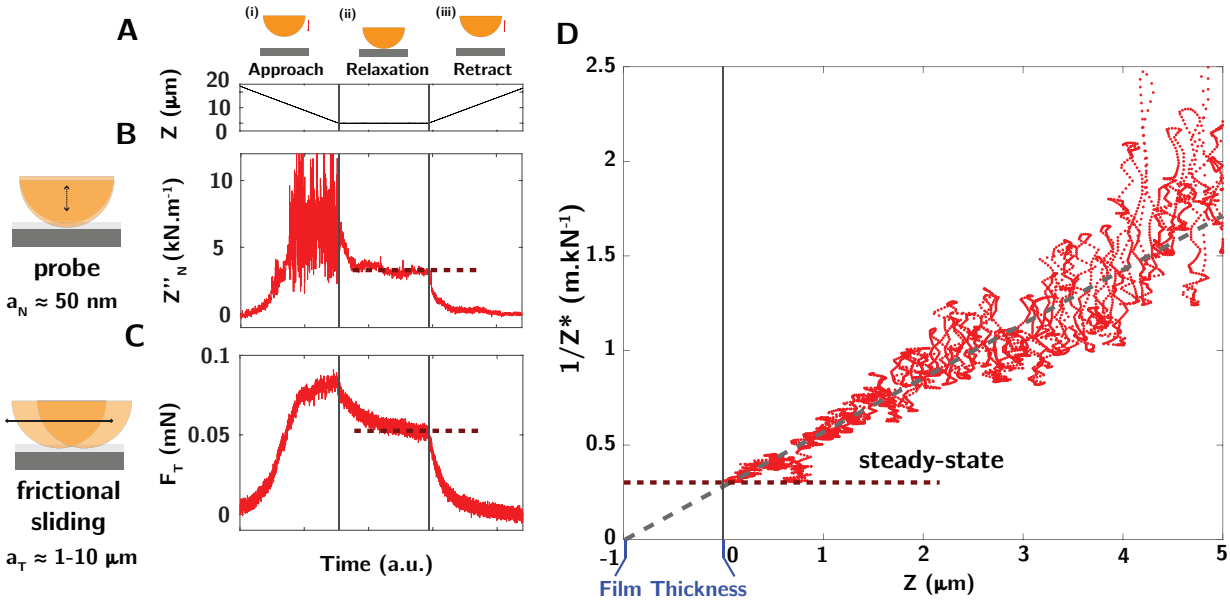

Figure 5.2: **(A-C)** Typical approach curves, consisting of three phases of approach, relaxation and retract (**A**). Variation of the normal dissipative modulus Z''_{N}, **(B)** and tangential frictional force F_{T} **(C)**. Both Z''_{N} and F_{T} relax to a steady state value characterizing an equilibrium condition (red horizontal dotted line). **(D)** Variation of $1/Z''_{\mathrm{N}}$ (red) during retraction, as a function of retraction distance Z. The horizontal dotted line indicated the steady state value for Z''_{N}, identified in (B).

Fig. 5.2A shows the typical procedure when approaching the surface of ice. We first approach the probe in contact to the ice surface (Fig. 5.2A, (i)), leading to the increase in tangential frictional force F_{T} (Fig. 5.2C) and in normal dissipative modulus Z''_{N} (Fig. 5.2B). The approach is then stopped, leading to relaxation towards a steady state equilibrium (Fig. 5.2A, (ii)). Upon retract, the tangential friction and normal impedance relax smoothly to zero (Fig. 5.2A, (iii)). We plot in Fig. 5.2D the variation of the inverse of normal dissipative modulus, which varies linearly with distance for sufficient confinement. This linear variation points to a liquid-like behavior of the confining interface, characterized by a dissipative impedance varying as $Z'' = 6\pi\eta R^2\omega/D$, with η the viscosity, R the probe radius, ω the normal oscillation frequency and D the confining distance. The linear extrapolation of the inverse dissipative modulus crosses the horizontal axis at a well-defined point, which characterizes the thickness of the interfacial water film developing during frictional sliding.

The tuning fork based dynamic Surface Force Apparatus can thus be used to measure the thickness and the interfacial properties of the confined water film forming during frictional sliding. We measure a viscosity for the water film of the order of $\eta \approx 20$ mPa.s.

Interestingly, the measured film thickness varies between 100 nm and 1 µm, corresponding to values much smaller than what were previously predicted. We now plan to carry out a systematic investigation of the parameters influencing the thickness and properties of this interfacial film. Especially interesting would be to probe the effect of the sliding velocity, temperature as well as properties of the sliding materials, in terms of heat conductivity and hydrophobicity.

5.2.3 Reactive Lubrication in Ionic Liquids

As discussed at the beginning of this Chapter, the confinement-induced freezing transition of ionic liquids evidenced in the second Chapter could also be particularly interesting in the context of reactive lubrication and protection against wear. One could indeed imagine to take advantage of the change in the ionic liquid phase to prevent undesired direct substrate-substrate contact by generating normal forces between the sliding surfaces. One might expect a yield stress for this weak ionic solid phase, beyond which it will start to flow. This phase could be potentially regenerated in situ, presenting potentially novel self-healing properties.

We show in Fig. 5.3 preliminary results obtained with A. Lainé for the macroscale rheology and frictional properties of confined ionic liquids using the tuning fork based dynamic SFA. Fig. 5.3 shows an approach curve in the ionic liquid BmimBF4 confined between a smooth pyrex sphere and an intrinsic (undopped) silicon substrate, showing measurements of both normal dissipative and conservative impedance (Fig. 5.3A), and tangential frictional forces (Fig. 5.3B).

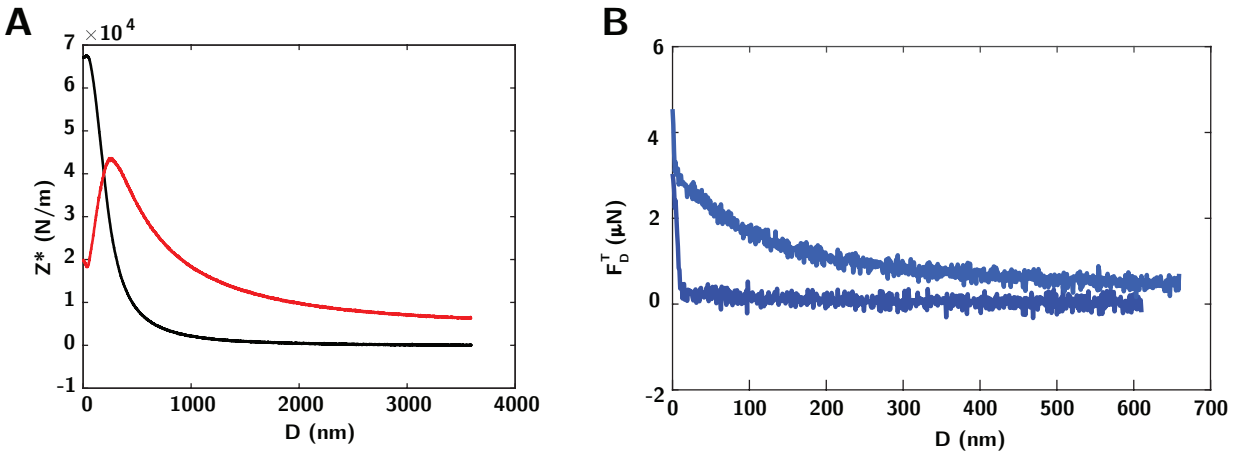

Figure 5.3: Approach curve for BmimBF4 confined between a smooth pyrex sphere and an intrinsic silicon substrate. **(A)** Normal impedance (Z' in black and Z'' in red) **(B)** Tangential frictional force at 2.5 nm and 25 nm amplitude.

The normal impedance response shown in Fig. 5.3A is reminiscent of elasto-hydrodynamic measurements obtained using dynamic SFA [15, 16, 30]. The frictional profile in Fig. 5.3B is well characterized by an initial hydrodynamic logarithmic increase of the tangential dissipation as D decreases with $F_{\mathrm{D}}^{\mathrm{T}} \sim \eta v_{\mathrm{T}} R \ln\left(\frac{R}{D}\right)$ [10], followed by hard contact.

Those preliminary measurements validate the use of the tuning fork based dynamic SFA as a valuable tool for friction measurements in ionic liquids and test further the effects of shear rate and substrate metallicity on ionic liquids rheology in the context of friction studies.

Bibliography

1. Bayart, E., Svetlizky, I. & Fineberg, J. Slippery but Tough: The Rapid Fracture of Lubricated Frictional Interfaces. *Physical Review Letters* **116,** 1–5 (2016).
2. Bowden, F. P. & Hughes, T. P. The Mechanism of Sliding on Ice and Snow. *Proceedings of the Royal Society A: Mathematical, Physical and Engineering Sciences* **172,** 280–298 (1939).
3. Cha, S.-H. *et al.* Cold welding of gold nanoparticles on mica substrate: Self-adjustment and enhanced diffusion. *Scientific Reports* **6,** 32951 (2016).
4. Chen, C., Yan, L., Kong, E. S.-W. & Zhang, Y. Ultrasonic nanowelding of carbon nanotubes to metal electrodes. *Nanotechnology* **17,** 2192–2197 (2006).
5. Colbeck, S. C. The kinetic friction of snow. *Journal of Glaciology* **34,** 78–86 (1988).
6. Eichler, a. *et al.* Nonlinear damping in mechanical resonators made from carbon nanotubes and graphene. *Nature nanotechnology* **6,** 339–342 (2011).
7. Futamura, R. *et al.* Partial breaking of the Coulombic ordering of ionic liquids confined in carbon nanopores. *Nature Materials* **16,** 1225–1232 (2017).
8. Garcia, L., Jacquot, L., Charlaix, E. & Cross, B. Nano-mechanics of ionic liquids at dielectric and metallic interfaces. *Faraday Discuss.* (2017).
9. Garcia, L. *et al.* A micro-nano-rheometer for the mechanics of soft matter at interfaces. *Review of Scientific Instruments* **87** (2016).
10. Goldman, A., Cox, R. & Brenner, H. Slow viscous motion of a sphere parallel to a plane wall - II Couette flow. *Chemical Engineering Science* **22,** 653–660 (1967).
11. Güttinger, J. *et al.* Energy-dependent path of dissipation in nanomechanical resonators. *Nature Nanotechnology* **12,** 631–636 (2017).
12. Kietzig, A. M., Hatzikiriakos, S. G. & Englezos, P. Physics of ice friction. *Journal of Applied Physics* **107** (2010).
13. Kondrat, S. & Kornyshev, A. Superionic state in double-layer capacitors with nanoporous electrodes. *Journal of Physics Condensed Matter* **23** (2011).
14. Kondrat, S., Wu, P., Qiao, R. & Kornyshev, A. A. Accelerating charging dynamics in subnanometre pores. *Nature Materials* **13,** 387–393 (2014).
15. Leroy, S. & Charlaix, E. Hydrodynamic interactions for the measurement of thin film elastic properties. *Journal of Fluid Mechanics* **674,** 389–407 (2011).
16. Leroy, S. *et al.* Hydrodynamic interaction between a spherical particle and an elastic surface: A gentle probe for soft thin films. *Physical Review Letters* **108,** 1–5 (2012).
17. Lu, W. & Lieber, C. M. Nanoelectronics from the bottom up. *Nature Materials* **6,** 841–850 (2007).
18. Lu, Y., Huang, J. Y., Wang, C., Sun, S. & Lou, J. Cold welding of ultrathin gold nanowires. *Nature Nanotechnology* **5,** 218–224 (2010).
19. Mason, T., Bibette, J. & Weitz, D. Yielding and Flow of Monodisperse Emulsions. *Journal of Colloid and Interface Science* **179,** 439–448 (1996).
20. Mate, C. M. *Tribology on the Small Scale: A Bottom Up Approach to Friction, Lubrication, and Wear* 1–354. ISBN: 9780191712098 (2008).

21. Merlet, C. *et al.* On the molecular origin of supercapacitance in nanoporous carbon electrodes. *Nature materials* **11,** 306–310 (2012).

22. Müser, M. H. *et al.* Meeting the Contact-Mechanics Challenge. *Tribology Letters* **65** (2017).

23. Persson, B. N., Albohr, O., Tartaglino, U., Volokitin, A. I. & Tosatti, E. On the nature of surface roughness with application to contact mechanics, sealing, rubber friction and adhesion. *Journal of Physics Condensed Matter* **17,** 1–62 (2005).

24. Restagno, F., Crassous, J., Charlaix, É., Cottin-Bizonne, C. & Monchanin, M. A new surface forces apparatus for nanorheology. *Review of Scientific Instruments* **73,** 2292 (2002).

25. Rigato, A., Miyagi, A., Scheuring, S. & Rico, F. High-frequency microrheology reveals cytoskeleton dynamics in living cells. *Nature Physics* **13,** 771–775 (2017).

26. Rodrigues, M. S., Costa, L., Chevrier, J. & Comin, F. Why do atomic force microscopy force curves still exhibit jump to contact? *Applied Physics Letters* **101,** 203105 (2012).

27. Singh, M. P., Singh, R. K. & Chandra, S. Ionic liquids confined in porous matrices: Physicochemical properties and applications. *Progress in Materials Science* **64,** 73–120 (2014).

28. Sun, J. *et al.* Liquid-like pseudoelasticity of sub-10-nm crystalline silver particles. *Nature materials* **13,** 1007–12 (2014).

29. Van Vliet, K. J., Tsikata, S. & Suresh, S. Model experiments for direct visualization of grain boundary deformation in nanocrystalline metals. *Applied Physics Letters* **83,** 1441–1443 (2003).

30. Villey, R. *et al.* Effect of Surface Elasticity on the Rheology of Nanometric Liquids. *Physical Review Letters* **111,** 215701 (2013).

31. Vioux, A. & Coasne, B. From Ionogels to Biredox Ionic Liquids: Some Emerging Opportunities for Electrochemical Energy Storage and Conversion Devices. *Advanced Energy Materials* **7,** 1–13 (2017).

32. Vitorino, M. V., Carpentier, S., Costa, L. & Rodrigues, M. S. Force feedback microscopy based on an optical beam deflection scheme. *Applied Physics Letters* **105** (2014).

33. Weber, B. *et al.* Molecular probes reveal deviations from Amontons' law in multi-asperity frictional contacts. *Nature Communications* **9,** 1–7 (2018).

Appendix A

Theoretical model: Interfacial energies with Thomas–Fermi boundary

Contents

We consider in this Appendix the energetics of an ionic system interacting with an imperfect conductor. The electronic screening inside the conductor is described by the Thomas-Fermi (TF) theory, defined in terms of the screening length $\ell_{\mathrm{TF}} = k_{\mathrm{TF}}^{-1}$. The finite screening length is due to the energy cost for localizing electrons under external charges [4].

The objective of this part is to obtain an estimate of the surface energies of the crystal-metal and liquid-metal interfaces, and predict its behavior as a function of the metallicity of the metal, introduced here with the TF screening parameter. We first introduce a 1D simplified model, which gives many insights into the dominant contributions to surface energies, and then extend our conclusions to a general ion-metal interface.

A.1 Surface energy of a crystal with a TF wall

We first start our consideration with the ideal case of a perfect 1D crystal in contact with a TF wall. Negative and positive point charges are distributed in an alternating fashion giving the charge density as

$$\rho_{\mathrm{cr}}(z,R) = Q \sum_{n=0}^{\infty} (-1)^n \frac{\delta(z-(na+h))\delta(R)}{2\pi R} \,, \tag{A.1}$$

where we used the representation of δ-function in cylindrical coordinates, corresponding to the axial symmetry of the problem. The lattice constant is a and the crystal is at the distance h from the boundary. This allows us to gives the results in terms of two dimensionless variables $k_{\mathrm{TF}}a$ and h/a. In the following we assume to simplify that $h = a/2$.

We also assume to simplify that the dielectric constant of the crystal background and of the metal are both equal to ϵ (an hypothesis that can be easily relaxed).

In the TF model, the screening parameter $k_{\rm TF} = 1/\ell_{\rm TF}$ allows to interpolate smoothly between the insulating case, with $\ell_{\rm TF} = \infty$, and the perfect metal case, with $\ell_{\rm TF} = 0$. In both limits the electrostatic energy can be readily calculated [1]. The corresponding surface energy reduces to $\gamma^{\rm ins} = Q^2/8\pi\epsilon a$ for the insulating wall, and to $\gamma^{\rm metal} = Q^2/16\pi\epsilon a$ for the perfect metal wall (both in 1D). This points already to the fact that the metallicity of the wall reduces the surface energy by a factor $\delta\gamma = -Q^2/16\pi\epsilon a$. The case of TF substrates will interpolate between these two limiting cases.

As we demonstrate below, the surface tension between a perfect semi-infinite ionic crystal and a TF substrate writes as

$$\gamma_{\rm WC}\left(k_{\rm TF}a\right) = \gamma_{\rm WC}^{\rm ins} - \frac{Q^2}{16\pi\epsilon}\rho_{\rm C}\mathcal{F}(k_{\rm TF}a) \tag{A.2}$$

where $\rho_{\rm C}$ is the crystal density ($\rho_{\rm C} = 1/a$ in 1D) and the function $\mathcal{F}$ is defined as

$$\mathcal{F}(k_{\rm TF}a) = 1 - \mathcal{J}_{\rm cr}\left(k_{\rm TF}a\right) + \mathcal{J}_{\rm TF}\left(k_{\rm TF}a\right), \tag{A.3}$$

with the expressions for $\mathcal{J}_{\rm cr}$ and $\mathcal{J}_{\rm TF}$ as follows:

$$\mathcal{J}_{\rm cr}\left(k_{\rm TF}a\right) = \int_0^{+\infty} {\rm d}\lambda \frac{4\lambda}{\lambda + \sqrt{\lambda^2 + (k_{\rm TF}a)^2}} \frac{{\rm e}^{-2\lambda(h/a)}}{(1+{\rm e}^{-\lambda})^2} \tag{A.4}$$

$$\mathcal{J}_{\rm TF}\left(k_{\rm TF}a\right) = \int_0^{+\infty} {\rm d}\lambda \frac{2\lambda(k_{\rm TF}\alpha)^2}{\sqrt{\lambda^2 + (k_{\rm TF}\alpha)^2}\left[\lambda + \sqrt{\lambda^2 + (k_{\rm TF}\alpha)^2}\right]^2} \frac{{\rm e}^{-2\lambda(h/\alpha)}}{(1+{\rm e}^{-\lambda})^2}\,. \tag{A.5}$$

To find this expression, we first formulate the problem of a single charge close to the boundary and solve for the potential using the Hankel transform, which we integrate to obtain the electrostatic energy of a single charge, and finally we sum the individual contributions to get the energy of the crystal, thus the surface tension.

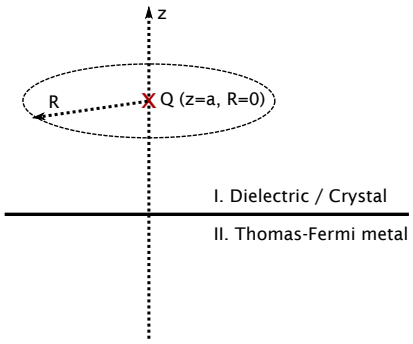

Green's functions. The quantity of interest for the electrostatic interactions is the Green function. The potential for a point charge at $z = \alpha$ in an insulator next to the surface of TF metal (at $z = 0$) follows the combined Poisson and TF equations

$$\Delta\psi_{\rm cr} = -\frac{Q\delta(z-\alpha)\delta(R)}{2\pi\epsilon R} \qquad \text{for} \quad z > 0 \tag{A.6}$$

$$\Delta\psi_{\rm TF} - k_{\rm TF}^2\psi_{\rm TF} = 0 \qquad \text{for} \quad z < 0, \tag{A.7}$$

which read in their Hankel transformed form – $\psi(z,K) = \int \mathrm{d}R\psi(z,R)RJ_0(KR)$ –

$$(\partial_{zz} - K^2)\psi_{\mathrm{cr}} = -\frac{Q\delta(z-\alpha)}{2\pi\epsilon}\,, \tag{A.8}$$

$$(\partial_{zz} - \varkappa_{\mathrm{TF}}^2)\psi_{\mathrm{TF}} = 0 \qquad \text{with} \quad \varkappa_{\mathrm{TF}}^2 = K^2 + k_{\mathrm{TF}}^2\,. \tag{A.9}$$

Boundary conditions at the surface are the continuity of the potential $\psi_{\mathrm{cr}}(z = 0_+) = \psi_{\mathrm{TF}}(z = 0_-)$ and the electric displacement field $\epsilon[\partial_z\psi_{\mathrm{cr}}](z = 0_+) - \epsilon[\partial_z\psi_{\mathrm{TF}}](z = 0_-) = 0$ and the potential decaying to zero at infinity.

Previous equations are solved to give

$$\psi_{\mathrm{cr}}(z > \alpha,K) = \frac{Q\mathrm{e}^{-K\alpha}}{4\pi\epsilon K}\left[\frac{K - \varkappa_{\mathrm{TF}}}{K + \varkappa_{\mathrm{TF}}} + \mathrm{e}^{+2K\alpha}\right]\mathrm{e}^{-Kz} \tag{A.10}$$

$$\psi_{\mathrm{cr}}(z < \alpha,K) = \frac{Q\mathrm{e}^{-K\alpha}}{4\pi\epsilon K}\left[\mathrm{e}^{+Kz} + \frac{K - \varkappa_{\mathrm{TF}}}{K + \varkappa_{\mathrm{TF}}}\mathrm{e}^{-Kz}\right] \tag{A.11}$$

$$\psi_{\mathrm{TF}}(z,K) = \frac{Q\mathrm{e}^{-K\alpha}}{4\pi\epsilon K}\frac{2K}{K + \varkappa_{\mathrm{TF}}}\mathrm{e}^{+\varkappa_{\mathrm{TF}}z}\,. \tag{A.12}$$

In practice, it proves technically easier to consider the ideal metal case a a reference state and calculate the energy difference with respect to (w.r.t.) this case. Accordingly we calculate the excess potential w.r.t. the ideal case (which is obtained readily as a sum of Coulomb potentials from the real and image charges):

$$\Delta\psi_{\mathrm{cr}}(z,K) = \psi_{\mathrm{cr}}(z \geq \alpha,K) - \psi_{\mathrm{cr}}^{(\mathrm{id})}(z \geq \alpha,K) = \tag{A.13}$$

$$= \frac{Q}{4\pi\epsilon K}\left[\mathrm{e}^{+K\alpha} - \frac{\varkappa_{\mathrm{TF}} - K}{\varkappa_{\mathrm{TF}} + K}\mathrm{e}^{-K\alpha}\right]\mathrm{e}^{-Kz} - \frac{Q}{4\pi\epsilon K}\left[\mathrm{e}^{+K\alpha} - \mathrm{e}^{-K\alpha}\right]\mathrm{e}^{-Kz} \tag{A.14}$$

$$= \frac{Q}{4\pi\epsilon K}\frac{2K}{\varkappa_{\mathrm{TF}} + K}\mathrm{e}^{-K\alpha}\mathrm{e}^{-Kz} \tag{A.15}$$

$$\Delta\psi_{\mathrm{cr}}(z,K) = \psi_{\mathrm{cr}}(z \leq \alpha,K) - \psi_{\mathrm{cr}}^{(\mathrm{id})}(z \leq \alpha,K) = \tag{A.16}$$

$$= \frac{Q}{4\pi\epsilon K}\left[\mathrm{e}^{+Kz} - \frac{\varkappa_{\mathrm{TF}} - K}{\varkappa_{\mathrm{TF}} + K}\mathrm{e}^{-Kz}\right]\mathrm{e}^{-K\alpha} - \frac{Q}{4\pi\epsilon K}\left[\mathrm{e}^{+Kz} - \mathrm{e}^{-Kz}\right]\mathrm{e}^{-K\alpha} \tag{A.17}$$

$$= \frac{Q}{4\pi\epsilon K}\frac{2K}{\varkappa_{\mathrm{TF}} + K}\mathrm{e}^{-K\alpha}\mathrm{e}^{-Kz} \tag{A.18}$$

$$\Delta\psi_{\mathrm{TF}}(z,K) = \psi_{\mathrm{TF}}(z,K) - \psi_{\mathrm{TF}}^{(\mathrm{id})}(z,K) = \psi_{\mathrm{TF}}(z,K) = \frac{Q}{4\pi\epsilon K}\frac{2K}{I\varkappa_{\mathrm{TF}} + K}\mathrm{e}^{-K\alpha}\mathrm{e}^{+\varkappa_{\mathrm{TF}}z}\,, \tag{A.19}$$

where we note that we have a single expression for $\Delta\psi_{\mathrm{cr}}$ instead of two different ones for ψ_{cr} and the potential is zero in an ideal metal due to its perfect screening of any charge.

The inverse transform $\psi(z,R) = \int \mathrm{d}K\psi(z,K)KJ_0(KR)$ is not expressible in simple analytic functions. However, the electrostatic energy is an integrated quantity which can be found using the Plancherel theorem for Hankel transform $\int \mathrm{d}Rf(R)g(R)R = \int \mathrm{d}Kf(K)g(K)K$. As we have no boundary terms at infinity and the relation between potential and the induced charge is linear $\rho_{\mathrm{ind}}(z,K) = -\epsilon k_{\mathrm{TF}}^2\psi_{\mathrm{TF}}(z,K)$, we can evaluate the electrostatic energy as the integrated product of charge and potential [1]. The difference of energy, ΔU, between a crystal close to a TF metal and a crystal close to an ideal

metal reads accordingly:

$$\Delta U = \frac{1}{2}\int_{-\infty}^{+\infty} \mathrm{d}z \int_0^{+\infty} 2\pi R \mathrm{d}R \rho(z,R)\Delta\psi(z,R) = \pi \int_{-\infty}^{+\infty} \mathrm{d}z \int_0^{+\infty} \mathrm{d}K \rho(z,K)\Delta\psi(z,K)K \ , \tag{A.20}$$

which we split into the metal (ρ_{ind},ψ_{TF},$z<0$) and the crystal (ρ_{cr},ψ_{cr},$z>0$) integrals to be evaluated separately

$$\Delta U = \pi \int_{-\infty}^{+\infty} \mathrm{d}z \int_0^{+\infty} \mathrm{d}K \rho_{\mathrm{cr}}(z,K)\Delta\psi_{\mathrm{cr}}(z,K)K + \pi \int_{-\infty}^{+\infty} \mathrm{d}z \int_0^{+\infty} \mathrm{d}K \rho_{\mathrm{ind}}(z,K)\psi_{\mathrm{TF}}(z,K)K \ . \tag{A.21}$$

(1) Crystal contribution to the electrostatic energy: The part of the electrostatic energy sum associated with the charge distribution (A.1), *i.e.* the first term in Eq.(A.21), reads

$$\Delta U_{\mathrm{cr}} = \frac{Q}{2}\sum_{n=0}^{\infty}(-1)^n \int_0^{+\infty} \mathrm{d}K \sum_{l=0}^{\infty}(-1)^l \Delta\psi_{\mathrm{cr}}^{(\alpha=la+h)}(na+h,K)K \ . \tag{A.22}$$

which, using eq. (A.13), corresponds to

$$\Delta U_{\mathrm{cr}} = \frac{Q^2}{8\pi\epsilon}\int_0^{+\infty} \mathrm{d}K \frac{2K}{\varkappa_{\mathrm{TF}}+K} \mathrm{e}^{-2Kh} \sum_{n=0}^{\infty}\sum_{l=0}^{\infty}\left(-\mathrm{e}^{-Ka}\right)^{n+l} \ . \tag{A.23}$$

This double geometric series yields

$$\Delta U_{\mathrm{cr}} = \frac{Q^2}{8\pi\epsilon}\int_0^{+\infty} \mathrm{d}K \frac{2K}{\varkappa_{\mathrm{TF}}+K} \frac{\mathrm{e}^{-2Kh}}{\left(1+\mathrm{e}^{-Ka}\right)^2} \ , \tag{A.24}$$

which can be expressed as a prefactor multiplied by a integral over a dimensionless variable $\lambda = Ka$ which evaluates to values between zero and one

$$\Delta U_{\mathrm{cr}} = \frac{Q^2}{16\pi\epsilon a}\int_0^{+\infty} \mathrm{d}\lambda \frac{4\lambda}{\lambda+\sqrt{\lambda^2+(k_{\mathrm{TF}}a)^2}} \frac{\mathrm{e}^{-2\lambda(h/a)}}{(1+\mathrm{e}^{-\lambda})^2} \tag{A.25}$$

$$\equiv \frac{Q^2}{16\pi\epsilon a} \times \mathcal{J}_{\mathrm{cr}}\left(k_{\mathrm{TF}}a\right) \ . \tag{A.26}$$

Note that ΔU_{cr} vanishes in the perfect metal limit $k_{\mathrm{TF}} \to \infty$ and evaluates to $Q^2/(16\pi\epsilon a)$ for the ideal dielectric boundary $k_{\mathrm{TF}} \to 0$, which is a result for a dielectric-dielectric interface previously derived in literature [1].

(2) Metal contribution to the electrostatic energy: The second part of the electrostatic energy sum – second term in Eq.(A.21) – is due to the charge distribution induced in the metal to screen the external charges. For the Thomas-Fermi metal part we use the charge-potential relation $\rho_{\mathrm{ind}} = -\epsilon k_{\mathrm{TF}}^2 \psi_{\mathrm{TF}}$ yielding

$$\Delta U_{\mathrm{TF}} = \pi \int_{-\infty}^{+\infty} \mathrm{d}z \int_0^{+\infty} \mathrm{d}K \rho_{\mathrm{ind}}(z,K)\psi_{\mathrm{TF}}(z,K)K = -\pi\epsilon k_{\mathrm{TF}}^2 \int_{-\infty}^{0} \mathrm{d}z \int_0^{+\infty} \mathrm{d}K \left[\psi_{\mathrm{TF}}(z,K)\right]^2 K \ . \tag{A.27}$$

The potential $\psi_{\rm TF}$ is a geometric sum of the contributions of individual charges to the metal potential

$$\psi_{\rm TF}(z,K) = \sum_{n=0}^{\infty}(-1)^n \psi_{\rm TF}^{[na+h,(-1)^n Q]}(z,K) = \frac{Q\mathrm{e}^{-Kh}}{4\pi\epsilon K}\frac{2K}{K+\varkappa_{\rm TF}}\frac{\mathrm{e}^{+\varkappa_{\rm TF}z}}{1+\mathrm{e}^{-Ka}}\ , \tag{A.28}$$

the convergence of which can be proven by considering physically relevant finite crystals. This yields the electrostatic energy of the charge induced in the metal as

$$\Delta U_{\rm TF} = -\pi\epsilon k_{\rm TF}^2\left[\frac{Q}{2\pi\epsilon}\right]^2\int_{-\infty}^{0}\mathrm{d}z\int_0^{+\infty}\mathrm{d}K\left[\frac{1}{K+\varkappa_{\rm TF}}\frac{\mathrm{e}^{-Kh}}{1+\mathrm{e}^{-Ka}}\right]^2\mathrm{e}^{+\varkappa_{\rm TF}z}K \tag{A.29}$$

$$= -\frac{Q^2k_{\rm TF}^2}{4\pi\epsilon}\int_0^{+\infty}\mathrm{d}K\left[\frac{1}{K+\varkappa_{\rm TF}}\frac{\mathrm{e}^{-Kh}}{1+\mathrm{e}^{-Ka}}\right]^2\frac{K}{\varkappa_{\rm TF}} \tag{A.30}$$

$$= -\frac{Q^2k_{\rm TF}^2}{8\pi\epsilon}\int_0^{+\infty}\mathrm{d}K\frac{K\mathrm{e}^{-2Kh}}{\sqrt{K^2+k_{\rm TF}^2}\left[K+\sqrt{K^2+k_{\rm TF}^2}\right]^2\left[1+\mathrm{e}^{-Ka}\right]^2}\ , \tag{A.31}$$

which goes to zero as $k_{\rm TF}^{-1}=\ell_{\rm TF}$ if $\ell_{\rm TF}\to 0$ (ideal metal limit, $k_{\rm TF}\to\infty$) and also vanishes as $k_{\rm TF}=\ell_{\rm TF}^{-1}$ for vacuum or ideal dielectric boundary ($k_{\rm TF}\to 0$). We convert this integral to a dimensionless form

$$\Delta U_{\rm TF} = -\frac{Q^2}{16\pi\epsilon a}\int_0^{+\infty}\mathrm{d}\lambda\frac{2\lambda(k_{\rm TF}a)^2}{\sqrt{\lambda^2+(k_{\rm TF}a)^2}\left[\lambda+\sqrt{\lambda^2+(k_{\rm TF}a)^2}\right]^2}\frac{\mathrm{e}^{-2\lambda(h/a)}}{(1+\mathrm{e}^{-\lambda})^2} \tag{A.32}$$

$$\equiv -\frac{Q^2}{16\pi\epsilon a}\times\mathcal{J}_{\rm TF}\left(k_{\rm TF}a\right)\ , \tag{A.33}$$

Summary: Surface energy
We now gather the various contributions for the electrostatic energy, $\Delta U_{\rm TF}$ and $\Delta U_{\rm cr}$. These correspond to surface energies, w.r.t. the ideal metal case. Thus, adding the surface tension for the perfect metal substrate, recalled above, we thus obtain $\gamma_{\rm WC}\left(k_{\rm TF}a\right) = \frac{Q^2}{16\pi\epsilon a}\left[1+\mathcal{J}_{\rm cr}\left(k_{\rm TF}a\right)-\mathcal{J}_{\rm TF}\left(k_{\rm TF}a\right)\right]$, where the $\mathcal{J}$-functions are defined in the expression above. Reorganizing the terms, this concludes the proof of Eq. (A.2).

A.2 Physical interpretation and an approximated scheme

An interesting remark is that the electrostatic contribution to the interfacial energy $\gamma_{\rm WC}$, which is exactly obtained in Eq. (A.2) for a 1D crystal, can be qualitatively interpreted in terms of the interaction of individual particles with their images. More specifically, we show below that *for any* $k_{\rm TF}$ *parameter*, the excess surface tension w.r.t. its insulating limit can be roughly approximated by

$$\gamma_{\rm WC}(k_{\rm TF}) - \gamma_{\rm WC}^{\rm ins} \approx \rho_{\rm C}\times a\times U^{(1)}(a) \tag{A.34}$$

where $U^{(1)}$ is the one-body interaction energy of a single ion with its image charge, at a distance a close to the TF surface; $\rho_{\rm C}$ is the crystal density, and the expression for $\gamma_{\rm WC}(k_{\rm TF})$ is given in Eq. (A.2).

This conclusion, which is interpreted physically below, stems from a detailed analysis of the various analytical contributions to the surface tension and energy interaction.

To do so, let us first calculate the one-body interaction of a single, isolated particle close to a flat surface, at a distance z from the wall. In the case of an ideal metal, the potential of a charge can be found from the image charge method and the electrostatic energy $U^{(1)}_{\rm ideal} = -Q^2/[16\pi\epsilon z]$ is half of what an equivalent pair of real charges would yield [1]. In the general case, the total electrostatic energy is half the scalar product of the charge density and the electrostatic potential, split between the induced charge ($\rho_{\rm ind}$, $\psi_{\rm TF} = \psi_{\rm TF}$, $z < 0$ support) and the external charge ($\rho_{\rm cr}$, $\psi_{\rm cr} = \psi_{\rm cr}$, $z > 0$ support) parts. Therefore the derivation for $U^{(1)}(z)$ follows the same steps as for the total electrostatic energy above

$$U^{(1)}(z) = \pi \int_{-\infty}^{+\infty} {\rm d}z' \int_0^{+\infty} {\rm d}K\, K \left[\rho_{\rm ind}(z|z',K) + \rho_{\rm cr}(z|z',K)\right] \psi(z|z',K) \tag{A.35}$$

where we used the Plancherel theorem for the Hankel transform to equate the direct and reciprocal space integrations. The resulting expressions for $U^{(1)}(z)$ are obtained in terms of an integral $\mathcal{I}_{\rm cr}$ over the dimensionless variable $\lambda = Kz$

$$U^{(1)}(z) = -\frac{Q^2}{16\pi\epsilon z}(1 - \mathcal{I}_{\rm cr} + \mathcal{I}_{\rm TF}) \text{ , where} \tag{A.36}$$

$$\mathcal{I}_{\rm cr} = \int_0^{+\infty} {\rm d}\lambda \frac{4\lambda {\rm e}^{-2\lambda}}{\sqrt{\lambda^2 + (k_{\rm TF}z)^2} + \lambda} \tag{A.37}$$

$$\mathcal{I}_{\rm TF} = \int_0^{+\infty} {\rm d}\lambda \frac{2(k_{\rm TF}z)^2 \lambda {\rm e}^{-2\lambda}}{\left(\lambda + \sqrt{\lambda^2 + (k_{\rm TF}z)^2}\right)^2 \sqrt{\lambda^2 + (k_{\rm TF}z)^2}}. \tag{A.38}$$

$\mathcal{I}_{\rm cr}$ goes to unity for the insulating limit ($k_{\rm TF} = 0$) and vanishes for the ideal metal ($k_{\rm TF} \to \infty$); $\mathcal{I}_{\rm TF}$ vanishes in both limits.

At this stage, a key remark then is that taking for $z = a$, leads to

$$U^{(1)}(a) \approx -\frac{Q^2}{16\pi\epsilon a}\mathcal{F}(k_{\rm TF}a) \tag{A.39}$$

where the expression for $\mathcal{F}(k_{\rm TF}a)$ is given in Eq. (A.2). This can be actually verified by a direct numerical comparison between the two expressions. But beyond, their analytical definitions are extremely close, as pointed out by a direct inspection of their expression: compare $\mathcal{I}_{\rm cr}$ and $\mathcal{J}_{\rm cr}$ in Eq. (A.4) versus Eq. (A.37), as well as $\mathcal{I}_{\rm TF}$ and $\mathcal{J}_{\rm TF}$ in Eq. (A.5) versus Eq. (A.38). Furthermore they interpolate smoothly between the perfect metal and the insulating substrate, as a function of the characteristic TF parameter $k_{\rm TF}$, with obviously a cross over occuring at $k_{\rm TF}a \sim 1$; they also have the same limiting values in both limiting regimes of insulating walls and perfect metal.

The underlying physical reason is transparent: this agreement stems from the fact that the surface energy – in excess to the insulating case as a reference, in which there is no image charge– merely originates from the interaction of ions in the vicinity of the substrate with their image charges. Contributing charges are typically within a volume of extension of a molecular length a, with a number $N_c \sim \rho_{\rm C} \times a$ (per unit surface, with $\rho_{\rm C}$ the density of the crystal). The molecular extension a is determined by the electroneutrality condition, leading to a cutoff of the interaction beyond a. Accordingly it suggests that the excess surface tension can be approximated by summing up the direct one-body energy terms *within this volume of size a* (and dividing by the lateral area a^2):

$$\gamma_{\rm WC}(k_{\rm TF}) - \gamma^{\rm ins}_{\rm WC} \approx \rho_{\rm C} \times a \times U^{(1)}(a) \tag{A.40}$$

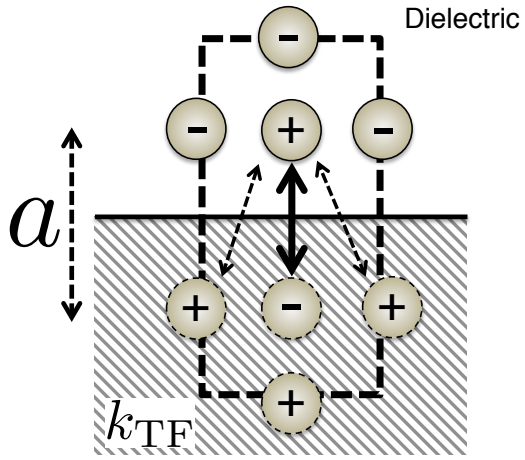

Figure A.1: Sketch of charges close to a Thomas-Fermi metal interacting with their image charges. A volume of extension a, defined in terms of electro-neutrality, interact with its image charges. Charges beyond are screened out by electroneutrality.

This approximated expression captures the main tendencies of the surface tension γ_{WC} as a function of the TF screening parameter k_{TF}.

Obviously Eq.(A.40) is not an exact result, but this simple estimate is fully validated by the exact calculation of the interfacial energy. It further captures the main physical ingredients and reproduces properly – at a qualitative level – the dependency of the surface tension of the crystal with a TF wall.

A.3 Surface energy of a liquid with a TF wall

By giving a simple interpretation of the surface tension for a condensed phase at a metal surface, the previous argument can be extended to other interfaces, and in particular a liquid-wall interface. Indeed in this case, the ion configurations are mostly disordered, although with a strong local ordering originating in the electrostatic correlations. It is *a priori* not possible to proceed along the analytical steps above to calculate the expression for the electrostatic energy of a ionic liquid in the presence of a TF wall. However following the previous approximation scheme, one may assume physically that the contribution of the interfacial energy – in excess to the insulating case – of a ionic liquid at a metallic wall originates mostly from the direct interaction of charges with their images. This provides an *approximated scheme* to obtain an estimate of the liquid-TF wall surface energy, γ_{wl}. Following the discussion above, one can thus writes as

$$\gamma_{\mathrm{wl}} - \gamma_{\mathrm{wl}}^{\mathrm{ins}} \approx \rho_{\mathrm{L}} \times a \times U^{(1)}(a) \tag{A.41}$$

where ρ_{L} is now the density of the ionic *liquid* (since $\rho_{\mathrm{L}} < \rho_{\mathrm{C}}$ for ionic systems, there are less ions interacting with their image at the surface); a is again a molecular length scale, in the range of the molecular size of the ions, and thus of the same order of magnitude as the crystal lattice spacing. Since $a \times U^{(1)} \approx -\frac{Q^2}{16\pi\epsilon}\mathcal{F}(k_{\mathrm{TF}}a)$, at this level of approximation, we can write this equation approximatively in terms of the function $\mathcal{F}$. We therefore obtain

$$\gamma_{\mathrm{wl}} - \gamma_{\mathrm{wl}}^{\mathrm{ins}} \approx -\rho_{\mathrm{L}} \times \frac{Q^2}{16\pi\epsilon}\mathcal{F}(k_{\mathrm{TF}}a) \tag{A.42}$$

Note that at this level of approximation, we took the same value of a for both the liquid and crystal (chosen here as the crystal lattice spacing in the crystal), since this choice does not make a strong difference in the functional dependence of $\mathcal{F}(k_{\rm TF}a)$.

Again we emphasize that this expression is only approximate, but this approximation is expected to capture the main contributions for the surface energy, as validated by the exact benchmarking calculations above for the crystal-metal interface.

A.4 Relative wetting of the crystal versus the liquid at a TF wall

We can now gather the various contribution to calculate $\Delta\gamma = \gamma_{\rm wl} - \gamma_{\rm WC}$ the interfacial free energy difference between the liquid-metal and the crystal-metal interfaces. Using Eqs.(A.2) and (A.42), one accordingly obtains

$$\Delta\gamma = \gamma_{\rm wl} - \gamma_{\rm WC} \approx \Delta\gamma^{\rm ins} + (\rho_{\rm C} - \rho_{\rm L})\frac{Q^2}{16\pi\epsilon} \times \mathcal{F}(k_{\rm TF}a) \tag{A.43}$$

where $\Delta\gamma^{\rm ins} = \gamma_{\rm wl}^{\rm ins} - \gamma_{\rm WC}^{\rm ins}$. The last term is positive because $\rho_{\rm L} < \rho_{\rm C}$. This is the equation (5) reported in the main text.

Note that for practical purposes, one may use a simple fitting form for the function $\mathcal{F}(k_{\rm TF}a)$ as $\mathcal{F}(k_{\rm TF}a) \simeq k_{\rm TF}a/(\nu + k_{\rm TF}a)$. We find that $\nu \simeq 1.7$ provides a good quantitative fit to the exact expression for $\mathcal{F}(k_{\rm TF}a)$. This is inspired in particular by a similar expression for $U^{(1)}$ derived by Kornyshev and Vorotyntsev [2] (assuming in the present case a uniform dielectric constant). This simple rational approximation has the merit of simplicity.

A.5 Molecular dynamics of the crystallisation of a molten salt in confinement

In order to investigate the effect of confinement on the crystallization of ionic systems, we performed molecular simulations for a simple salt made up of positive and negative (unit) charges confined inside an atomistic slit pore. In the simulations described below, the confining boundaries are insulating.

In what follows, all lengths and distances are expressed with respect to the lattice spacing a for the crystalline phase while energies are expressed with respect to the energy for an ionic pair separated by the distance a, $U_0 = q^2/(4\pi\epsilon_0 a)$. As a result, temperatures are expressed in reduced units with respect to the reference temperature $T_0 = U_0/k_B$ (the latter choice allows defining the dimensionless temperature from the Bjerrum length l_B, i.e. $T = a/l_B$). The ionic system is described using the well-established Tosi-Fumi model [8] with the physical parameters for NaCl [9]. Within this model, the pair interaction potential between two atoms i and j separated by a distance r is given as the sum of a Born-Huggins-Mayer repulsive contribution, two attractive dispersive contributions, and the Coulomb interaction contribution:

$$U_{ij}(r) = A_{ij}\exp[B_{ij}(\sigma_{ij} - r)] - \frac{C_{ij}^6}{r^6} - \frac{D_{ij}^8}{r^8} + \frac{q_i q_j}{4\pi\epsilon_0 r} \tag{A.44}$$

In order to keep these molecular simulations as simple as possible while retaining the physics of the Coulomb interaction, we use the damped shifted Coulomb force technique.

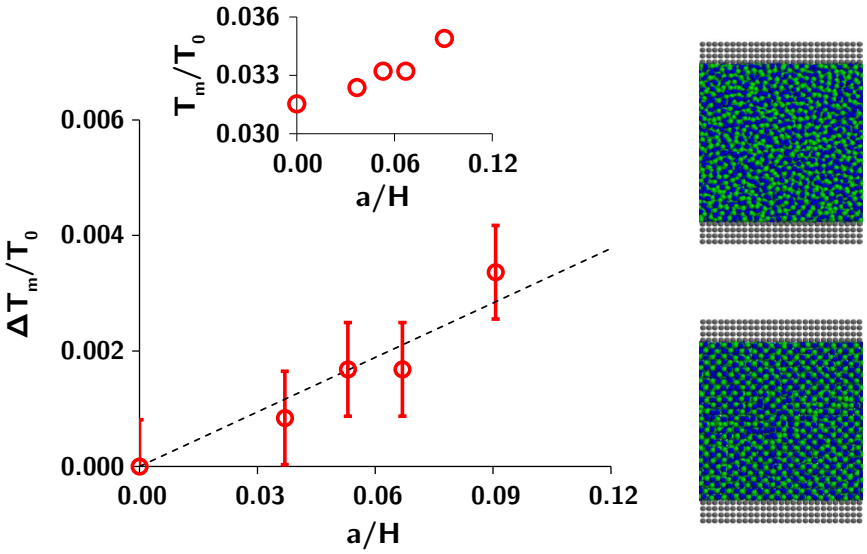

Figure A.2: Shift in the melting temperature $\Delta T_{\mathrm{m}}/T_0$ with respect to the bulk melting point as a function of the reciprocal of pore size a/H for a nanoconfined salt. The symbols are the results from molecular simulation (direct coexistence method) while the dashed line is a linear fit corresponding to the Gibbs-Thomson equation. The insert shows the melting temperature T_{m}/T_0 as a function of a/H. The snapshots on the right show a typical molecular configuration for the confined liquid (top) and crystal (bottom). The blue and green spheres are the cations and anions while the grey atoms are the wall atoms.

This method consists of truncating and shifting the pair force and pair potential so that both go to zero at the cut-off value, $r_{\mathrm{C}}/a = 6.7$:

$$U_{C,ij}(r) = \frac{q_i q_j}{4\pi\epsilon_0 r}\left[\frac{1}{r} + \frac{r}{r_C^2} - \frac{2}{r_C}\right] \tag{A.45}$$

$$\mathbf{F}_{C,ij}(r) = \frac{q_i q_j}{4\pi\epsilon_0 r}\left[\frac{1}{r^2} - \frac{1}{r_C^2}\right]\frac{\mathbf{r}}{r} \tag{A.46}$$

The slit pores considered in this work, which have a reduced size H/a, are made up of a cubic array of neutral atoms separated by a distance a. Each ion in the confined system interacts through the same pair potential as that described in Eq. A.44 (except for the Coulomb contribution since the wall atoms are neutral). For such a wall/ion contribution, we used the same physical parameters as those for the cation/cation interactions. Fig. A.2 shows typical molecular configurations for the confined liquid and crystal in a pore of a width $H/a = 27$.

Crystallization of the confined salt as well as of the bulk salt was assessed using the Direct Coexistence Method [3, 7]. With this method, we first prepared a system in which the crystal and liquid phases coexist (typically, if z is the direction perpendicular to the pore surface, the system is prepared with the crystal occupying the space $x \leq 0$ while the liquid occupies the rest of the space $x > 0$). Such a coexisting system was then equilibrated at different temperatures in the canonical ensemble using Molecular Dynamics (temperature was imposed using a Nose-Hoover thermostat). From this initial condition, and depending on the temperature, the crystaline phase grows or shrinks. The melting temperature T_{m}

is determined as the cross-over between these two regimes: the crystal melts for $T > T_{\mathrm{m}}$ while the liquid crystallizes for $T < T_{\mathrm{m}}$.

Fig. A.2 shows the shift in the melting temperature $\Delta T_{\mathrm{m}}/T_0$ with respect to the bulk melting point as a function of the reciprocal of pore size a/H for the nanoconfined salt. The crystal/liquid transition temperature is shifted to higher temperature for all pore sizes H/a (ranging from 0.03 to 0.10), suggesting that the crystal wets better the surface than the liquid. The shift in melting temperature increases linearly with increasing the reciprocal pore size a/H, in full agreement with the celebrated Gibbs-Thomson equation:

$$\Delta T_{\mathrm{m}} = T_{\mathrm{m}} - T_{\mathrm{m}}^0 = \frac{2T_{\mathrm{m}}^0 \Delta\gamma}{\rho_{\mathrm{L}} \Delta h_{\mathrm{fus}} H} \tag{A.47}$$

where T_{m}^0 is the bulk melting temperature, $\Delta\gamma = \gamma_{\mathrm{LW}} - \gamma_{\mathrm{CW}}$ the difference between the liquid/wall and crystal/wall surface tension, ρ_{L} the bulk density of the liquid phase (here assumed to be equal to that of the crystal for simplification), and Δh_{fus} is the bulk latent heat of fusion.

Since Δh_{fus} and ρ_{L} are known for the Tosi-Fumi model considered in this work, $\Delta\gamma$ can be estimated by fitting the data in Fig. A.2 against Eq. (A.47). We found $\Delta\gamma = 0.2$ which is positive since the crystal wets the wall surface rather than the liquid (considering the reduced units used in throughout this part, surface tensions are normalized to $\gamma_0 = \frac{q^2}{4\pi\epsilon_0 a^3}$).

In order to confirm these numbers, we estimated independently γ_{LW} and γ_{CW} from the normal (P_{N}) and tangential (P_{T}) pressures:

$$\gamma = \frac{1}{2}\int (P_{\mathrm{N}}(z) - P_{\mathrm{T}}(z))\mathrm{d}z \sim \frac{L_z}{2}\big\langle P_{\mathrm{N}} - P_{\mathrm{T}}\big\rangle \tag{A.48}$$

where the second equality simply corresponds to the mean value theorem (L_z is the system dimension in the direction z which corresponds to the direction normal to the pore surfaces). The factor 1/2 in the above equations is required as the system exhibits two wall/liquid or wall/crystal interfaces. $P_{\mathrm{N}} = P_{zz}$ and $P_{\mathrm{T}} = 1/2(P_{xx} + P_{yy})$ can be estimated from the pressure tensor using the virial formalism (for N particles i and j subjected to pair additive interactions):

$$P_{\alpha\beta} = \rho k_B T \delta_{\alpha\beta} + \frac{1}{V}\sum_{j>i}^{N} F_{ij} r_{ji} \tag{A.49}$$

where $\alpha, \beta = x, y$ or z. $\delta_{\alpha\beta}$ is the Kronecker symbol, V the system's volume, F_{ij} the force exerted by j on i and $r_{ji} = r_i - r_j$. Following the work of Nijmeijer et al. [5, 6], wall/fluid interactions were omitted when computing the tangential pressure owing to the atomistic/crystalline nature of the pore wall. We found that the liquid/wall surface tension, $\gamma_{\mathrm{LW}} = 0.15$, is indeed larger thant the crystal/wall surface tension, $\gamma_{\mathrm{CW}} = 0.07$, leading to a surface tension difference $\Delta\gamma$ of the same order of magnitude as that inferred from the Gibbs-Thomson equation applied to the results from the direct coexistence methodology.

Bibliography

1. Jackson, J. D. *Classical Electrodynamics* 641. ISBN: 9780471431312 (John Wiley & Sons, 1998).

2. Kornyshev, A. A. & Vorotyntsev, M. A. Analytic expression for the potential energy of a test charge bounded by solid state plasma. *Journal of Physics C: Solid State Physics* **11** (1978).
3. Ladd, A. J. C. & Woodcock, L. V. Triple-point coexistence properties of the lennard-jones system. *Chemical Physics Letters* **51,** 155–159 (1977).
4. Mahan, G. D. in (Springer Science & Business Media, 2013).
5. Nijmeijer, M. J., Bruin, C., Bakker, A. F. & Van Leeuwen, J. M. Wetting and drying of an inert wall by a fluid in a molecular-dynamics simulation. *Physical Review A* **42,** 6052–6059 (1990).
6. Nijmeijer, M. J., Van & Leeuwen, J. M. Microscopic expressions for the surface and line tension. *Journal of Physics A: General Physics* **23,** 4211–4235 (1990).
7. Noya, E. G., Vega, C. & De Miguel, E. Determination of the melting point of hard spheres from direct coexistence simulation methods. *Journal of Chemical Physics* **128** (2008).
8. Tosi, M. & Fumi, F. Ionic sizes and born repulsive parameters in the NaCl-type alkali halidesâII. *Journal of Physics and Chemistry of Solids* **25,** 45–52 (1964).
9. Valeriani, C., Sanz, E. & Frenkel, D. Rate of homogeneous crystal nucleation in molten NaCl. *Journal of Chemical Physics* **122** (2005).

Résumé

Dans ce Manuscript, nous mesurons la réponse mécanique à l'échelle nanométrique de divers systèmes issus de la matière molle en utilisant un Microscope à Force Atomique basé sur un diapason à quartz. Utilisé comme un nano-rhéomètre, cet instrument permet une mesure quantitative des propriétés viscoélastiques des matériaux et des processus frictionnels et dissipatifs aux nanoéchelles.
Nous montrons d'abord que les liquides ioniques confinés aux nanoéchelles peuvent subir un changement dramatique de leurs propriétés mécaniques, suggérant une solidification capillaire. Cette transition est favorisée par la nature métallique des interfaces confinantes, montrant la présence d'effets électrostatiques subtils dans ces électrolytes denses.
Nous étudions ensuite les mécanismes de plasticité à l'échelle atomique en mesurant la réponse viscoélastique de jonctions d'or de quelques atomes de diamètre. Nous mettons en évidence une transition sous cisaillement entre un régime élastique, puis plastique, jusqu'à la liquéfaction complète de la jonction. Nous caractérisons ainsi de manière fine les mécanismes de plasticité dans ces systèmes moléculaires.
Finalement, nous montrons les effets profonds que les interactions à l'échelle nanométrique peuvent avoir sur le comportement macroscopique de la matière molle. Nous mesurons le profil frictionnel entre paires de particules de suspensions de PVC et de Maïzena. Nos mesures mettent en lumière le rôle dominant des interactions locales entre particules dans la rhéologie non-newtonienne des suspensions.

Mots Clés

Microscopie à Force Atomique – Tribologie – Rhéologie – Matière Molle – Nanoscience

Abstract

In this Manuscript, we use a tuning fork based Atomic Force Microscope to measure the mechanical response of various soft matter systems at the nanoscale. This instrument is used as a nano-rheometer, allowing quantitative measurements of viscoelastic material properties, and unprecedented characterization of friction and dissipation at the nanoscale.
First, we show that ionic liquids can undergo a dramatic change in their mechanical properties when confined at the nanoscale, pointing to a capillary freezing transition. This transition is favored by the metallic nature of the confining substrates, suggesting the occurrence of subtle electrostatic effects in those dense electrolytes.
Second, we probe plasticity at the individual atomic level, by measuring the viscoelastic rheological response of gold junctions of few atoms diameter. For increasing shear, we uncover a transition from a purely elastic regime to a plastic flow regime, up to the complete shear-induced melting of the junction. Our measurements give unprecedented insights on the plastic mechanisms at play in those molecular systems.
Finally, we show that nanoscale interactions can have profound effects on the macroscopic behavior of soft materials. Focusing on the non-newtonian flow behavior of concentrated suspensions of particles, we measure the nanoscale frictional force profile between pairs of particles of PVC and Cornstarch suspensions. Our measurements highlight the dominant role of local interparticle interactions on the macroscale rheology of suspensions.

Keywords

Atomic Force Microscopy – Tribology – Rheology – Soft Matter – Nanoscience